**République Algérienne Démocratique et Populaire**
**Ministère de l'Enseignement Supérieur et de la Recherche Scientifique**
**Ecole Nationale Polytechnique**
**Département de Métallurgie**

Doctoral Thesis in Materials

**Major**

Materials sciences

**Presented by** :

AZZOUG Rabah

**Entitled:**

# Elaboration and characterization of composite coatings in NiFeCrBSi-WC, applied to drilling tools

Defended in front of the jury composed of :

| | | |
|---|---|---|
| Mohamed Chitroub | Professor at ENP | President |
| Fatah Hellal | Professor at ENP | Supervisor |
| Yamina Mebdoua Lahmar | Director of Research at CDTA | Co-Supervisor |
| Nadir Mesrati | Professor at ENP | Examinor |
| Naïma Zaouarar | Professor at USTHB | Examinor |
| Kasser Abdelmadjid | Lecturer at ENP | Examinor |
| Achraf Boudiaf | Lecturer at EMP | Examinor |

**ENP 2022**

**People's Democratic Republic of Algeria**
**Ministry of Higher Education and Scientific Research**
**National Polytechnic School**
**Department of Metallurgy**

Doctoral Thesis in Materials

**Major**

Materials sciences

**Presented by** :

AZZOUG Rabah

**Entitled:**

# Elaboration and characterization of composite coatings in NiFeCrBSi-WC, applied to drilling tools

Defended in front of the jury composed of :

| | | |
|---|---|---|
| Mohamed Chitroub | Professor at ENP | President |
| Fatah Hellal | Professor at ENP | Supervisor |
| Yamina Mebdoua Lahmar | Director of Research at CDTA | Co-Supervisor |
| Nadir Mesrati | Professor at ENP | Examinor |
| Naïma Zaouarar | Professor at USTHB | Examinor |
| Kasser Abdelmadjid | Lecturer at ENP | Examinor |
| Achraf Boudiaf | Lecturer at EMP | Examinor |

**ENP 2022**

**République Algérienne Démocratique et Populaire**
**Ministère de l'Enseignement Supérieur et de la Recherche Scientifique**
**Ecole Nationale Polytechnique**
**Département de Métallurgie**

Thèse de Doctorat en Matériaux

**Option**

Sciences des matériaux

**Presentée par** :

AZZOUG Rabah

**Intitulée:**

# Elaboration et caractérisation de revêtements composites en NiFeCrBSi-WC, appliqués aux outils de forage

Soutenue devant le jury composé de :

| | | |
|---|---|---|
| Mohamed Chitroub | Professeur à l'ENP | Président |
| Fatah Hellal | Professeur à l'ENP | Rapporteur |
| Yamina Mebdoua Lahmar | Directrice de Recherche au CDTA | Co-Rapporteur |
| Nadir Mesrati | Professeur à l'ENP | Examinateur |
| Naïma Zaouarar | Professeur à l'USTHB | Examinateur |
| Kasser Abdelmadjid | Maitre de conférence à l'ENP | Examinateur |
| Achraf Boudiaf | Maitre de conférence à l'EMP | Examinateur |

**ENP 2022**

# Acknowledgement

Foremost, I would express my deep and special gratitude to my parents who have always supported and encouraged me throughout my schooling days.

I would like to express my sincere thanks to my supervisors Pr. Fatah HELLAL, Yamina MEBDOUA and Francesco Marra, who have given me a lot of valuable advices and feedbacks. I would also thank them for their encouragement, availability, and help. Furthermore, I would appreciate their eagerness to do this thesis work in the best circumstances.

I would also like to substantially acknowledge Pr.Mohamed Chitroub for having honored me by accepting to chair the jury, Pr.Nadir Mesrati, Pr.Naïma Zaouarar, Dr.Kasser Abdelmadjid and Dr.Achraf Boudiaf for agreeing to judge my humble thesis;

I also extend my gratitude to all the professors of the National Polytechnic School for the support they have shown for this thesis, either through their dedication or cooperation.

**ملخص**

**يستخدم الفولاذ منخفض السبائك عادة في صناعة أدوات الحفر وهذا لضمان المتانة الجيدة لهذه الأجزاء. وبما أن أدوات الحفر معرضة لظروف العمل القاسية ، فإنها غالباً ما تكون مغطاة بطلاءات لتقليل التآكل والصدأ. تم تنفيذ هذا العمل بهدف دراسة سلوك نوعين من سيرميت النيكل(NiFeCrBSi-WC) المستخدمة كطلاءات لتحسين خصائص سطح الفولاذ العادي X18 وهي الخصائص الكهروكيميائية ومكافحة التآكل.**

**وقد تم اختيار عملية الترسيب بالرش الحراري للهب مع الأخذ بعين الاعتبار جميع المعاملات التي تؤثر على تشكل ومجهرية الترسيب من درجة حرارة التسخين، خشونة السطح، معدل تدفق الغازات المستخدمة، و المسافة بين الشعلة والركيزة وسرعة حركة الشعلة. كان سمك التراسيب حوالي 3 ملم. وقد تمت دراسة الطلاء بواسطة المجهر الضوئي والإلكتروني، من خلال قياسات صلابة، الصلادة الدقيقة والنانونية وحيود الأشعة السينية والاختبارات الكهروكيميائية.**

**تميزت البنية المجهرية لأول طلاء NiFeCrBSi-WC بوجود طور شجيري من النيكل محاط بسهل الانصهار وتشتت كربيدات الكروم. تحتوي هذه البنية المجهرية أيضًا على مستوى مسامية يبلغ حوالي 2٪ ، وأظهرت النتائج أن البنية المجهرية للطلاء الثاني متشجرة وتحتوي على توزيع كربيدات الكروم جنبًا إلى جنب مع كربيدات التنجستن. وقد لوحظ نوعان متميزان من تشعبات Ni-. أحدهما غني بالنيكل أكثر من الآخر. تعتمد صلابة الطلاء على طبيعة المراحل الموجودة والمسامية. كشفت قياسات الصلادة الدقيقة أن صلابة هذه الطلاءات يمكن أن تصل إلى قيمة قصوى تبلغ حوالي HV 3000. علاوة على ذلك ، أثبتت منحنيات EIS أن الزيادة في تركيز الأيونات تزيد من نقل الشحنة في واجهة الطلاء / الإلكتروليت وتسرع من التآكل .في المحاليل الكبريتية ، تشكل الطلاءات الأولى طبقة رقيقة ومضغوطة من الغشاء الخامل تجعل نقل الشحنة ثابتًا بشكل دائم عند تركيزات عالية من الأيونات (35 جم / لتر)**

**الكلمات المفتاحية: فولاذ، نيكل، سيرميت، بنية مجهرية، صلادة، صدأ.**

**Résumé**

L'acier faiblement allié est couramment utilisé dans la fabrication des têtes de forage et ceci pour garantir une bonne ténacité à ces pièces. Vu que les têtes de forage sont exposées à des conditions de travail draconiennes, elles sont souvent revêtues afin de réduire leur dégradation par usure et par corrosion. Le présent travail a été effectué dans l'objectif d'examiner le comportement de deux types de cermets à base de nickel ( NiFeCrBSi-WC), utilisés comme revêtement, pour améliorer les propriétés en surface d'un acier ordinaire X18, que sont les propriétés mécaniques et électrochimiques.

Le choix du procédé de revêtement a été porté sur le procédé de projection thermique à flamme. Nous avons pris en considération tous les paramètres influant sur la morphologie et la microstructure des dépôts, tels que la température de préchauffage, la rugosité, le débit des gaz utilisés, la distance entre la torche et le substrat et la vitesse de déplacement de la torche. Les épaisseurs des revêtements obtenues ont été de l'ordre de 3mm. La détermination préalable de la composition chimique des matériaux utilisés a été faite par spectrométrie de fluorescence X. La caractérisation des dépôts a été faite par le biais de la microscopie électronique, de mesures de dureté, de microdureté et de nano-indentation, ainsi que par la diffraction des rayons X. Des essais électrochimiques (polarisation dynamique et spectrométrie d'impédance EIS) ont été réalisés dans des solutions de NaCl et de $Na_2SO_4$.

La microstructure du premier revêtement NiFeCrBSi-WC a été marquée par la présence d'une phase dendritique de nickel entourée de phase eutectique et de carbures de chrome dispersés. Cette microstructure contient un taux de porosité d'environ 2%. Les résultats montrent que la microstructure du deuxième revêtement NiFeCrBSi-WC est dendritique et contient une distribution de carbures de chrome à côté des carbures de tungstène. Deux types distincts de dendrites Ni-γ ont été observés. L'un est plus enrichi en nickel que l'autre. Les analyses microscopiques ont démontrées que les carbures de tungstène ont été object d'une décarburation. La dureté des revêtements dépend de la nature des phases présentes et de la présence de porosités dans les zones indentées. Les mesures de microdureté ont révélé que la dureté de ces revêtements pouvait atteindre une valeur maximale de l'ordre de 3000HV. De plus, les courbes EIS ont prouvé que l'augmentation de la concentration en ions augmente le transfert de charge à l'interface revêtement/électrolyte et accélère la corrosion. Dans les solutions sulfuriques, les premiers revêtements forment une couche mince et compacte. Ce film passif rend le transfert de charge constant en permanence à des concentrations ioniques élevées (35g/l)

**Mots clés : acier, nickel, cermet, microstructure, dureté, corrosion.**

**Abstract**

Low alloy steel is commonly used in the manufacture of drilling bits and this to ensure good toughness to these parts. Since drilling bits are exposed to harsh working conditions, they are often coated to reduce wear and corrosion. This work was carried out with the aim of examining the behavior of two types of nickel-based cermets (ie NiFeCrBSi-WC), using them as coatings, to further improve the surface properties of an ordinary X18 steel namely the electrochemical and anti-wear properties.

The choice of the coating process was focused on the flame thermal projection process taking into consideration all parameters affecting the morphology and microstructure of deposits such as preheating temperature, roughness, gas flow rate, distance between the torch and the substrate and the speed of movement of the torch. The thicknesse of the coatings was of the order of 3 mm. The preliminary determination of the chemical composition of the used materials was made by X-ray fluorescence spectrometry. The characterization of the deposits was performed by means of electron microscopy, hardness, microhardness and nano-indentation measurements, as well as by X-ray diffraction. Electrochemical tests (dynamic polarization and EIS impedance spectrometry) were carried out in NaCl and $Na_2SO_4$ solutions.

The microstructure of the first NiFeCrBSi-WC coating was marked by the presence of a nickel dendritic phase surrounded by the eutectic and a dispersion of chromium carbides. This microstructure additionally contains a porosity level of about 2%. The results show that the microstructure of the second coating NiFeCrBSi-WC is dendritic and contains a distribution of chromium carbides alongside with the tungsten carbides. Two distinct types of Ni-γ dendrites have been observed. One is more enriched in nickel than the other. The microscopic analyzes have shown that tungsten carbides were subject to decarburization The hardness of the coatings depends on the nature of the phases present and the porosity in the indented areas. Microhardness measurements have revealed that the hardness of these coatings can reach a maximum value of around 3000 HV. Moreover, the EIS curves proved that the increase in ion concentration augments the charge transfer at the coating/electrolyte interface and accelerates corrosion. In the sulfuric solutions, the first coatings form a thin and compact passive film layer that makes the charge transfer permanently constant at high ion concentrations (35 g/l).

**Keywords: steel, nickel, cermet, microstructure, hardness, corrosion.**

## List of symbols

$h_m$ : The depth from the original specimen surface at maximum load

$h_{rc}$ : The calculated depth of the residual impression for an equivalent punch

$h_e$ : The elastic displacement during unloading

$h_r$ : The depth of residual impression

$i_{corr}$: Corrosion current

$E_{corr}$: Corrosion potential

$V_{corr}$: Corrosion rate

Z : impedance

$R_a$: arithmetic mean roughness

# List of Figures

## Chapter I



## Chapter II



## Chapter III

## Chapter IV

# List of Tables

## Chapter III



## Chapter IV

# Contents



## Literature Review

# Chapter I: Thermal Spraying Processes and Coatings

## Chapter II: Nickel-based Selffluxing Coatings



# Experimental Part

## Chapter III: Materials and Methods

# Chapter IV: Results and Discussion

# General Introduction

## General Introduction

Nowadays, with the increasing need to diversify and expand the industrial activities, the prime requirement for the industrialists is to increase the production and the performance of the industrial parts while decreasing their cost. The industrial parts have to resist internal and external solicitations. Among the solicitations that parts also undergo in service are the environmental aggressions. The environmental aggressions are a major cause of the damage of the materials constituting that parts. They are responsible for their degradation and can cause an alteration of their properties over time.

For the last few decades, the optimization of the properties and performance of parts in service has been the subject of numerous studies. The drilling tools required for mining and petrochemical extraction are one example. The specific properties required for their operation are such that their cost is extremely high.

The drilling conditions are draconian (hard soil, high temperature and pressure, aggressive environment) and require special qualities of the tool. This one that it works in percussion and in rotation or is solicited in friction, in abrasion and in corrosion. The strong mechanical and thermal gradients observed are not without consequences on the behavior of the materials that compose it and on their durability. These properties obviously depend on the constitution of the coating, the functional part of the tool and that of the substrate.

The objective of this thesis is to establish a deposition procedure to achieve wear-resistant coatings that can withstand the harshness of corrosive environments. This involves the production of thick nickel-based coatings of the order of 3mm by the flame spraying technique and then the evaluation of their metallurgical, mechanical and electrochemical characteristics, optionally to improve the performance of the X18 carbon steel.

For this purpose, we have subdivided the present thesis work into two major parts.

The bibliographic part is divided into two chapters, the first chapter deals with general information on the thermal spraying processes.

The second chapter is reserved for the state of the art that relates solely to the nickel based coatings.

The experimental part has two main chapters; the first is devoted to the experimental methods and techniques used to carry out this study and the second includes the experimental results with their interpretations.

# Literature review

# Chapter I :

# Thermal Spray

## I.1 Introduction:

The working components are usually prone to various surface related problems which commonly lead to their failure. Corrosion [1], erosion, and wear are the foremost examples. Overcoming all these inexorable phenomena particularly in the currently exploited harsh aggressive fields is still a tough challenge that ranks high. Since decades, great endeavors have been deployed to enhance the in-surface properties of the used bulk materials via applying coatings so as to offer more protection within a specified period of service life time [2, 3]. Currently, the so-called thermal spraying processes have satisfied the demands in a wide range of applications. They encompass numerous techniques enabling the obtaining of diverse coatings with totally unlike characteristics and with the possibility of monitoring the thickness of the deposited layers from the thin to the thick with or without affecting the microstructural state of the used substrates (Figure.1) [4]. In this chapter, we'll describe the different thermal spraying processes which are mostly used to perform coatings in their real industrial fields. We outline the main characteristics of each technique and we give some hints about the main features of the in-resulted coatings.

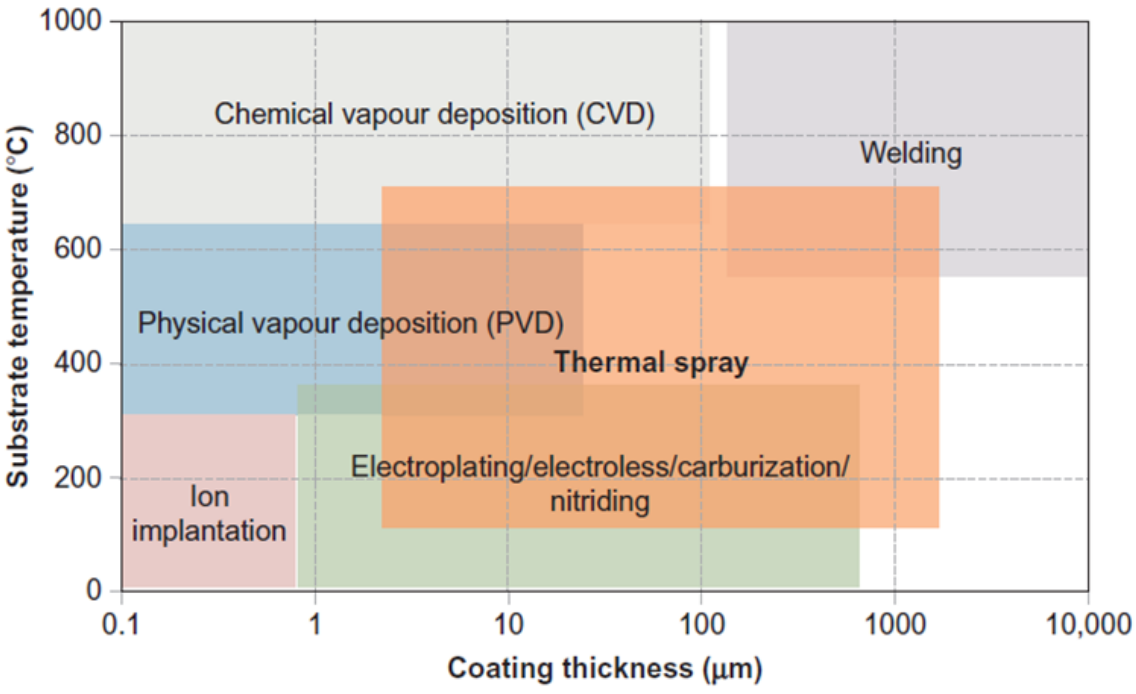


**Figure I.1- Influence of the surface modification processes on the substrate temperature [4].**

## I.2 Thermal spray:

Thermal spray is a generic term [3,5,6,7] for a group of surface-modification processes which allow to propel a melted, semi-melted or completely solid metallic, ceramic, composite or polymer materials by a gas stream to a properly prepared substrate [5,8,56]. As shown in Figure.2, thermal spray encompasses numerous techniques that can be classified into three broad families. The first uses combustion heat sources; namely the flame, detonation gun and high velocity oxygen fuel spray (HVOF) processes; The second uses electrical energy; either in plasma or in an wire arc spray, and the third is a recent extension to the thermal spray family and is known as cold spray, kinetic spray or hypersonic spray, which uses the energy that evolves from gas expansion [4,9].

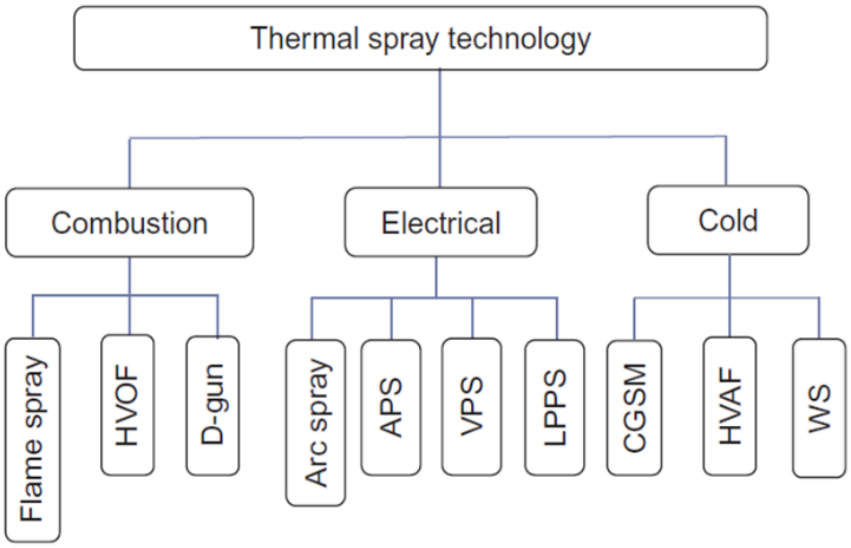


**Figure I.2- Classification of the thermal spraying techniques[4].**

## I. 3 Thermal spray processes:

### I.3.1 Flame spraying:

As surface treatment process, flame spraying has been used since 1910s [4] to wear the manufactured components and the reworked parts in various industrial sectors in order to extend their lifetime during their service period. The cost effectiveness and the simplicity of the flame spraying are the major factors behind its wide spreading [4,9]. This process allow to deposit a numerous type of materials as feedstock powders, rods or wires either in

molten, or semi-molten state including metals, ceramics, composites and polymers. Ceramics are almost available in the markets in rod form. Metals and polymers are usually commercialized as powders, and wires. There are two main flame spraying types that are actually employed: Powder Flame Spraying (FS-Wire) and Wire Flame Spraying (FS-Wire). The difference between the both reside on the design of the torch (see Figure 3). In the (FS-Powder), the powder can be axially or radially faded to the combustion chamber by the mean of a carrier gas. In the case of Wire Flame Spraying (FS-Wire), the wires and rods are pushed towards the interior of the combustion chamber using an electrical motor. The required chemical energy for melting the coating materials in both processes is generated by a combustion reaction of a fuel gas in the oxygen inside the torch. During the combustion process, the compressed air in the FS-Wire particularly surrounds the flame, allow to atomize the wire or rod tips and propels the melt in the form of a stream of droplets towards the prepared workpiece surface [10]. And with that, the droplets are accelerated with a velocity 3 times greater (150 m/s) than that of FS-Powder (50 m/s). As a consequence, the FS-Wire allow to attenuate a temperature 0.95 the temperature of the flame higher than that of FS-Powder. However, due to the heat dissipation the in-flight molten particles leave the nozzle with an initial temperature around 2000 °C. Practically, the spraying distance between the nozzle and the coated surface should be kept in the range of 120–250 mm. During the processing, the substrate temperatures achieve a maximum of 250 °C and up to 1000 °C for the self-fluxing coatings due to the post-spraying treatment [4,8].

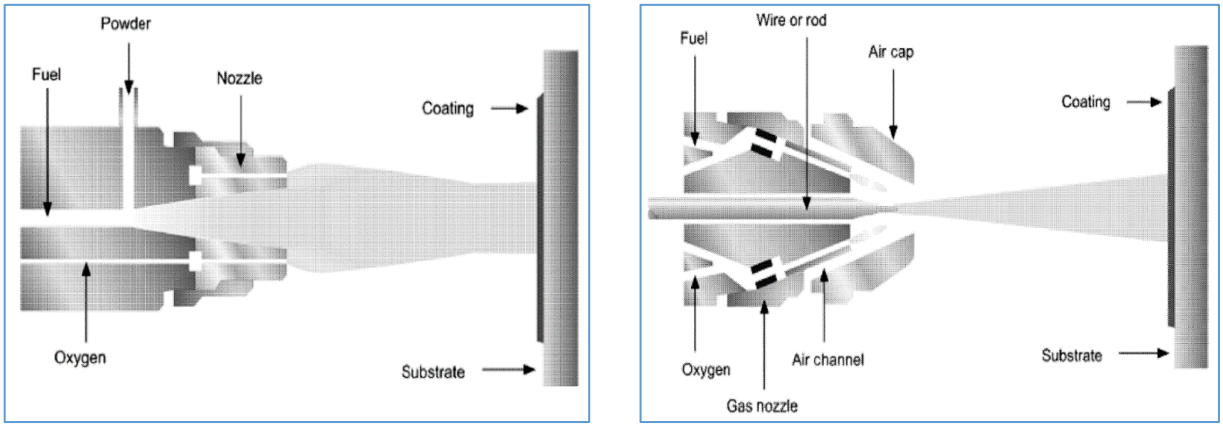


**Figure I.3- Principle of flame spraying using (a) powders and (b) using wire[10].**

The flow rates and pressures of the working gases depend on the type of the torch design. The wise adjustment of the oxygen to fuel mixing ratio before the processing is

mandatory to regulate the flame temperature and to stimulate the creation of an oxidizing or carburizing atmosphere. The oxidizing atmosphere can be formed when the ratio value is equal to the unit. Whereas, a ratio of 1.1 result in a carburizing one [8]. Using the acetylene as fuel, the flame temperature can exceed 3350 K. The combustion reaction of the acetylene in the oxygen is given by the following equation [11]:

$$C_2H_2 + \frac{5}{2}O_2 \rightarrow 2CO_2 + H_2O + 1259.85\ KJ.mol^{-1}$$

Lower temperatures under 3200 K can be reached by using other gases such as Hydrogen $H_2$, Ethylene $C_2H_4$, Propylene $C_3H_6$, and Propane $C_3H_6$. As depicted in the figure below, each of those has a critical oxygen to fuel ratio at which the combustion temperature reach its maximum value.

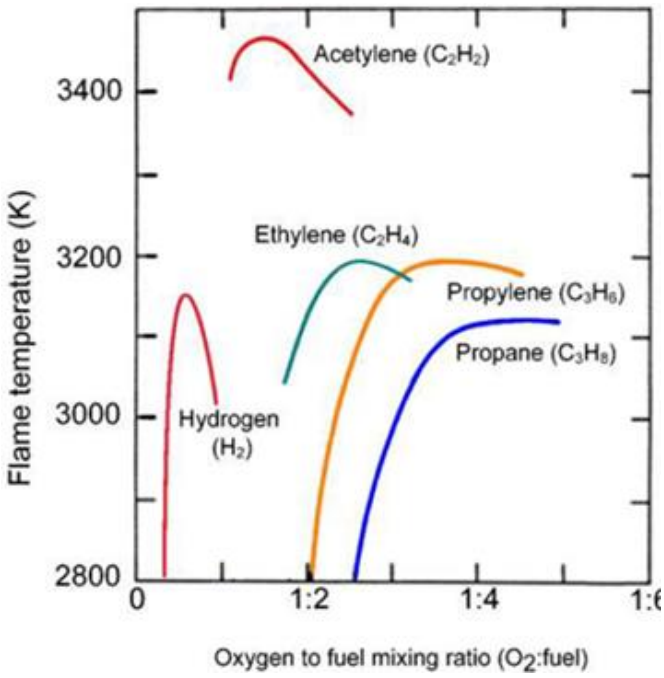


**Figure I.4- The variation of flame temperature as a function of oxygen to fuel ratio ($O_2$/fuel)**

Flame spraying provides rough coatings with relatively low density and are of about 100 to 2500 µm in thickness. Their adherence to the target whose strength depends on the type of the deposited material is insured by mechanical bonds. The bond strength determined using tensile adhesion test can reach 60 MPa for flame-sprayed NiAl alloys or even 70 MPa for self-fluxing ones. Typical values are in the range of 15 MPa for ceramics coatings to 30

MPa for metals and alloys. The coating build up is chiefly consisting of a porous lamellar microstructure containing towards 6% to 12% of oxide inclusions [12]. The appearance of the porous microstructure is ascribed to the consecutive flattening of the droplets on the target. Flame spraying porosity content fluctuates between 10% and 20%. Beside voids and porosity, unmolten particles can also be found inside the coatings when the particle size distribution is unfit and/or the particle injection is not optimized. Besides the benefits of the inhibition of the cracks propagations and lubricant role, the interconnected porosity severely impacts the coating anti-corrosion, and anti-erosion performances. The oxides are inevitably formed through the in-flight period due to the oxygen diffusion from the open atmosphere.

### I.3.2 Detonation-gun spraying (D-GUN):

This particular process has constituted the breakthrough of the 1950s and 1960s. It was developed by Union Carbide and the Paton Institute in Kiev latter. It's slightly similar to the flame spray. The process uses the confined combustion of a fuel gas in the oxygen to accelerate the powders along a long barrel (450–1350 mm) through a detonation wave (Figure.5). It allows to deposit powders with sizes ranging from 5 to 60 µm at spraying distances varying from 100 to 300 mm. The actual detonation systems can produce 100 detonation per second with flames that work at high speed. The fuels that are customarily used for detonation gun spraying are hydrogen, acetylene, propane and butane. The flame temperature may attain 4500 K if a proportion of 45% of acetylene is used. The particle velocity varies between 750 to 1000 m/s while that of the detonation wave may exceed 2930 m/s [8, 14, 15].

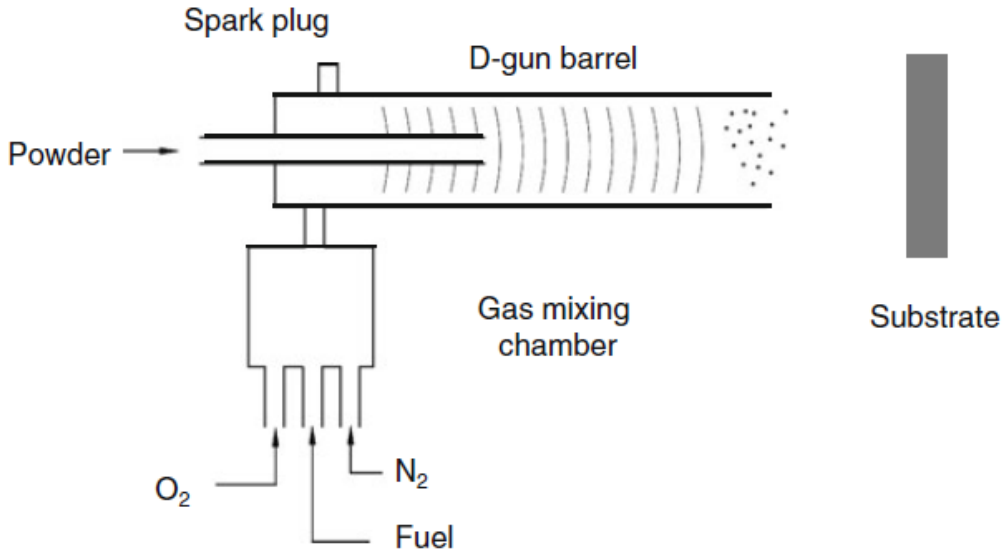


**Figure I.5- Schematic of a detonation gun torch [13, 14].**

The detonation gun spraying is able to create thin gas-tight coatings of about 300 µm in thickness. The sprayed coatings have a tensile bond strengths that vary between 83 and 70 MPa [8, 14].

### I.3.3 High velocity oxy-fuel Spraying (HVOF):

The high velocity oxy-fuel (HVOF) spraying is a combustion thermal spray process which was developed at the beginning of 1980s as an alternative to the detonation gun technique. It uses a selection of fuel–gas mixtures (including propylene, propane, hydrogen or natural gas for gas fuel led systems and kerosene for liquid fuel led systems) to heat and accelerate the feedstock materials axially through a consecutive combustion reactions (Figure.6). The HVOF torches are composed of three main zones: a mixing zone, a combustion chamber, and a nozzle. The combustion occurs in a pressurized chamber in which the feedstock materials can be melted either in an oxidizing or reducing environment. The high kinetic energy that results from the expansion of gases in the nozzle after combustion allow to accelerates the molten or semi molten particles from the barrel to the target at a velocity of about 550 m/s. the useful gases that are used for carrying the feedstock powders are usually argon and nitrogen. The injection of gases to the combustion chamber is usually done under a pressure between 0.3 MPa and 4MPa. The temperature of gases

depends mainly on the type of the used gases, the oxygen to fuel ratio, and the flow rate of the fuel gas [8, 14]. the flame temperature is around 3000 °C [59].

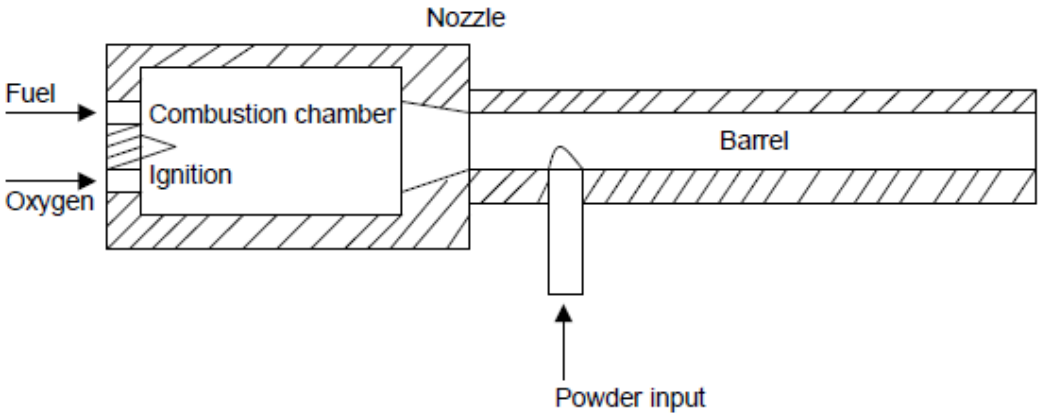


**Figure I.6- Schematic of an HVOF torch [8].**

High velocity oxy-fuel is a proven process that is used for many industries varying from the outer space applications to the deep sea technologies. This process can be used to build up metallic, ceramic or metal matrix composite coatings for anti-tribo-corrosion components. The HVOF process usually produces dense, and well adhered coatings which have high bond strengths (>69 MPa), low oxide content (< 2%) and a relatively low roughness for the as-sprayed finish (root mean square, ~3 mm). The HVOF coating are usually 0.5 mm thick and their density may achieve 99%.

### I.3.4 Wire arc spraying:

This spraying process was invented at first by Dr. Schoop in 1910s and it proved its success just after 1960s. It's well considered as the most efficient thermal spray technique. As depicted schematically in Figure 7, the technique uses two wires as consumable electrodes and a compressed gas to atomize and propel the coating material. When the electric current circulates through the wires, an electric arc forms leading to the formation of droplets between the wires' tips. These droplets are propelled by the atomizing gas toward the substrate. The temperature between the arc can reach 20000 K. The arc voltage is in the range of 20 to 40 V and the gas flow can be varied between 0.8 and 1.8 $m^3$/min. The spraying distance ranges from 50 to 170 mm [4,8,14].

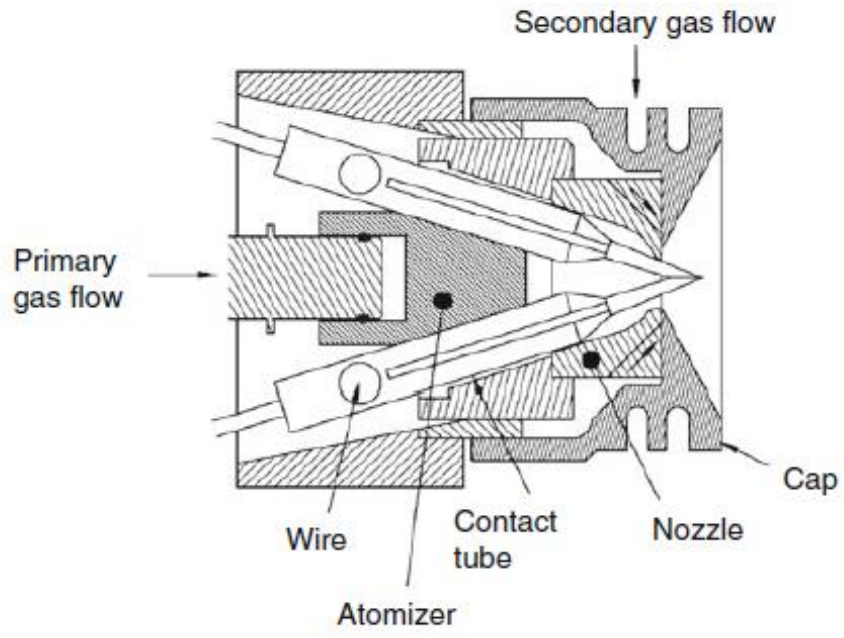


**Figure I.7- Schematic of an arc spray torch [29, 32].**

Coatings produced via arc spraying usually contain 10% to 20% of porosity. Depending on the nature of the deposited materials; the tensile bond strength varies between 10 and 70 MPa. The thickness of arc spray coatings ranges from 100 to 2000 µm [8].

### I.3.5 Plasma spraying:

In the plasma spraying (Figure.8), the powder is introduced using an ionized gas or a gas mixture. The ionization of gas or gases is insured by the continuous generation of electric arc discharge that occur between copper or graphite anode and thoriated tungsten anode. The ionization of gas or gases produces a warm plasma jet which propels the feedstock material toward the substrate. Depending on the operational conditions, the plasma spraying can be divided into four main classes: arc plasma spraying, air plasma spraying, vacuum plasma spraying, and low pressure plasma spraying. Plasma spraying technique allows to propel powders having 20 to 90 µm in size from spraying distances in the range of 30 to 160 mm [4].

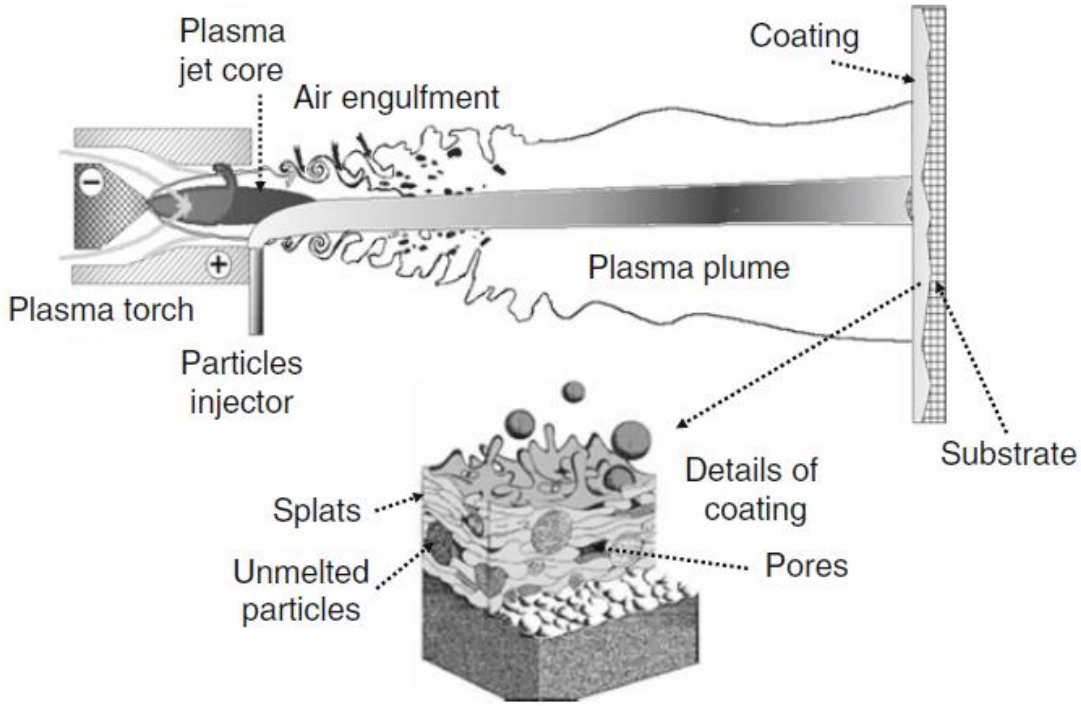


**Figure I.8-functioning principle of plasma torch [30,32].**

For the vacuum plasma spraying technique, the coating thicknesses may vary between 150 and 500 µm. The coatings have a maximum porosity content around 2% and the tensile bond strength may surpass 80MPa. For air plasma spraying, the tensile bond strength may reach 70 MPa for NiCr alloys and is in the range of 15 to 25 MPa for the ceramics deposited on metallic substrates. The amount of porosity fluctuates between 1% and 7 % [8].

### I.3.6 Cold spraying:

In this process developed in 1980s, the kinetic energy of a compressed gas is used to accelerate the feedstock powders below its molten temperature. The gas is preheated up to 700 °C and compressed so that it reaches supersonic velocities around 1500 m/s when it exits through a convergent- divergent Laval nozzle (Figure.9). The pressure of the stream is between 2 and 2.5 MPa. The internal diameter of the throat is in the range of 2 to 3 mm. The

used gases are usually $H_2$ and $N_2$ or their mixture. Using this technique, the un-molten particles take its trajectory toward the substrate upon which they plastically deform at velocities between 500 m/s and 1500 m/s. The efficiency of the process may exceed 90%. Cold spraying can be classified into three main classes: Cold-gas spraying method, high velocity air fuel, and warm spraying [4,14].

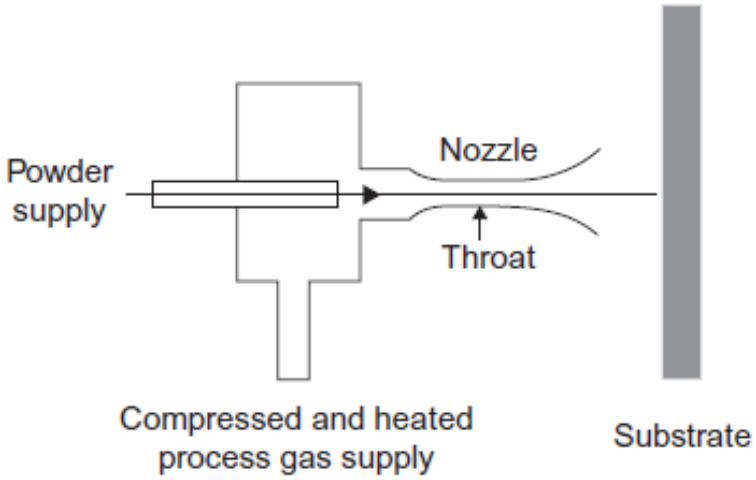


**Figure I.9- Schematic of a cold spray torch [14, 16,17].**

Cold spraying produce well adhered coatings when they are deposited on metallic or ceramic substrates. For Cu and Al, the reported amounts of porosity of cold gas spraying method were 4.5% and 3.7% respectively. The tensile bond strength was 33 MPa to 35 MPa for Al and 44 MPa for Cu. The deposits may contain also a little amount of oxygen. The oxygen content varies between 0.1% and 0.12%. The coating thicknesses are in the range of 250 mm to 650mm [8].

### I.3.7 Coating build up

In the thermal spray, the coatings are obtained through the successive flattening of particles inflight on the substrate or on the previously deposited layers. As a consequence of flattening, the microstructure of coatings is typically lamellar and porous. It contains thin individual strips called splats and a certain amount of voids, oxides and unmelted particles (Figure 10 and 11).

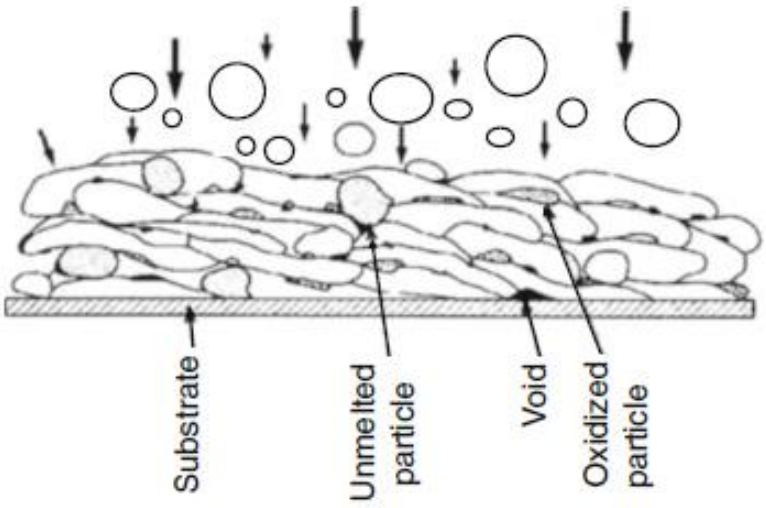


**Figure I.10-Schematic cross section of thermally sprayed coatings[59]**

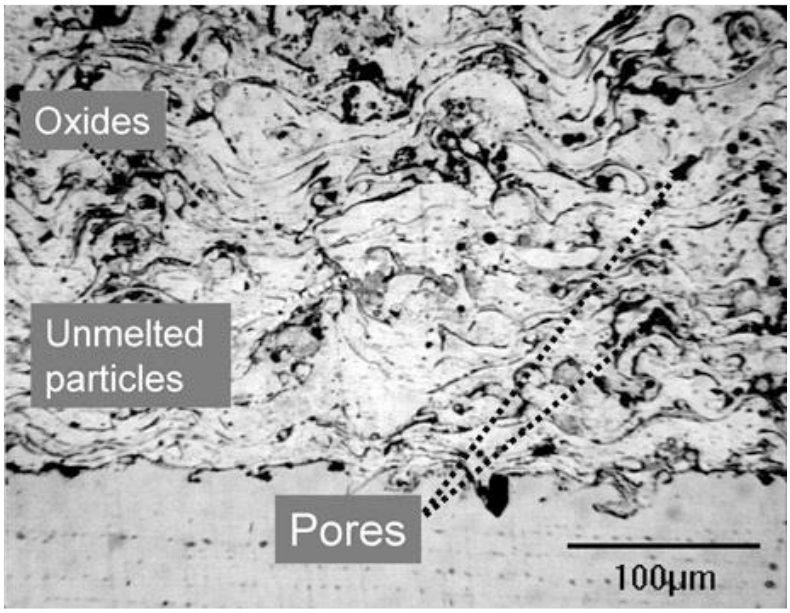


**Figure I.11- Microstructure of a 304L stainless steel coating deposited by APS on a low-carbon steel substrate**

The characteristics of the microstructure depend, on the one hand, on the parameters of the particles at impact (speed, size, melting state and chemical state) and on the other hand, the parameters of the substrate (material, roughness, chemical state of surface and temperature) [18-22].

Kudinov et al. [61] has classified the different form of splats that can result from their interaction with the substrate on the moment of impact. The figure 12 represents completely melted particles (from 1 to 6), completely melted particles that contain gaseous hollow (from 7 to 11), preheated particles which are at the beginning of evaporation (from 12 to 14), a particle which is melted on its surface (15) partially melted particles with a solid core (from 16 to 19), particles with molten core that are solidified at the surface (20, 21, and 30), particles which are solidified at the surface-and has a solid core and a melted middle layer (from 22 to 27), and solid particles ( from 28 to 29).

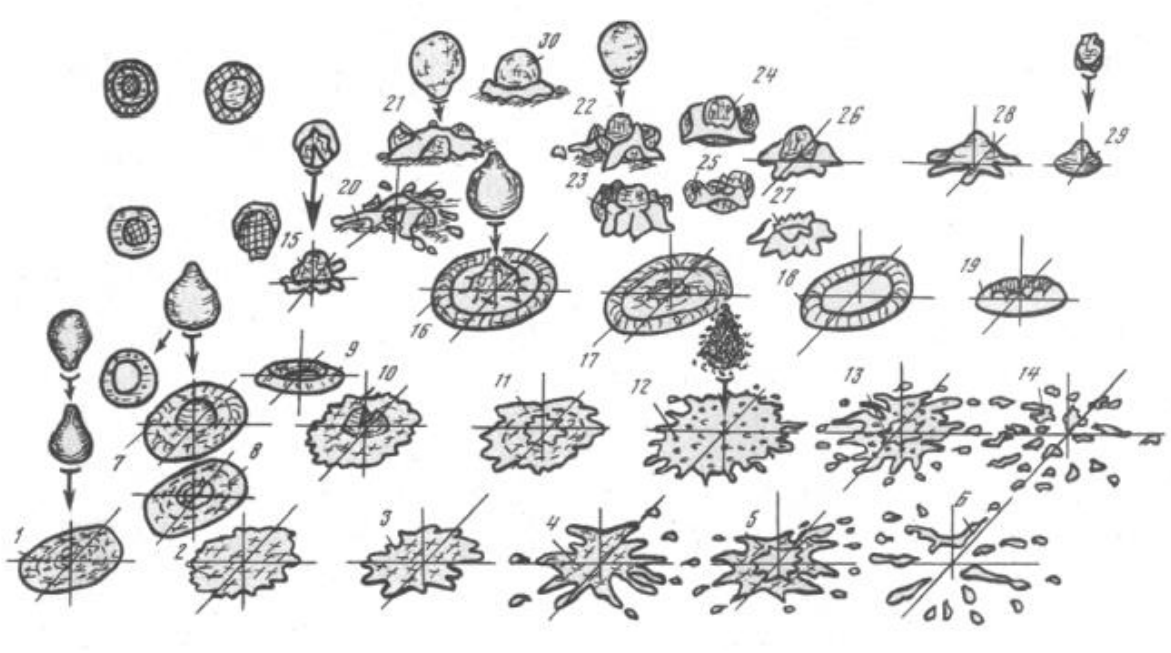

**Figure I.12- illustration of the different forms of splats that result from their interaction with the substrate [61].**

This form of a splat differs from each other depending on the type of particle inflight, its velocity and temperature, and also its wettability. The impact of particle inflight depends on the geometrical profile of the substrate and its temperature.

The passage of the molten particles inflight to the solidified splat on the substrate can be divided into three stages which can be correlated with one another according to the cooling kinetics of the splat: the initial impact, the flattening of the particle and its solidification. The impact usually takes a few tens of nanoseconds while the flattening of particles and solidification of a splat occurs in few microseconds [23-24].

The temperature, the velocity, and the diameter of both particles inflight and spray jet are not enough to predict what the final properties of a thermally sprayed coating could be. The final properties of coatings are linked to the flattening and the solidification of particles impacting the substrate or the previously deposited layers. They are related also to the splats layering and to the real contact between splats and substrate or the previously deposited layers [25-26].

Preheating the substrate below a critical preheating temperature called transition temperature ($Tt<0.3Tm$) (Tm is the particle melting temperature) desorbs the adsorbates and condensates present at the substrate surface and create a rough oxide layer that increases the adhesion of coatings on the metallic substrates. When the substrates are preheated above the transition temperature, the splats are disk shaped and the contact area between the flattening particle and substrate can reach 50%-60%. Without preheating, the evaporation of adsorbates and condensates provide high gas pressure that lifts the flattening liquid and results in fingered splats. The contact area is then near 10%-15% [25-27].

## I.4 Comparative analysis between the thermal spraying techniques

The different thermal spraying processes can be represented on a diagram (Figure 13 and 14) characterizing the energy transfer scales (thermal and kinetic) between the enthalpy source and the particles. It can be seen that the VPS technique is positioned as a method for achieving a significant particle velocity of the order of 600 m/s, while the plasma temperature can be up to 20000 ° C. The velocity of the particles has a direct influence on the characteristics of the deposit such as its density and its adhesion. On the other hand, the maximum temperature of the enthalpy source imposes the limit of use of certain materials whose melting temperature is high. The combination of these two characteristics demonstrates the interest of using the LPPS technique [28].

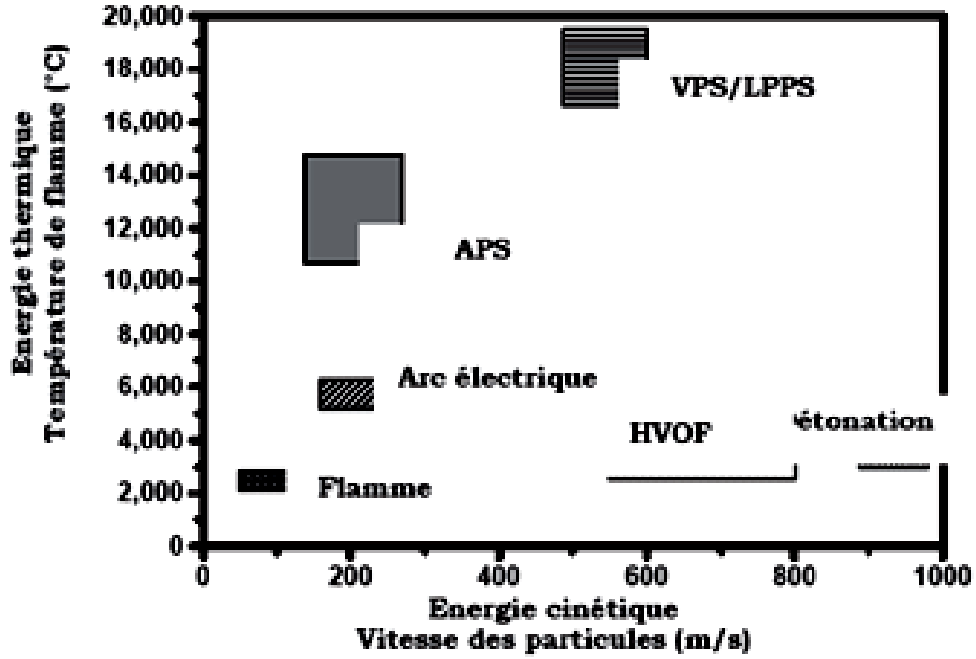


**Figure I.13- Characteristics of the different thermal spraying techniques [28].**

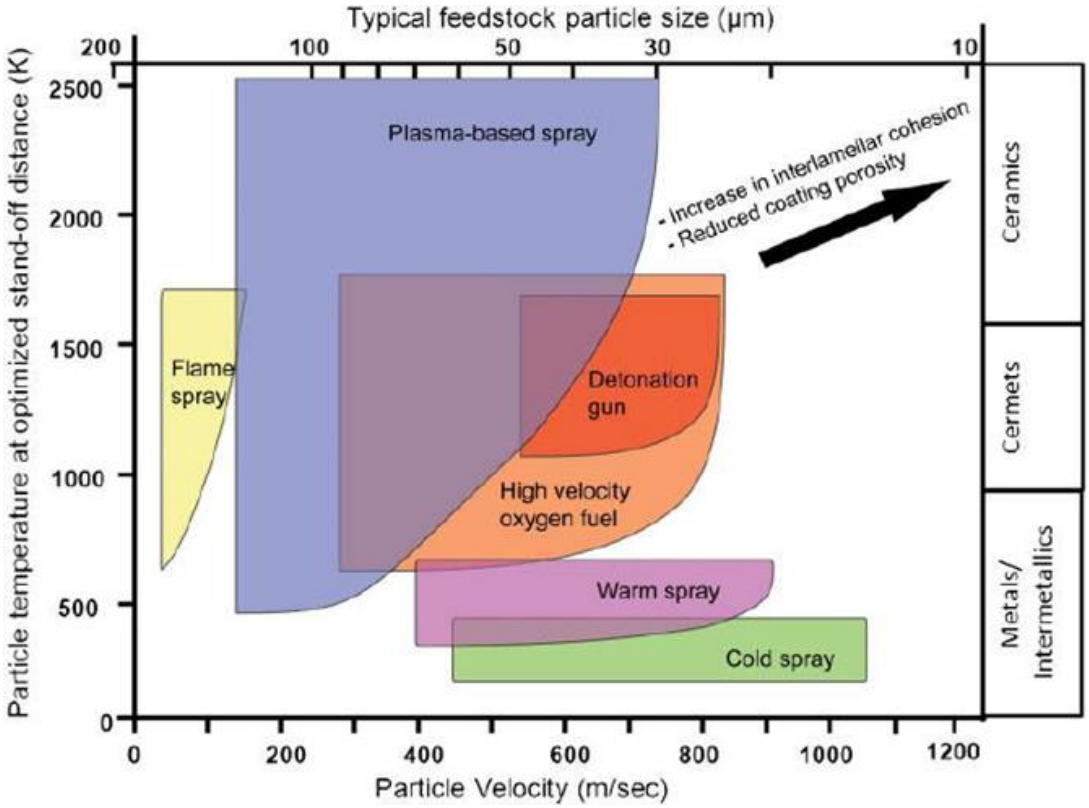


**Figure I.14- Particle temperature and velocity of thermally sprayed coatings.**

## I.5 Characterization of thermally sprayed coatings

### I.5.1 Microstructure:

During the spraying, the successive flattening of droplets on the substrate gives to the thermally sprayed coatings a layered microstructure with lenticular shape. This microstructure is composed of splats which are parallel to the interface. The coatings grow with anisotropic properties due to this particular microstructure and directional solidification.

### I.5.2 Adhesion and adherence:

As we have mentioned before, the quality and the microstructure of the coatings depend on various parameters related to the projection of particles. The surface preparation of the substrates is also an important factor that affects the final properties of the deposits including adherence. If different surface preparation conditions exist, various interface forms can be obtained and, therefore, different value of adhesion and various levels of adhesion can be found.

### I.5.3 Adhesion mechanisms:

Adherence and adhesion are two basic concepts that should be distinguished. Adhesion is the result of a mechanical separation test. It characterizes the breaking strength of an assembly. For an assembly to be durable and efficient, it is necessary to obtain an optimal level of adhesion [44].

Adhesion is defined as a state in which two surfaces are cohered together by physicochemical bonds acting at the interface. A number of interfacial phenomena are responsible for the adhesion mechanism [33], the main ones are the following:

#### I.5.3.1 Interatomic and intermolecular bonds

The interatomic chemical bonds are bonds of high energy. They are covalent, metallic, ionic or mixed. They can be created at the interface between two materials if their chemical affinity is high [34]. They are of short spans and require an intimate contact which is free of impurities between two surfaces. As the chemical reactions do not always occur, places are available for the creation of physical bonds of low energy. These physical bonds result from Wan der Waals forces or hydrogen bonds.

**Table 1- energy associated to the physical and the chemical bonds [44].**

| Bond type | | The associated energy (kJ/mol) | span (nm) |
|---|---|---|---|
| Physical bonds | Wan der Waals bonds | 2 - 15 | ≤ 1 |
| | hydrogen bonds | 10 - 40 | 0,2 |
| Chemical bonds | covalent | 150 - 950 | 0,1 - 0,2 |
| | ionic | 400 - 800 | 0,2 - 0,3 |
| | metallic | 100 - 400 | 0,3 - 0,5 |

### I.5.3.2 Wettability

Wettability is defined as the ability of a liquid to spread over the solid with which it is brought into contact. During the thermal spraying, this phenomenon occurs during the flattening of the melted particles on the substrate. Good substrate wettability is required to get good adhesion [34]. The more the surface tension of the substrate is high, the more the previous condition is respected.

The adhesion energy $W_{adhesion}$ is related to θ representing the contact angle of the liquid with the substrate and γ the interfacial tension by the following relation:

$$W_{adhesion} = g\ (1+ \cos \theta)$$

The more the droplet is spread on the surface of the substrate, the more the adhesion energy due to wettability is steady. The wettability is assured by Wan der Waals forces.

### I.5.3.3 Diffusion mechanism

Diffusion is an interfacial phenomenon which may occur between two materials according to their mutual solubility. A chemical composition gradient may be formed in the case of metals. Diffusion requires a sufficient heat energy. The required energy can be provided by maintaining the temperature of the substrate. During spraying, an oxide layer is commonly formed on the surface of metal substrates. This oxide layer may be advantageous to the adhesion of the coating or harmful if the layer is fragile. The substrate preheating generally contributes to the formation of an interphase layer conducive to the flattening of the splats [35]. However, the control of the thickness of this oxide layer, by controlling the preheating temperature and

the time, is necessary in order not to reach great thicknesses causing delamination because of a layer too much fragile.

### I.5.3.4 Mechanical anchoring

After spraying and during the cooling phase, the mechanical anchoring results from the contraction of the particles impacting the irregularities of the substrate surface [33,36]. Adhesion of plasma sprayed coatings for example is attributed to a predominant mechanical anchoring.

The mechanical anchoring depends strongly on the roughness morphology of the substrate surface. The presence of asperities on rough substrate greatly reduce the flattening of particles (Figure 15). The splat therefore has a jagged edges. The more thickness of splat is greater, the more its cooling is slower, the more the contact splat/substrate or splat/splat is better [37].

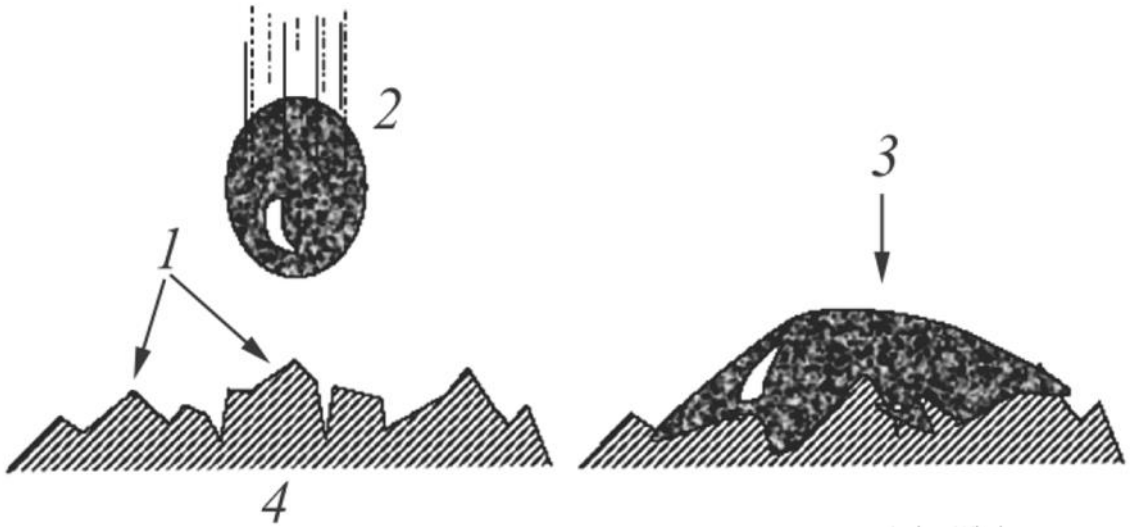


**Figure I.15- Schematic illustration of adhesion of a droplet to the asperity of a substrate [60]: (1) asperities, (2) particle in flight, (3) particle mechanically anchored to the asperities of the substrate, (4) substrate.**

After a number of experiments conducted on glass and molybdenum substrates coated with molybdenum, an author has proved that the splats can spread out easily on a smooth substrates, however just 10 % of the splat remains adherent [39].

The pre-surface treatment are able to increase the roughness of the substrates and the increase in the roughness of the substrate can improve the adhesion of sprayed coatings [45]. The mechanical anchoring contributes to the increase of adhesion on a rough substrate (Ra> 0.5 μm). If the substrate surface is smooth (Ra <0.05 μm), the diffusion or wettability are the dominant mechanisms which can insure adhesion [38]. The mechanical anchoring is closely linked to the wettability that is favored by a higher substrate temperature. The splats look less compact and more anchored in the rough surfaces if the substrate is preheated.

It has been also has demonstrated that the arithmetic mean parameter Ra is not enough to correlate mechanical adhesion to the other parameters that characterize the surface roughness. A new parameter called Skewness has been introduced to correlate it to the mechanical adhesion [40].

A number of authors propose that the size of the asperities can be adapted to the diameter of the particles inflight in order to improve the adhesion [41].

**I.5.4 Residual stresses:**

Residual stresses are the stresses that exist inside a material in absence of external applied loads. These stresses remain within the material even if the cause of the appearance of stresses has been removed (external forces, inelastic deformations, heat treatments). In the case polycrystalline material, the deformations which result from the residual stresses make it possible to distinguish 3 types of stresses:

- The first order residual stresses are called macroscopic stresses. They extend over a sufficient number of grains and reflect the mean value of the residual stresses present in the material.
- The Second order residual stresses correspond to the average of stresses within a grain.
- The Residual stresses of third order are the local stresses, which can differ within a grain.

During the thermal spraying, and during the formation of the coating, the microscopic and macroscopic residual stresses are mainly due to [42,43]:

- Intrinsic, quenching or deposition stresses that are microscopic and has a tensile nature. They are produced in the sprayed particles as a result of the shrinkage of

each particle during its cooling from its melting temperature to the substrate temperature.

- Compressive metallurgical stresses where the sprayed particles can undergo metallurgical transformations and can be subject to a volume change.
- Thermal stresses generated due to a thermal expansion coefficient mismatch or due to a difference on Young's and Poisson's modulus between the coating and the substrate.

### I.5.5 Wear:

In the case of coatings, two mechanism that are due to wear can be cited here as main damage processes: abrasive wear and adhesive wear

#### I.5.5.1 Abrasive wear:

Abrasive wear occurs when pressed hard particles are made to slide against a soft surface [48,49]. We distinguish two types of abrasive wear that are due to two unalike contacts [50]:

• The two-body abrasion (Figure 16), in which a hard particle rubs against the surface in return, and produces on the latter a number of grooves parallel to the direction of sliding;

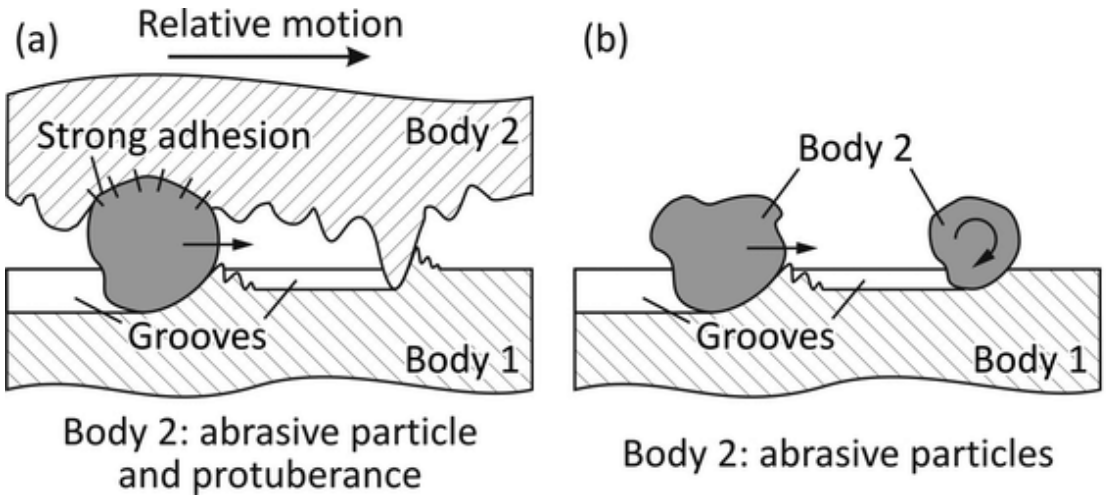


**Figure I.16- Two-body abrasion process [55].**

• The three-body abrasion (Figure 17), where wear debris and particles are trapped between two surfaces, and are free to slide. This type of contact can cause a random pattern on the surface, which has been strongly deformed through a plastic deformation.

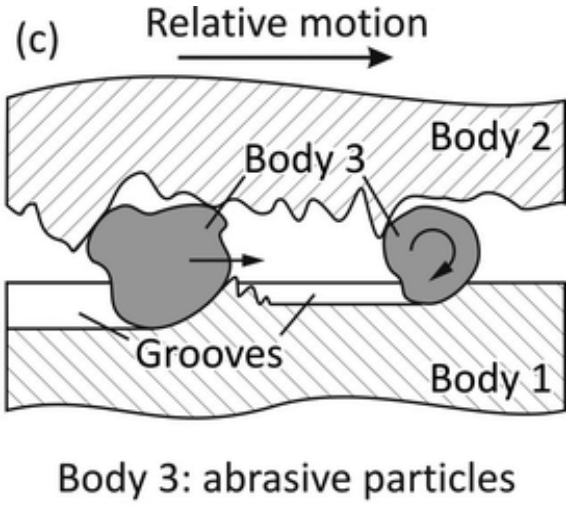


**Figure I.17- Three-body abrasion process [55].**

Different modes of wear have been proposed to explain the removal of material from a surface during abrasion, such as plowing, micro-cutting, and wedge forming [51-53]

### I.5.5.2 Adhesive wear:

When two solid surfaces are brought into a sliding contact, they will adhere one to another due to a localized bonding at the contact area. When the surfaces are driven to move, the localized bonding resist to the relative displacement of the surfaces. Therefore, the removal of material will take place by one surface pulling the material out of the other surface (Figure 18). The removal of material through this process is called adhesive wear [54].

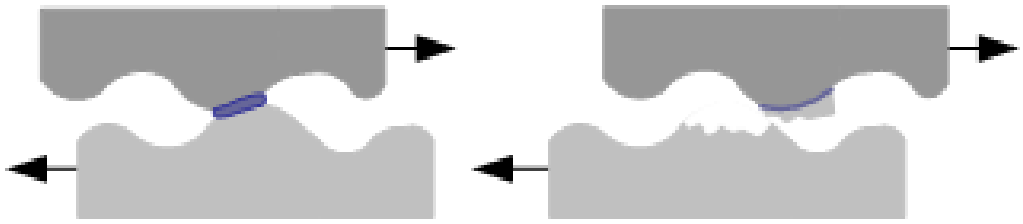

**Figure I.18- Adhesive wear.**

### I.5.6 Hardness

The hardness of the thermally sprayed coatings is generally lower than that of the cast and wrought materials. This is due to the heterogeneous nature of the microstructure of the coatings which further contains an amount of voids and oxide beside the coating material. The hardness of the thermally sprayed coatings can be affected by the nature of the atmosphere in which the coatings were performed. It's commonly known that the hardness of a material will

be higher if the latter is sprayed in the open atmosphere and lower if the material is sprayed in an inert environment [57, 58]. The presence of oxide may increase the hardness and decrease the coatings' strength which can lead to an alteration of the coating performance. The hardness values may differ from one region to another due to a variance in the residual stresses within the coating.

## I.6 Pre-surface treatments of substrates

So that a coating can adhere to the surface of a substrate, preliminary treatments of substrate are often required. These surface preparation treatments make it possible to clean the treated surfaces and / or to maintain a sufficient roughness to have a good adhesion. Performing thermal spray coatings is usually preceded by a number of operations. These operations are essential and must be done in a well-established order to improve adhesion.

### I.6.1 Degreasing

Degreasing is necessary for workpieces in order to be able to coat them. They must therefore be freed from production-related greasy deposits such as greases, lubricating oils or corrosion protection oils. This happens with so-called degreasing agents. These may be organic solvents, or even non- halogenated agents. As an alternative, there are still aqueous solutions. For environmental reasons, almost only the latter are used in recent times. However, they are not as universally applicable as organic solvents and must therefore be tailored to the specific process.

Degreasing is possible in the acidic to the alkaline range, with the extreme agents to be replaced by approximately neutral degreasing agents. However, this requires a higher concentration of wetting agents and surfactants. However, this disadvantage is compensated by a better environmental compatibility, since the wastewater treatment can be done more easily and inexpensively. In addition, they are able to saponify animal and vegetable fats; The wetting agents dissolve non-saponifiable residues in very fine particles.

In order to economically carry out a degreasing, there are various plants. The degreasing agent can be sprayed directly onto the workpiece by means of nozzles, whereby the mechanical effect is achieved by the chemical action. However, if the workpiece surface is difficult to reach due to complicated shapes, it can be dipped in a degreasing agent. In this process, the energy requirement is lower, but there is no mechanical removal of the residues. To solve this problem,

ultrasound is also used, which creates micro and macro turbulences to remove residues in the smallest cracks and holes. In addition, the chemicals can be utilized much better here by cascading the immersion baths and the water consumption can be significantly reduced.

### I.6.2 Sandblasting

Sandblasting (Figure 19) is a cold abrasive treatment of workpieces that modify the geometrical profile of their surface under the impact of sand or other abrasive powder which are sprayed with an air stream, and during hydro-abrasive treatment with a stream of water or other liquid. For the first time, this treatment process was patented by the American Benjamin Chu Tilgman (1821–1901) in 1870 (US patent 108408).

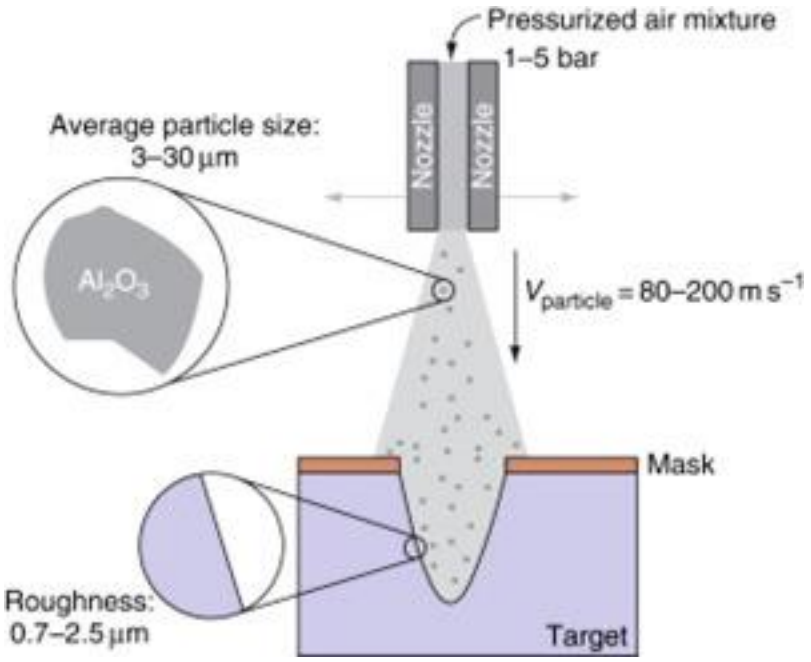


**Figure I.19- Schematic of grit blasting using alumina as abrasive particles [62].**

During abrasive blasting, abrasive particles are accelerated from the blasting machine with the help of compressed air energy. In order to ensure effective cleaning through abrasive particles and compressed air, professional skills, high-quality equipment and quality control are required. Each element affects the performance of the entire system. When cleaning, unnecessary materials are removed, the surface of the material is hardened and becomes prepared for coating. Abrasive blasting from metal structures removes old paint, rust and other contaminants. In addition, during blasting, the secondary scale is removed, which is formed on the new steel.

Angular particles of abrasive give a rough surface and create a profile, or notch. Most paint manufacturers indicate what the profile should be in order to ensure effective application of their products.

When abrasive blasting of aluminum, titanium, magnesium and other metals remove the results of corrosion and, depending on the selected abrasive and pressure, mark the profile.

New, softer types of abrasive (including plastic), as well as special low-pressure abrasive blasting equipment are used for the dry method of removing coatings from modern composite materials. This allows you to clean planes, helicopters, cars, trucks and boats without using abrasive blasting, which can disrupt the surface structure. In addition, the transition to the dry method of cleaning the upper layers eliminates the possibility of exposure to working toxic chemicals used in cleaning, and eliminates the costs associated with the disposal of hazardous waste.

Abrasive blast cleaning options are varied. Since new materials are regularly invented in industry and the need arises to process new surfaces, manufacturers of abrasive blasting equipment and materials have to continuously improve their technologies and equipment.

### I.6.3 Pickling

Pickling is a world that refers to a chemical operation which is used to eliminate the inorganic impurities and oxide layer from the surface of a material through acid or alkali solutions.

In case of metallic materials, this process is one of the methods commonly employed in order to make the metal surface suitable to be covered by another metal. After pickling, the treated surface becomes porous and allows the other metal to firmly bond with the surface of the underlying one. The surface is thus cleaned of rust residues formed by hot-rolled steel products, surfactants (soaps that increase wettability) and corrosion inhibitors, the calamine, the rolling flake, or any other chemical substances.

Pickling can also be used for the preparation of steel surfaces on which an anticorrosive and protective coating is to be applied. It is also used to prepare steel bars and tubes in wire drawing machines as a preliminary operation to improve the final result. In this case sulfuric acid is used for low alloy steels and hydrochloric for stainless steels.

Pickling of steel pieces is carried out by immersion of hydrochloric acid or sulfuric acid, but also phosphoric acid, nitric acid and hydrofluoric acid, at high temperature. For the pickling of hot-rolled low-carbon steels, sulfuric acid is generally used.

During pickling, corrosion inhibitors are normally introduced to control the acid attack on the areas of metal which are naked because they are deprived of the oxide layer more quickly than the others.

The pickling operation, besides being of a chemical nature, can also be of an electrolytic nature where the steel constitutes the anode or the cathode in an acidic electrolyte, through which the current passes.

# Chapter II :

# Nickel Self-fluxing Alloys

## II.1 Introduction

In oil and gas industry, the research for inexpensive versatile materials with a long longevity has become an essential task to increase the drilling bits efficiency and to alleviate the impact of the unsteady oil prices fluctuations on the production progress. The nature of the encountered rock formations and the severity of the operational drilling conditions are decisive factors in the choice of materials that best matches the requirements. Therefore, one cost effective way of improvement is to develop a new generation of metal matrix composites that can adapt in various harsh fields due to their upgraded performance.

Over the past decades, tungsten carbides cermet, containing as binder phase a cobalt based alloy, were the materials that had been settled to lessen the degradation of the implemented PDC cutters and to protect the drilling bit body against corrosion and erosion. In either sintered or in a sprayed coating form, these materials have shown high anti-tribocorrosion properties combined with excellent toughness, hardness and strength. Their characteristics may be improved either by varying their chemical composition and the nature of the processing techniques, or by applying post-processing treatments. This improvement possibility had put them forward as exceptional candidate materials for the extreme drilling operations.

More recently, and beside the ongoing optimization on this kind of cermet, the fierce critics beyond the noxious cobalt effects on health and environment have promoted the exploration of novel alternatives that can exhibit more enhanced features and assure better functionality to the sintered and the coated parts. However, owing to the remarkable similarities between cobalt and nickel, in term of their physical properties, and the gap between their prices, the nickel selffluxing alloys reinforced with tungsten carbides have won the favor.

## II.2 Microstructure and hardness of nickel selffluxing coatings

Reinaldo and D'Oliveira [1] showed that in the case of Colmonoy coatings deposited via plasma transferred arc process, the chemistry of the used steel substrates has a strong influence on coating performance. Indeed, a lower wear loss was measured on the coatings which were deposited on carbon steel plates. Comparatively to carbon steel plates, It has

been also demonstrated that the low thermal conductivity of AISI 304 stainless steel substrates result in a greater dilution and low solidification conditions, which lead to the formation of shallow and wider coatings with lower hardness. Additionally, the study proved that the increase in the current increases dilution and the use of low travel speed decrease the heat input and produce thick coatings with lower dilution. Depending on the deposition parameters, the microstructure of coatings may be of eutectic, dendritic or martensitic type. The more the dilution is low, the more the microstructure is complex, the more the coating is harder.

Gil, et al. [2] examined the microstructure of NiWCrBSiC coatings processed on 1020 steel substrates using the HVOF technique. The results revealed that the coating consists of a multiphase microstructure with inhomogeneous distribution of soluble elements in a $\gamma$ Ni matrix. The coatings also contain a set of hard phases embedded in the nickel matrix. These hard phases were : borides of about 0,35 µm in size ($Cr_5B_3$, $Cr_{18}W_{32}B_3$, $W_5(B,Si)_3$, $B_{305}Si_{8,44}$ and $B_4Si$), carbides (including $M_{23}C_6$ , where metals (M) are Cr, W, Si and Ni), silicon carbide ($C_{0,17}Fe_{0,81}Si_{0,02}$), tungsten carbide ($W_3C$), silicide ($Ni_2Si$) and trimetallics ($Ni_{29}Cr_{0,7}Fe_{0,36}$). As it was mentioned, the presence of borides was not reported in the literature due to their small size.

Hemmati, et al. [3] concluded that the rapid cooling rate promotes the nucleation and the growth of floret-shape mixtures of nickel and chromium borides $Cr_5B_3$ through a metastable reaction. They have also established that the proportion of NiBSi eutectic is influenced by the type of borides and can be affected by varying the amount of boron that remain in the melting pool. The peritectic transformation of the chromium borides CrB begun with the precipitation of primary chromium borides CrB or floret-shape mixtures at high cooling rates followed by a consecutive precipitation of $Cr_5B_3$ and $Cr_7B_3$ and by the formation of nickel solid solution dendrites and NiBSi eutectic.

Rodriguez, et al. [4] demonstrated that the post heat treatment using either oxy-acetylene flame , vacuum or argon atmosphere can significantly affect the microstructure and increase the hardness and the density of NiCrBSiW (Colmonoy 88) coatings deposited via HVOF process. The authors inferred that the post heat treatment improve adhesion by improving metallurgical bond between the coating and the substrate. The study revealed

that , prior the post treatments, the coatings mainly consist of nickel solid solution matrix in which chromium tungsten carbides and borides, and a tad of nickel silicides were precipitated as second phases. After oxy-acetylene flame treatment, the amount of porosity decreases and the hardness of coatings increases as a result of the precipitation of new borides and silicides. The samples treated in vacuum atmosphere exhibit lower microhardness and porosity than the samples treated with oxyacetelene flame. The treatment in argon atmosphere engender a morphogical change that causes dissolution and dilution of hard phases which result in lower microhardness.

Tokarev [5] studied the heat treatment of plasma sprayed coatings in a salt bath by the electrocontact method and by a plasma quasi-laminar jet. The author inferred that the use of intense heat sources increases the efficiency of deposition and the treatment of the coatings.

Serres, et al. [6] proved that with diode laser source associated with an APS plasma gun induce a laser remelting that densify the deposits and promote the formation of dendritic microstructure. The laser remelting contribute to the increase of adhesion, hardness and elastic modulus of Ni-based self-fluxing alloy coatings and make it an alternative to electrodeposited hard chromium as the Ni-based self-fluxing alloy coatings can exhibit better mechanical characteristics for a specific laser power density.

Zhang, et al. [7, 8] confirmed that the addition of tungsten carbides decreases the size of the dendritic crystal and the eutectic. They distinguished three different zones: the heat-affected zone, the interface, and the laser-alloyed zone.

Liyanage, et al. [9] showed that the coatings obtained via plasma transferred arc welding exhibit a multiphase microstructure consisting of Ni dendritic phase with harder Ni+$Ni_3B$ or Ni+$Ni_3Si$ eutectics and Cr-based borides and carbides (CrB, $Cr_3C_2$ , and $Cr_7C_3$ ) which occupy the interdendritic sites. They demonstrated that the change in chemical composition of the NiCrBSi alloy could disturb the formation of different phases. Indeed, the proportion of the dendritic phase decreases and that of chromium carbides and borides increases if the Cr, B, Si, and C content increase. The hardness of NiCrBSi coatings depends the amount of Cr containing phases and the volume fraction of the interdendritic carbides and borides. The hardness was found to increase with the increase of the volume fraction of eutectics

and Cr containing phases. It was found also that the Ni dendrite, interdendritic, and Cr-containing phases had an average hardness around 405, 860, and 1200 HV respectively.

Sudha, et al. [10] conducted a microstructural studies on Ni-Cr-Si-B overlays deposited on AISI 304L Stainless Steel via a plasma transferred arc process. The authors revealed the existence of three regions in the overlays. These regions depends on the distance from the interface. The first region is adjacent to the interface. It has a eutectic structure having γ Ni+$Cr_2B$ eutectic constituents. The second region contains chromium carbides of $Cr_7C_3$ or $Cr_3C_2$ type and $Cr_2B$ chromium boride type in γ -Ni matrix. The third region has a high volume fraction of needle shaped chromium carbides. These region had hardness values of about 300 VHN, 475 VHN and 700 VHN respectively.

Sidha, et al. [11] characterized the performance of four type of thermally sprayed HVOF coatings on Fe-based superalloy: NiCrBSi, $Cr_3C_2$-NiCr, Ni-20Cr, and Stellite-6. The study showed that the coatings had a layered microstructure. For NiCrBSi, $Cr_3C_2$-NiCr, Ni-20Cr, the principal phase was a nickel-base face-centered cubic phase while in the case of Stellite-6 coatings, the main phase was a face-centered cubic Co-rich metallic matrix. The coatings contain spinal oxides in the form of intersplat lamellae and globules parallel to the substrate. The coatings are also characterized by the presence of inclusions, porosities (<2%) and unmelted or partially unmelted particles. The $Cr_3C_2$-NiCr coatings have shown higher hardness values of about 900 HV while Ni-20Cr coatings have indicated lower hardness values of 400 HV. The authors have mentioned that near the interface the microhardness of the coated substrate is higher than the substrate itself due to a work hardening during substrate preparation treatment and under the impact of HVOF molten particles.

Otsubo, et al. [12] investigated the structure of the interface between a nickel based coating and mild steel substrate. They concluded that Lumpy $Fe_2B$ boride precipitates can be formed in the substrate at the interface between the coating and the steel substrate after heating at 1273 K for 1.8 ks or more. The formation of this type of borides doesn't affect the increase of adhesion due to interdiffusion.

Simunovic, et al. [13] studied the effect of flame spraying and fusing on the microstructure of substrates made from heat treated carbon steel C45, a heat treated low alloyed 42CrMo4

steel and austenitic stainless steel X6CrNiMo18-10-2. They confirmed that the fusing activated the transformation of martensitic to perlite in the affected zone of C45 steel. They also concluded that the high fusing temperature has a significant influence on the coating–substrate interface and it does not significantly affect the microstructure of hardened and tempered 42CrMo4 steel. They marked two interface zones for flame-sprayed and fused Ni-based self-fluxing alloy coatings: diffusion zone of 550 HV0,1 and dendritic zone of low hardness (400 HV0,1). They also showed that in the case of steel the increase of the alloying elements decrease the size of the diffusion zone. Along with the high alloying element content, the lower thermal conductivity of the stainless steel makes the diffusion zone thinner than that observed in the case C45 and low alloyed 42CrMo4 steels. Fusing the coatings at temperature exceeding that of heat treatment of stainless steel (around 1000°C), makes the microstructure of Austenitic grains coarser remote from the coating.

Skulev, et al. [14] examined the microstructure of nickel-base plasma sprayed coatings. They found the coatings deposited on steel substrate are composed of $\gamma$-Ni solid solution and amorphous phases. Contrary to those, the coatings deposited in cast iron reveal a microstructure that contain further nickel borides $Ni_3B$, chromium borides CrB, and chromium carbides $Cr_{23}C_6$. They found also that the heat treatment at temperature up to 1200 gives high hardness to the coatings deposited on steel substrate.

La Barbera-Sosa, et al. [15] studied the effect of spraying distance (380, 425, and 470 mm) on the microstructure and mechanical properties of a Colmonoy 88 alloy deposited by HVOF thermal spraying. The study indicated that there were an increase on the volume fraction of the unmelted particle and a generation of interlamellar microcracks with the increase of the spraying distance, which induce a decreasing in the elastic modulus of the coatings. The anisotropic behavior of the hardness and the elastic modulus makes them high on the cross section of coating than the deposition plane.

Zeng, et al. [16, 17] investigated the effects of the addition of silicon and boron on the oxidation behavior of Fe, Ni20Cr and NiCrSiBC during air plasma spraying. They reported that Addition of these elements is more effective for reducing the in-flight oxidation as compared to the on-substrate oxidation. They found also that the preferential oxidation of C, Si, and B and the formation of their gaseous oxides prevent the oxides from picking up

in NiCrSiBC coatings. They concluded that the oxygen content in Ni20Cr coating is higher than that of NiCrSiBC coating by a factor of 13 when the sprayed distance is fixed at 100 mm. these authors also mentioned in another investigation that in the case of Ni20Cr, the formation of $Cr_2O_3$ and its vaporization particles occurred during the plasma jet and dominate the oxidation in the deposits.

## II.3 Porosity and mechanical properties of nickel selffluxing coatings

In the thermal spray coating, pores occupy the space between the deposited splats and they can be formed beside unmelted particles. We distinguish two types of pores: interlamellar pore and globular pores. Thermally sprayed coatings usually contain a certain number of voids and porosity especially when the used spraying velocities are small which make the density of the deposits lower.

Zhang, et al. [18] reported that the increase in porosity decreases the microhardness and the Young's modulus of coatings and with the increase in microhardness the Young's modulus of coating increases. The amount of porosity in the coating generally increases with the decrease of the hydrogen gas flow rate and the spraying power or the increase of the powder feed rate.

Zhang, et al. [19] found that the variations of porosity, elastic moduli and micro-hardness of the supersonic plasma-sprayed Ni–Cr–B–Si–C coatings followed a Weibull distribution; they concluded that with the increase of the powder feed rate the microhardness and the elastic modulus decreased and then increased after reaching a local minima. They established that the elastic modulus depended on to the square root of the microhardness and the residual stresses were mainly controlled by the elastic modulus of coatings. Moreover, the residual stresses followed the variation of the elastic modulus; it decreased to reach a local minima and then increased with the increase of the powder feed rate. The higher powder feed rate promotes the existence of unmelted particles inside the coatings whereas the lower powder feed rate engender the formation of microcracks and pores, which affect the microhardness and elastic modulus values.

Zhang, et al. [20] found that the amount of porosity of Ni-based coatings increases with decreasing the hydrogen gas flow rate.

Zhang, et al. [21] concludes that if the spraying power is low , microcracks, pores, and unmelted particles can be formed inside the Ni-base coatings due to the weak bonding between lamellar structures, residual stress relaxation, and incomplete filling of the rapidly solidifying. They found also that the porosity content increases with the decrease in the spraying power and that 57 kW is sufficient to fully melt the feedstock powder and to not detect any variation in the amount of porosity with the increase in the spraying power.

## II.4 Adhesive strength of nickel selffluxings coatings

The main purpose of applying the nickel selffluxing coatings is to protect the substrates' surfaces from corrosion and wear. However, premature damage of the substrate/ coating system can occur if cracks are present inside the coatings or if the adherence of coatings to the substrate is inappropriate. For these reasons, a number of authors have investigated the cracking resistance, the fatigue and the bond strength of nickel selffluxing coatings.

Li and Wang [22] assessed the effect of particle state on the adhesive strength of HVOF sprayed NiCrBSi and Ni-Cr coatings according to the (ASTM) C633-79. They inferred that the complete melting of spray droplets doesn't contribute to the increase of HVOF adhesive strength and the deposition of a partially melted large particle result in a substantial improvement of adhesive strength of the HVOF coating. The adhesive strength of NiCrBSi and Ni-Cr coatings deposited with the powder of particle size 45-74 µm reached about 40 MPa. The coatings deposited with large nickel-based alloy powders from 75-104 µm particle are composed of partially melted particles and have an adhesive strength of more than 76 MPa. They also found that the large droplet in the partially melted state is more effective to the improvement of the adhesion of HVOF metallic coating compared with the small droplet, which is also in the partially melted state.

Wang et al. [23] found that the state parameters of a spray particle, i.e., temperature, velocity and momentum, cannot be directly linked to the bond strength of HVOF coatings. The bond strength of HVOF coating can only be correlated well with the effective mass of solid phase in a spray particle (figure.1).

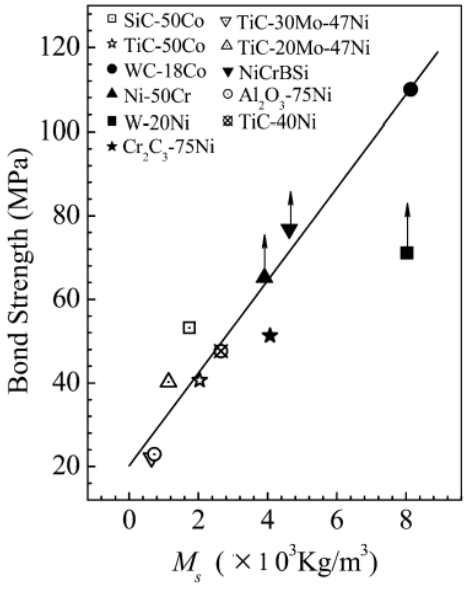


**Figure II.1- Influence of effective mass of solid phase on the bond strength of HVOF coatings.**

Wang et al. [24] inferred that the mechanical interlocking is the mechanism that governs the adhesion in the case of the melted spray particles and the deposition with semimolten particles induces the formation of the physical bonding in addition to the mechanical bonding. They found that the increase in the roughness of the substrate surface implies an increase in the adhesive strength of the coating and the effective adhesion occur when surface roughness became larger than Ra 1.7 Am (figure 2.). The coating attenuates a limited adhesive strength around 40 MPa with rough surfaces.

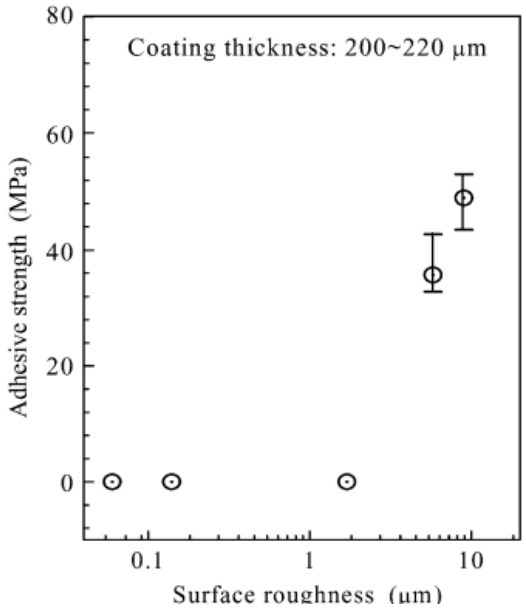


**Figure II.2- Effect of the surface roughness on the adhesive strength of HVOF NiCrBSi coating.**

Dolgov [25] studied the influence of the plasma coating thickness on the variation of elastic modulus. They established that the increase in the coating thickness leads to a decrease in the elastic modulus.

## II.5 Residual stresses

Residual stresses can have a strong influence of the coating properties. Their relaxation can cause the formation and the development of cracks inside the coating if the residual stresses are higher than the coating strength. Residual stresses can be generated due to :

- A molten particle cooling during the phase of deposition.
- A phase transformation that occurs inside the coatings.
- A plastic deformation of the coatings
- A thermal expansion coefficient mismatch between the substrate and the coating during the cooling

However, the residual stresses which result from the contraction and the cooling of particles are frequently mentioned in the literature. These residual stresses can cause delamination of coatings during their cooling from the deposition temperature or under the influence of external loadings. During the deposition the flattening and the cooling of

particles take a short time that allow the generation of tensile or quenching residual stresses .The deposition technology and the microstructure of the coatings are the prime factors which determine the type and the degree of these residual stresses. Molten particle contraction during the cooling generates high residual stresses that are higher than the yield strength. However, as the relaxation of the residual stresses occur, the level of maximum stresses is lessened in the cooled flattened particles. Both the creep and yield are the prominent mechanisms that govern the residual stresses relaxation in the case of metallic coatings. The relaxation of the residual stresses for ceramic coatings can happen through the formation of micro-cracks. The other type of residual stresses can be tensile or compressive. They result due to a thermal expansion mismatch between the substrate and the coating. If the thermal expansion of the coating material is greater than that of the substrate material, residual stresses of tensile type can develop inside the coating. The degree of these residual stresses can be affected by the temperature, Young's modulus of both the coating and the substrate and also by their thermal expansion coefficient.

Tsui and Clyne developed a simple analytical model which allow the prediction of the distribution of the residual in the thermally sprayed coatings. The model is adopted by many authors and is based on force and moment balances and takes as inputs the specimen dimensions, material properties and the intrinsic stress for planar geometry. Tsui and Clyne proposed another analytical model for cylindrical geometry. This model is based on Lamé equation and takes into account the two main residual stress generation mechanisms: deposition stress and differential thermal contraction [26, 27].

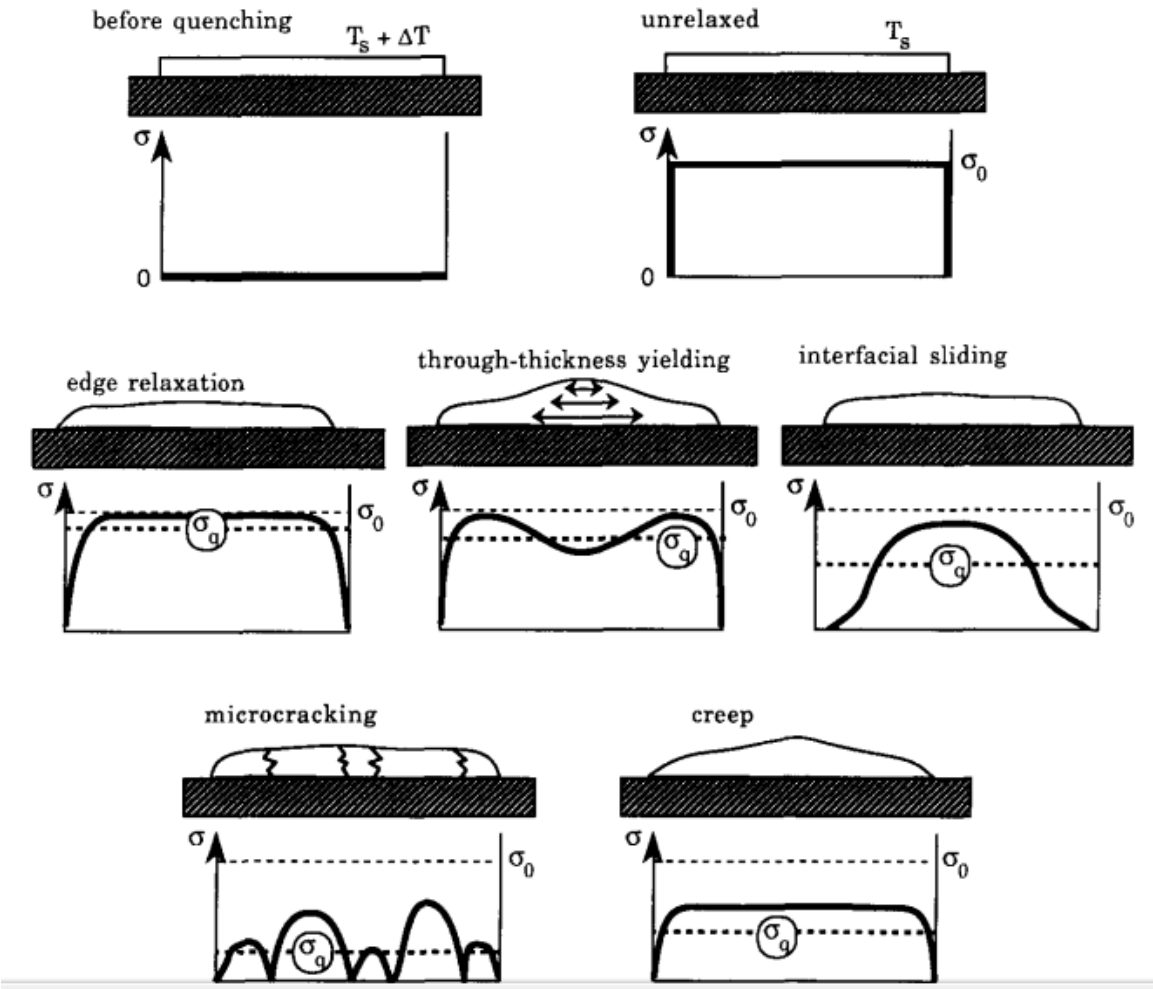


**Figure II.3 - Schematic illustration of the stress distributions within a single splat before and after various stress relaxation phenomena have taken place.**

## II.6 Sliding wear of nickel seffluxing coatings

Zhang, et al. [28] showed that the addition of mixture of $La_2O_3$ refine the microstructure, rises the hardness , increases the dry sliding wear resistance of flame-sprayed and flame-fused nickel based coatings and results in lower friction coefficient. They also established that the wear rate increases with the increase of applied load and that the friction coefficients are related to the sliding speed through a nearly linear relationship.

Chen, et al. [29] demonstrated that the addition of 30% of conventional and nanostructured WC–Co to nickel-based self-fluxing alloys resulted in a significant increase in wear resistance and exhibit lower wear loss. They established also that the addition of ceria refine the microstructure of the deposits but had no effect on their wear behavior.

Chen, et al. [30] proved that under lower load, only the elemental diffusion occur in the worn zone. However, at high loads the precipitation of new phases (WC and $WC_{1-x}$) has been detected due to the action of frictional force and heating. The new phases which have in size ten to hundred nanometers increase the hardness of the coatings and their amount can be increased by increasing the WC content on the coating.

Garcia, et al. [31] proved the partial laser remelting applied on NiCrBSi plasma spray coatings can improve the wear behavior and increase the hardness of the deposits. They found that a minimum wear loss was recorded when 46% of the surface was remelted. They found also that the laser remelting reduce the amount of porosity inside the plasma sprayed coatings, which lead to a poor lubrification conditions and that contribute to the increase of wear. However, the authors observed that the non-homogeneous plasma spray structure of the melted surface below 46% induce a greater wear rates and don't improve the lubrification conditions as the measured coefficients of friction for 16% to 56 % are the same. The study also demonstrated that the laser track angle can affect the final coefficients of friction but not the wear behavior of the coatings. The run up was found to be the prime phenomenon which has been occur in the first 30,000 cycles of the wear test. The use of short sliding distance can minimize the run-up phenomenon.

Serres, et al [32] examined the microstructures and the mechanical properties of NiCrBSi and NiCrBSi-WC composite coatings manufactured via Hybrid Plasma/Laser Process. They found that this particular process promotes the formation of dendritic structure that doesn't contain voids and porosity. Moreover, they confirmed that the process is responsible for the decarburization of the coating layers and the non-detection of any cracks. They found also that the hardness of the coating increase linearly with the increase of WC content and the Young modulus evolves when the WC content is 25% or 50%, in relation to the CrWB-type boride distribution in the matrix. The increase of hardness and Young modulus contribute to the decrease of the wear rates.

Guilemany, et al. (Guilemany, J. M., et al.2004) mentioned that $WO_3$ oxide acts as a solid lubricant and reduces wear in HVOF-deposited coatings.

A number of authors [33-36] outlined that the development of oxide layer ( like $Fe_3O_4$ and $CrO_3$ ) on the surface of coating at elevated temperature during the wear test may increase

the wear resistance and decrease the friction coefficient because the oxide layer act as protective film against the metal-metal contact.

Hejwowski [35] showed that Ni–Co alloys with Ni content between 40.4 and 64.3 have a wear resistance 2 times higher than plasma-deposited cobalt alloy, which make it a good candidate for hardfacing applications.

Zhang, et al. [36] showed that in the case of Ni–Cr–B–Si–RE coatings the increase in load is accompanied with an increase in the wear rates. Inversely, the increase in sliding speed between 0.02 and 0.08 m/s induces a decreasing in the wear rate then an increasing of the wear rate when the sliding speed reach 0.1 m/s. Moreover, the average friction coefficient which is about 0.48 increases with sliding speed.

Gonzalez, et al. and Fernandez, et al. [37-39] proved that even at moderate temperature and at low sliding speeds an oxide layer can be form on the coating surfaces to prevent the metal-metal contact during the wear tests. However, comparatively to the previously mentioned inferences, unmeleted particles and oxides can peel off from the coating top surface (but for shorter stand-off plasma spray distances) to act as abrasive particles during sliding and these contribute to the increase of wear rate at elevated temperature [34].

Serres, et al. [40] claimed that the destruction of the oxide layer during sliding can cause a two body or three body abrasion wear. The wear debris at elevated temperature can result in three body abrasion.

Contrary to what was claimed by Serres, et al.[32], several authors established that the addition of WC carbides had no effect on sliding wear. In fact, Wong, et al.[41] mentioned that the WC carbides remain in its unmelted form within the coatings and can easily peel off during the sliding test. Martin, et al. [42]; Rodriguez and et al.[43] demonstrate that the addition of WC (35%) had an effect on the wear of the counterbody material in sliding contact and cannot have an influence on the increasing of sliding resistance of plasma-sprayed Ni-based self-fluxing alloy coatings. The WC content influence the distance between the tested sample and the conterbody material and can be a factor for the wear resistance. For this reason, several authors have searched for the optimal WC content that can have an influential effect on the wear resistance.

Sari and Yilmaz [44] found that the WC content in the coating powders can substantially affect the wear resistance. The optimum weight proportion of WC was found to be around 55 wt.% in order to obtain the best wear resistance.

Kim, et al. [45] claim that the optimum WC cannot be the same for all types of wear. They showed that the coating of 35% WC with NiCrBSiC exhibits the highest hardness and the lowest porosity. Nevertheless, the addition of 25% WC to NiCrBSiC alloy result in a better wear resistance for Sugaru abrasive wear test, while 40% WC addition showed the best wear resistance for abrasive wear test (dry sand rubber wheel).

Van Acker, et al [46] claim that the size and the content of $WC/W_2C$ carbide cannot have an influence on the increasing of wear resistance because it depends on the wear mode.

Xu, et al. [47] confirmed that in the case of laser clad coating the sliding wear resistance strongly depends on WC content. It increases if the WC doesn't exceed 40% and it decreases otherwise due to the poorer connections between the WC and Ni matrix.

Wang, et al. [48] showed that up to 50% of TiC addition the wear rate of TiC + NiCrBSi + rare earth ($La_2O_3$) composite coatings decreases but it increase when the TiC content is higher than 50%. The authors also demonstrated that the addition of $La_2O_3$ to the composite result in a reduced friction coefficient and increased microhardness as well as a better wear resistance.

Niranatlumpong and Koiprasert [49] proved that the addition of a right amount of molybdenum Mo can improve the friction properties and increase the resistance of thermally sprayed NiCrBSi coatings against wear.

Buytoz, et al. [50] showed that the addition of SiC also influence the friction coefficient and the wear rate of NiCrBSi coatings. They revealed that the presence of SiC can affect the composition, the microstructure, and the hardness of the HVOF-sprayed composite coatings.

Fernandes, et al. [51] proved that the wear resistance and hardness of Colmonoy 88 coatings can increase with the addition of nanostructured zirconia, while their friction

coefficient decreases. Coatings produced with mechanical alloying show the highest sliding wear resistance.

Sun, et al. [52] proved that the wear weight loss in vacuum (47.9%) is greater than that in atmosphere (11.4%). The examination of the worn surfaces showed that the abrasion is the mechanism that govern wear loss of the coatings in atmosphere, while adhesive and ploughed wear are the dominant wear mechanisms in vacuum.

Gomez del-Rio, et al. [53] analyzed the effect of the processing conditions on the microstructure, the hardness and the wear loss of NiCrBSi coatings. They inferred that the microstructure, the hardness, and the toughness as well as Young's modulus affect the sliding wear of coatings and that the wear loss can be correlated to the ratios H/E and $H^2/E$.

Niranatlumpong and Koiprasert [54] concluded that in the case of NiBSi-WC/W2C arc sprayed coatings the absence of Cr induces a hardness decreasing. The wear resistance is higher than that of NiCrBSi–WC coatings due to the good metallurgic bounding between the matrix and the tungsten carbides. The poor connection between the NiCrBSi matrix and the tungsten carbides leads to the detachment of these carbides which results in a higher wear loss.

Chen, et al. [30] claimed that the precipitation caused by high friction load and heating and the strengthening that is due to deformation can result together in a hardness increasing during sliding.

## II.7 Corrosion of nickel selffluxing alloys

Guilemany, et al. [55] studied the corrosion behavior of HVOF coatings. They demonstrated that the coatings are prone to a localized corrosion especially on the cobalt matrix.

Bolelli, et al. [56] concluded that the HVOF nickel based self-fluxing coatings with WC-12Co are subject to selective corrosion near WC-Co particle.

Man, et al. [57] mentioned that various phases can play the role of galvanic cell affecting the selective corrosion of coatings.

Flores, et al. [58] suggested the use of cobalt or nickel coated WC particles allows to avoid their degradation caused by the dissolution of tungsten carbides and impede the formation of secondary phases due to the presence of carbon.

Gil and Staia [59] claim that the micropitting that affect the corrosion behavior of NiWCrBSi coatings can be due to nickel matrix corrosion which leads to the degradation of hard phases via galvanic corrosion or due to a degradation of splats as a consequence of crevasse corrosion developed through the splat boundaries.

Serres, et al. [60] mentioned that the various defects present in coatings without remelting can engender the degradation of the substrate through galvanic or crevasse corrosion. As many author did [61-64], they recommend remelting the coatings so as to obtain a dendritic microstructure instead of lamellar to improve the corrosion behavior of coatings.

Shrestha, et al. [61] concluded that the splat boundaries are the preferable sites for the development of crevasse corrosion, however, after posttreatment they deduced that the micropitting is the main degradation mechanism.

Suutala, et al. [65] concluded that the laser remelting can improve corrosion behavior of nickel based selffluxing coatings but a wise selection of the type of laser and the processing parameters should be done to avoid the formation of cracks within the coatings.

Liu, et al. [66] claimed that the presence of microcracks inside the coatings can be a cause for the electrolyte penetration to the substrate. They also mentioned that the corrosion potential of nickel based coating is higher than that of the stainless steel due to the effect of Cr passive film.

Zhao, et al. [67] claimed that inclusions and porosity influence the corrosion processes in different way. Inclusions promote the presence of micro cells on the surface of coatings which decease the corrosion resistance of the alloy. The presence of porosities can decrease the cohesive strength leading to particles drop off from the coating surface under the influence of the electrolyte.

Zhao, et al. [64] proved that the partially melted and unmelted particles constitute favorable sites for the initiations of corrosion in nickel based coatings.

Bolelli, et al. [56] claimed that the presence of unmelted particles reduces chromium in the nickel matrix and that the selective corrosion can occurs in the matrix between carbides and borides as galvanic cells.

Sharma and Majumdar [68] demonstrated that the presence of a larger amount of chromium and silicon in the coating can improve the resistance of the coating against corrosion and pitting.

Man, et al. [57] mentioned that the corrosion resistance improvement is ascribed to the presence of nickel in the coatings and is also due to the nickel and aluminum and to the chromium and nickel solution. They reported that the critical potential for pit formation for the coating is the same as that of Al6061 alloy.

Tam, et al. [69] reported that the presences chromium phases as precipitates can have a harmful effect on the corrosion resistance. They found also that the increase of hardness is accompanied with an increase of cavitation erosion resistance.

Serres, et al. [70] concluded that the nickel and chromium can improve corrosion resistance as same as the reduced porosity and the larger coating thickness do. They mentioned that NiCrBSi coatings can be successfully used as alternatives to the hard chromium electrolytic coatings for ecologic aims and for the reason that the NiCrBSi are more inexpensive than the tungsten chromium carbides in a metallic matrix or the cobalt based alloys.

Serres, et al.[40] assessed the influence of salt fog aging on wear and corrosion behavior of NiCrBSi which was laser cladded onto steel substrate. They found that the larger the exposure aging time result in a pitting corrosion. They confirmed also that the corrosion of substrate occur as the electrolyte reached the substrate surface through pitting.

Kesavan and Kamaraj [71] reported that the lower chromium content in the matrix can result in a decreased corrosion resistance due to the formation of chromium carbides.

Comparatively to gray cast iron, Fe-30Mo-2C, Zn-SiC, Stellite, Stanford and Jain [72] showed that the flame-sprayed nickel-based self-fluxing coating exhibit the highest sliding wear rate. They found also that the resistance against corrosion of HVOF-sprayed Stellite is the best in salt environment.

Sidhu, et al. [73-75] demonstrated that the resistance against corrosion of the HVOF-sprayed Stellite decreased in molten salt $Na_2SO_4$ -60% $V_2O_5$. However, Sidhu, et al. reported that in real working environment (coal-fired boiler), Stellite coatings resisted corrosion more than the HVOF Ni-based self-fluxing coating because the Cr passive layer was more compact.

Oliveira, et al. [76] reported that during the fatigue corrosion test the cracks were initiated at alumina particles deposited on the substrate surface during the grit blasting treatment.

Hot corrosion resistance of HVOF sprayed nickel based coatings in molten salt is due to the formation of oxides of chromium, silicon, and nickel and spinels of nickel and chromium, which impede corrosion by filling defects and pores as well as splat boundaries. Accordingly, Sidhu, et al. [73, 77-79] confirmed that the formation of passive film has protected the HVOF coating from a mass loss in $Na_2SO_4$-60% $V_2O_5$ at 900 °C. However, a mass loss was recorded at 800 °C when $Na_2SO_4$-25% NaCl was used as electrolyte and this was due to the non-formation of a protective layer [80].

# Chapter III :

# Materials and Methods

In this chapter, we describe the approaches and the experimental methods used to carry out our work. It is subdivided into 3 main parts:

The first and second are devoted to metallographic and mechanical characterization. Their purpose is to define the chemical composition and the mechanical characteristics of the steel and the coating materials studied before and after flame spraying.

The second is intended for both the profilometry analysis and the electrochemical study of the coatings in chlorinated (NaCl) and sulfur ($Na_2SO_4$) containing medium by potentiodynamic polarization, and electrochemical impedance spectroscopy.

## III.1 Metallographic characterization

### III.1.1 Presentation of the studied materials

To carry out this study, we have used X18 carbon steel as substrates and MB40 powder as coating material for performing the bonding layer. We have also used two NiFeCrBSi-WC composite wires to realize the deposits. The first one is commercially designated as Spherotene wire. The two wires contain WC particles that are embedded in NiFeCrBSi powder. The steel substrates have 50 mm in diameter and 5mm in thickness. They were cut from rods which have 60 mm in diameter.

### III.1.2. Spraying conditions

#### III.1.2.1 Preparation of the substrates' surfaces

Before the thermal spraying, the steel substrates were cleaned from any oxide, oil, grease, impurity or other material deposited thereon with a chemical solvent so as to avoid the formation of defects during the solidification of the molten droplets.

#### III.1.2.2 Operating conditions of flame spraying

The realization of coatings was performed in the open atmosphere using the acetylene as fuel. The selected processing parameters for both the bond layer deposition and the flame spraying are listed in Table III.1.

**Table III.1 –** Flame spraying processing parameters.

| Acetylene pressure | Oxygen pressure | Spray distance | Torch velocity |
|---|---|---|---|
| 0.2 bars | 4 bars | 120 mm | 1 mm/s |

### III.1.2.3 Hard-facing with flame spraying

Hard-facing consists of making deposits on degraded or worn functional surfaces to restore their dimensions and reconstitute their profiles. In order to do so, alloys of similar or higher performance characteristics compared to the base metals are often used.

In contrast to welding, hardfacing is an operation that consists of depositing hard-surface layers on the functional surfaces of components or mechanical parts. The aim is to modify the surface properties and thereby enhance their performance against different forms of wear: friction or metal-to-metal wear, abrasion, impacts, erosion, cavitation, corrosion wear, etc. Nevertheless, it should be noted that the wear is often caused by several deterioration mechanisms acting concurrently, such as abrasion, erosion-cavitation, etc.

The filler materials used for build up and hardfacing are typically more highly alloyed or of a different chemical composition than the base metals. These filler materials include cobalt alloys (Stellite®), nickel-based alloys, tungsten carbides, etc. Choosing an adequate filler material for a given application depends on several factors, including the type of base metal, the type of wear, the working environment (heat or corrosion), the cost, etc. Hardfacing significantly prolongs the life of the wear parts and optimizes the cost of repairs and maintenance. In our case, the flame spraying was used as hardfacing process. The coating operation of samples for their protection against wear was carried out with an oxyacetylene torch, type TECHNOKIT T2000 (Figure1). This type of coating is simple and economical and preserves the integrity and the integrality of the tungsten carbides.


**Figure III.1- TECHNOKIT T2000 torch.**

### III.1.3 Cutting of samples

Sampling of samples for chemical analysis, and optical metallography are performed by cutting. The samples are degreased with acetone and then rinsed with water.

### III.1.4 Characterization of the chemical composition

For the determination of the chemical composition of the coatings, we carried out a chemical analysis by X ray fluorescence spectroscopy at the CRAPC Center (Centre de Recherche Scientifique et Technique en Analyses Physico – Chimique) using ZSX PrimusIV spectrometer. Indeed, X-ray fluorescence is a spectral analysis method that is commonly used to determine the chemical composition of a sample. The technique is based on the fluorescence of atoms in the X-ray domain. The excitation of the sample atoms from the X ray source is generally insured by an X-ray beam. The analysis of the captured spectrum provides qualitative or quantitative information about the elemental composition of the sample.

When the sample exposed to high-energy rays of short wavelengths, the electronic structure of the sample receives that energy and become excited. As a result, the excited electrons leave their orbit to an orbit of higher energy. Thus, the electronic structure of the material becomes unstable. The excited electrons have a tendency to return to its internal orbits by emitting energy in the form of light (fluorescence). This fluorescence or characteristic radiation refers to a specific element from which the analyzed sample is composed.

This technique is universal and nondestructive. With it, most of materials can be analyzed without prior preparation. It doesn’t consume time

Figure 2 shows the schematic representation of the simplest apparatus which comprises two essential elements: the exciter primary radiation production system and the analysis and detection system.

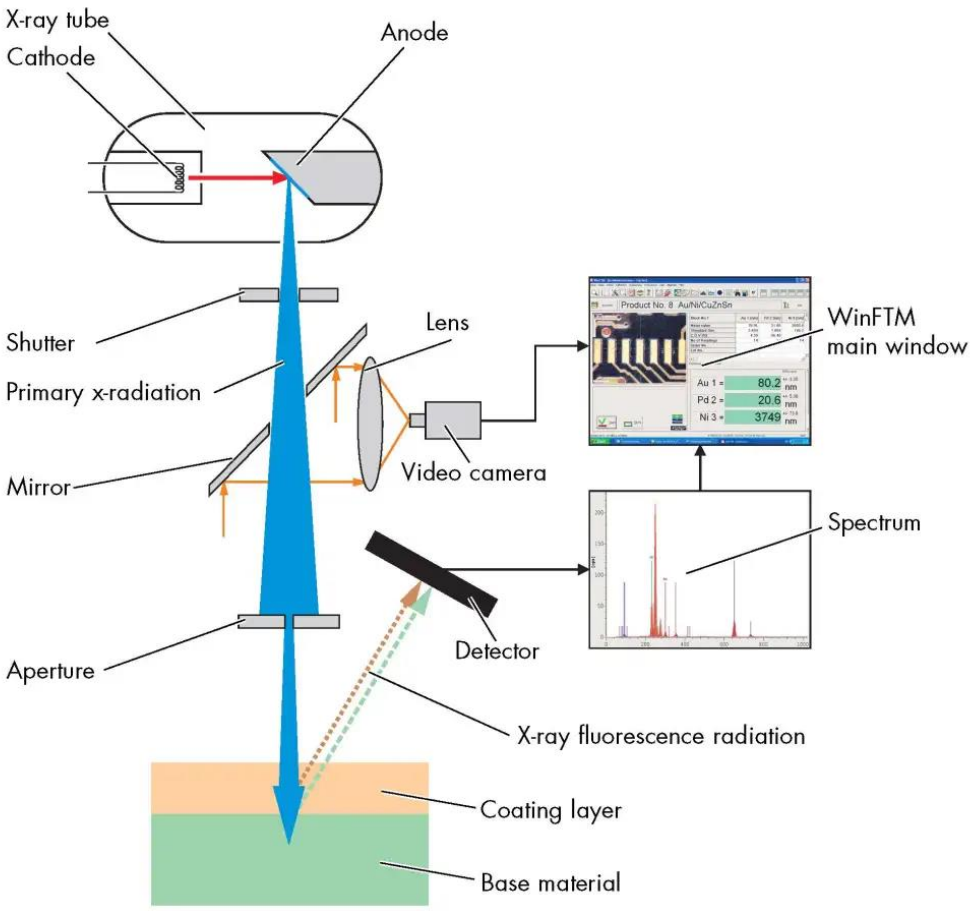


**Figure III.2- Schematic of an X-ray fluorescence analyzer.**

The analysis of the chemical composition of the coatings with X-ray fluorescence made it possible to obtain the mass percentages of the different alloying elements. These quantities are given in Table III.2 and Table III.3.

**Table III.2 -** Chemical composition of the first coating (Coating A).

| Ni | Fe | W | Cr | C | Si | Mn | B |
|---|---|---|---|---|---|---|---|
| 68.3 | 12.4 | 8.71 | 4.5 | 4.11 | 1.85 | 0.175 | < 1 |

**Table III.3 -** Chemical composition of the second coating (Coating B)

| Ni | Fe | W | Cr | C | Si | B |
|---|---|---|---|---|---|---|
| 78.48 | 2.96 | 4.19 | 6.20 | 5.71 | 2.72 | < 1 |

The chemical composition of the feedstock powder (MB40) that has been used to perform the bonding layer was determined by EDX spectroscopy analysis using an accelerating voltage of 25 KV. The results of this analysis are tabulated in Table III.4.

**Table III.4 -** The chemical composition of the powder used to perform the bonding layer.

| Ni | Mn | Cr | Si | Fe |
|---|---|---|---|---|
| 72.46 | 10.79 | 08.34 | 04.95 | 03.46 |
| 72.87 | 10.47 | 08.53 | 05.01 | 03.12 |

The micrograph showing the morphology of this powder (Figure 3.(a)) was obtained by the mean of a scanning electron microscope. The associated dispersive energy spectra are shown in Figure 3.(b).

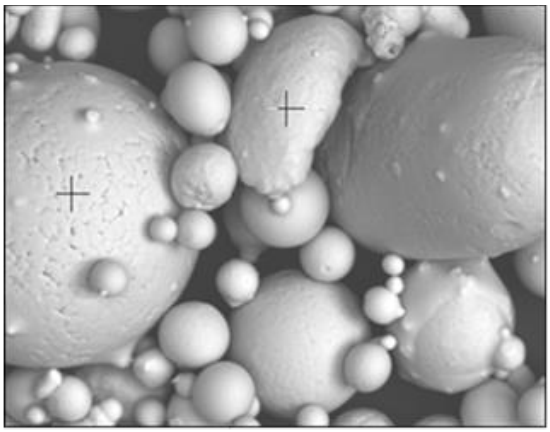

**(a)**

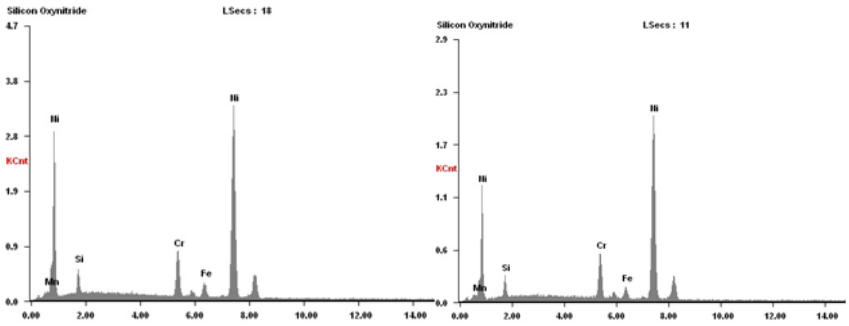


**(b)**

**Figure III.3 - Micrograph showing (a) the morphology of the sprayed powder used to perform the bonding layer and the selected EDX analysis spots; (b) Dispersive energy spectrum associated with each analysis.**

### III.1.5 Sample preparation

After sampling, the samples are cold-coated in an epoxy resin. A first mechanical polishing has maintained the flatness and eliminated the s mechanical deformation caused by cutting. A series of SiC silicon carbide abrasive papers of decreasing grain size (P240, P400, P600, P800, P1000, P1200) fixed on the turntable of the touring polisher was used at a speed of 300 rpm.

The finishing step is performed on a felt paper impregnated with a dilute suspension of colloidal alumina of size equal to 0.3 microns.

### III.1.6 Chemical etching

A chemical etching in aqueous solution of Murakami reagent (10g $K_3Fe(CN)_6$ + 10g KOH/NaOH + 100 ml water) was performed at room temperature for a period of 180 seconds to reveal the coating microstructure. This chemical reaction reveals the nickel grains in dark gray, the nickel dendrites in light gray and the pores in black. The experimental setup is shown in the figure below.

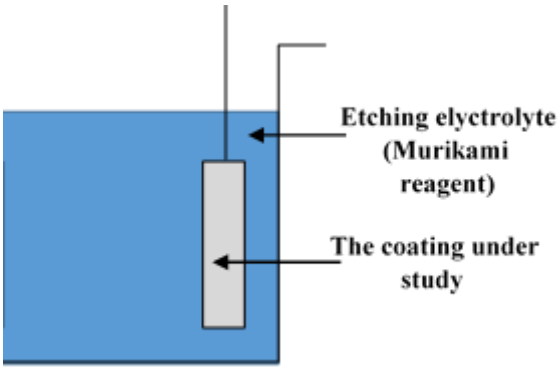


**Figure III.4 - Illustrative schema of the chemical etching device.**

### III.1.7 Electron microscopy and image acquisition

The micrographic analysis was carried out at the university of Rome using a Tescan Mira 3 electron microscope . The scanning electron microscope (SEM) is an electronic apparatus with which the microstructure of materials can be observed with high space resolution. It gives details about the microscopic state of the surface of a sample when an electronic beam from SEM source interferes with it (Figure 5). The resolution can be up of 0.4 nanometers and the magnification ranges from 3 to 10 times to $10^6$. The electronic interaction with the atoms of the sample surface produce various signals about its topography and its chemical composition. These information are collected with special detectors during the scanning. The surface topography is created from the

signals that come from a secondary electron detector, while, the chemical composition can be determined by the EDS (*Energy Dispersive Spectroscopy*) through an X-ray detector. The collection of backscattered electron allow to construct metallographic images in which the present phases are distinguishable according to their contrast. The image processing using the ImageJ software allows the estimation of the ratio of the different phases by varying the contrast created by the difference in the reflectivity of the different phases in presence.

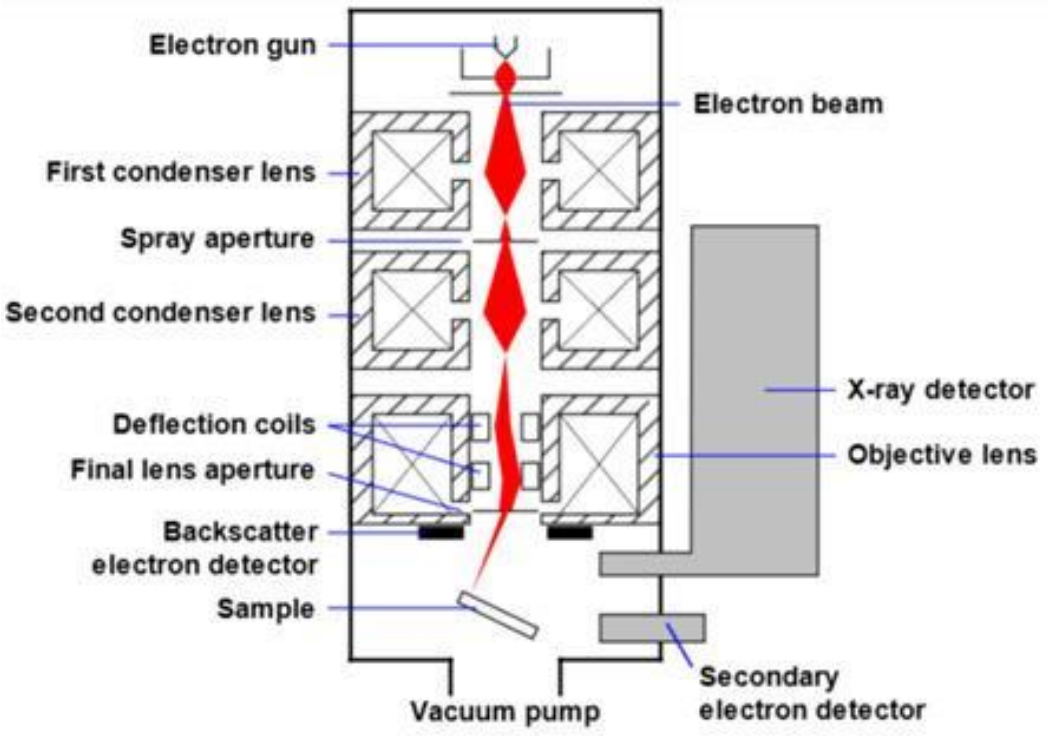


**Figure III.5- Schematic showing the components which constitute the scanning electron microscope.**

### III.1.8 X-ray diffraction

X-ray diffraction was performed at CRAPC center using D8 Advance Eco Brucker diffractometer, The X-ray diffraction (Figure 6) is generally used as a nondistructive technique to determine whether the material is crystalline or amorphous. X-ray source is Cu Kα radiation (λ = 1.5406 Å). The crystal lattice consists of parallel and equidistant lattice planes. Depending on their orientation, the incident X-ray beam can be reflected if a constructive interference is produced. Each XRD pic results from a monochromatic X-rays scattered at specific angles from each set of

lattice planes in a sample. The analysis and the identification of the atomic structure of microstructural phase can be done through Brag Brentano method:

$$2dsin\theta = n\,\lambda \text{ (Bragg law)}$$

where d is the reticular distance (the distance between the lattice planes), λ is the wavelength and n is the order of reflection. This relation shows that it is enough to measure the Bragg angles (θ) to determine the dimensions of crystallites. The amplitudes of the reflected waves make it possible to determine the atomic structure of the pattern.

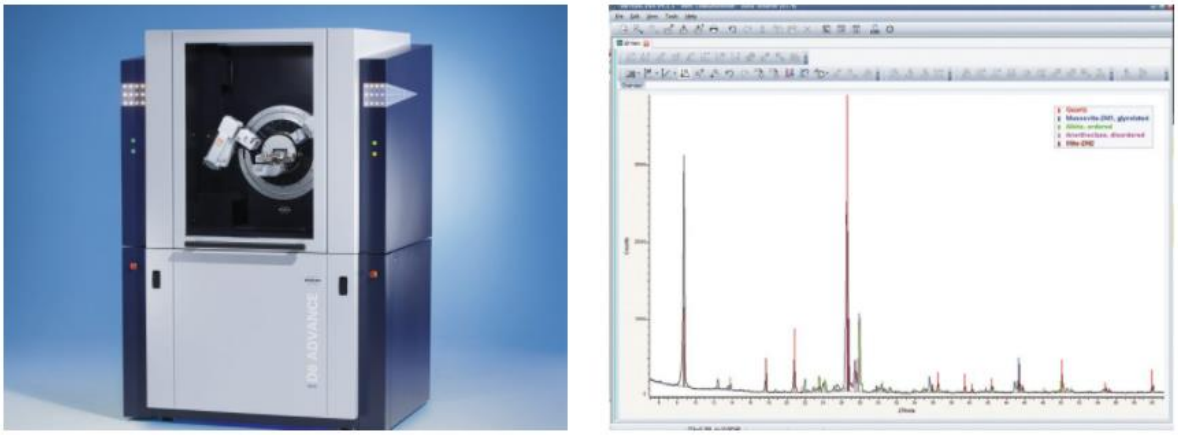

**Figure III.6- X-ray diffraction machine with an Xray diagram.**

## III.2 Mechanical characterization

Micrographic examinations after spraying are supplemented by hardness , micro-hardness, and nano-indentation tests. The micro-hardness tests are done at the Metallurgy Laboratory (LSGM) at the National Polytechnic School of Algiers while the hardness measurements were performed at the University of Rome. The nano-indentation tests were performed in the Center for the Development of Advanced Technologies (CDTA).

### III.2.1 Hardness Tests

For the Vickers hardness tests, the principle of functioning is defined in the figure below. we have used as indenter a wedged diamond of pyramidal shape with a square base and angle 136 ° between two opposite faces (Figure 7).

A force F of 100gf and 200 gf is smoothly applied up to its maximum value in 15 s. It is then removed. The pyramid then leaves a pyramidal shape. The measurement of Vickers hardness is given by:

$$H_V = 7{,}416 \times \frac{F}{(d_1 + d_2)^2}$$

$d_1$ and $d_2$ are the measured diagonals of the impression.

For the microhardness test, a Mytutoyo microdurometer HM100 model was used.

### III.2.2 Micro-hardness Tests

A filiation of micro-hardness measurements was carried out on the transversal cross-section of a sample, under a constant charge of 0.1Kgf, starting from the substrate to the top sprayed coating surface while passing through the bonding layer. A step of 50 µm has been applied.

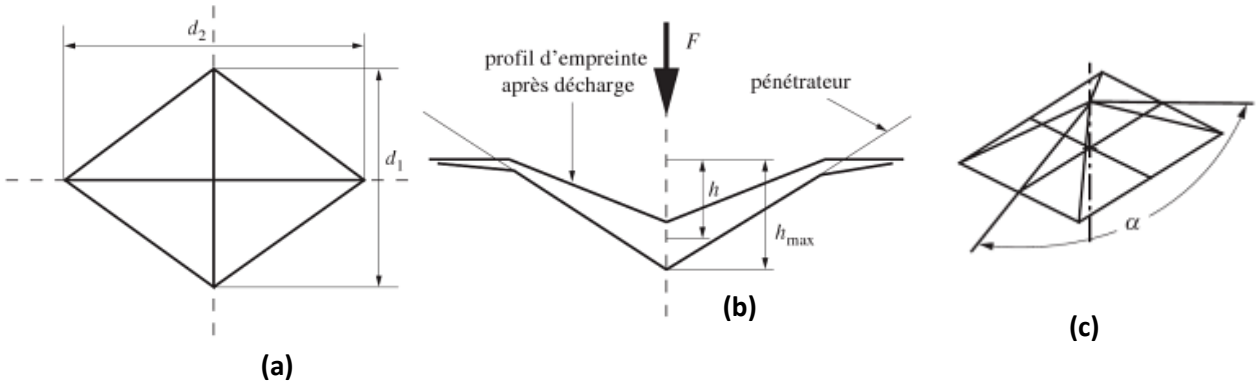


-

**Figure III.7 - Condition of the HV hardness test, (a) Schematic diagram of a Vickers hardness test, (b) Schematic of a Vickers indentation imprint, (c) Vickers pyramid with a square base of α = 136 °.**

### III.2.3 Nano-indentation Tests

. Nanoindentation (also known as instrumented penetration test) is a method of material testing that is used to determine the hardness of materials on small length scales (nanometers, nm). The technique has its origin in the Mohs scale for hardness, where the materials are classified according to what they can scratch and, in turn, according to which other material can be scratched. The characterization of solids in this way is essentially carried out on a discrete scale, so many efforts have been spent in order to develop techniques for the evaluation of the hardness of the material according to a field of continuous variability. Therefore, the hardness tests of Meyer, Knoop, Brinell, Rockwell and Vickers were adopted.

Nanoindentation is derived from the classical hardness test, but takes place on a much smaller scale. A diamond tip of known geometry is pressed into the surface to be tested. The load placed on the tip of the indenter is increased further as the tip enters the sample, soon reaching a user-defined value. At this point, the load can be kept constant for a period or removed. The hardness, H is defined as the maximum load, P max, divided by the residual indentation area, Ar

Due to the miniaturization of the structure, it is possible only with great effort to measure the area of the hardness impression remaining in the test specimen, as is done in conventional methods for measuring hardness. Therefore, in the nanoindentation during the experiment, the applied penetration force and the penetration path of the tip are simultaneously measured. Due to the known geometry of the indenter and the measurement data for penetration force and penetration, the contact surface, and subsequently the hardness can be calculated. the typical load displacement curve obtained during the nanoindentation test is shown the following figure.

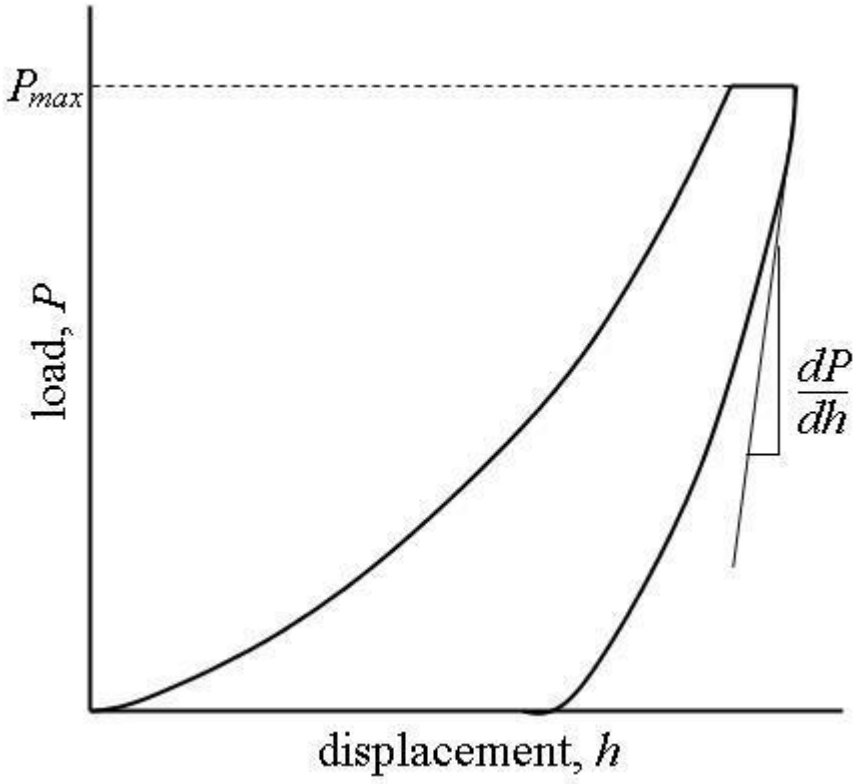


**Figure III.8- Typical load-displacement curve for nanoindentation test.**

The Nanoindentation measuring head consists of a three-plate capacitor and is mounted on an optical or atomic force microscope. When an electrical voltage is applied to the capacitor, a force is created on the middle capacitor plate, which presses a pin with a diamond tip into the surface to be tested. The displacement of the middle capacitor plate causes a capacitance change

of the capacitor and gives the required force and penetration depth data for determining the hardness. The boundary between the micro and nano-measuring ranges is defined as 0.2 μm according to DIN EN ISO 14577. However, most instruments for instrumented penetrant testing also measure in the micro range up to the limit of the macro test range of 2 N.

In our study, nano-indentation tests were performed with a nano-indenter using a Bruker AXS BW/508/98/RÖ CSM tester at CDTA center, according to Oliver-Pharr method. A Vickers indenter with a maximum load of 100 μN was used. The indentation velocity was fixed at 2500 nm/min and the dwell time to be maintained at the maximum load at 10 s. The charge/discharge velocity was equal to 200 μN/min.

## III.3. Electrochemical characterization

### III.3.1. Potentiodynamic measurements

To characterize the corrosion behavior of the coatings in the NaCl and $Na_2SO_4$ solutions potentiodynamic measurements were conducted at different concentrations (1g/l, 10g/l, and 35g/l) and that at ambient temperature at the national polytechnic school.

we carried out tests of polarization in a conventional three-electrode cell (Figure 9). Data acquisition from the potentiostat is done via the VoltaLab software.

The installation comprises:

- The working electrode.
- The counter electrode.
- Reference electrode.

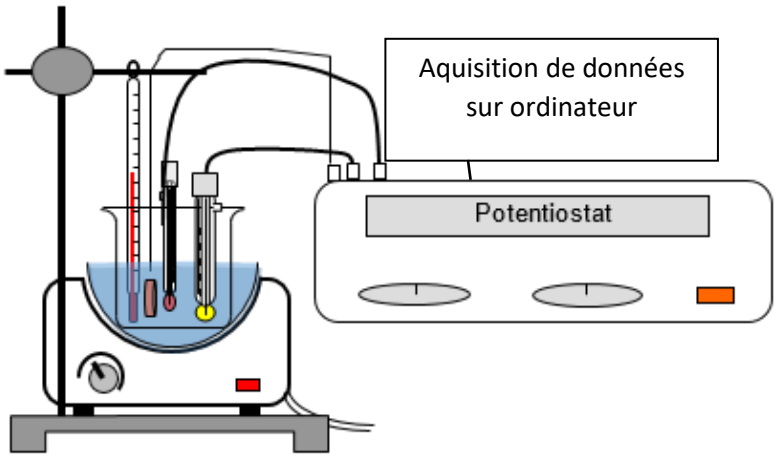


**Figure III.9- Diagram of the assembly carried out for the polarization tests.**

These tests were done to characterize the corrosion behavior of the surface for each coating. In each manipulation, we filled a beaker with the chemical solutions in which we perform the electrochemical tests. Then, we plunge the three electrodes; we wait for the measurement of open circuit potential for a period of 30 minutes. Then we start the test.

For these tests, the potential range chosen is between [-1000, 0 mV]. The scanning speed is 0.2 mV / s. which implies a duration of 30 min.

## III.3.2. Electrochemical Impedance Spectroscopy

The electrochemical impedance measurements were performed at open circuit potential at a sine perturbation amplitude of 10 mV and that between 100 kHz to 1 Hz of frequency. For these measurements, the acquisition rate was fixed at 5 per decade and the open circuit stabilization time was set at 30 minutes.

## III.3.3. Electrochemical methods

The electrochemical analyzing methods have an important place among all the other characterization techniques. It is well known for their accuracy and sensibility. It is widely used for the assessment of the interfacial properties of materials after their interaction with an electrolytic medium. They allow us to estimate the corrosion rate at the moment of measurement. They precisely provide information about the mechanisms which are responsible for the surface degradation to the extent that these information are correctly interpreted.

The electrochemical analyzing methods can be classified into two different categories:

- Stationary methods.

- Transitional methods.

### III.3.3.1. Stationary methods

The stationary methods allow the study of a system in a thermodynamic equilibrium state by taking into account all the redox couples in the solution.

#### III.3.3.1.1 Open circuit potential

This potential, also called free potential or open circuit potential, is measured under the test conditions without imposition of current. During the test, the evolution of the potential of the electrode is recorded as a function of time. After a sufficient time, the potential stabilizes at a constant value that corresponds to the open circuit potential.

#### III.3.3.1.2. Polarization resistance method

With the polarization resistance method, it is possible to determine the corrosion rate. The technique measures the corrosion rate by applying several millivolts around the corrosion potential and the corresponding current (Figure 10).

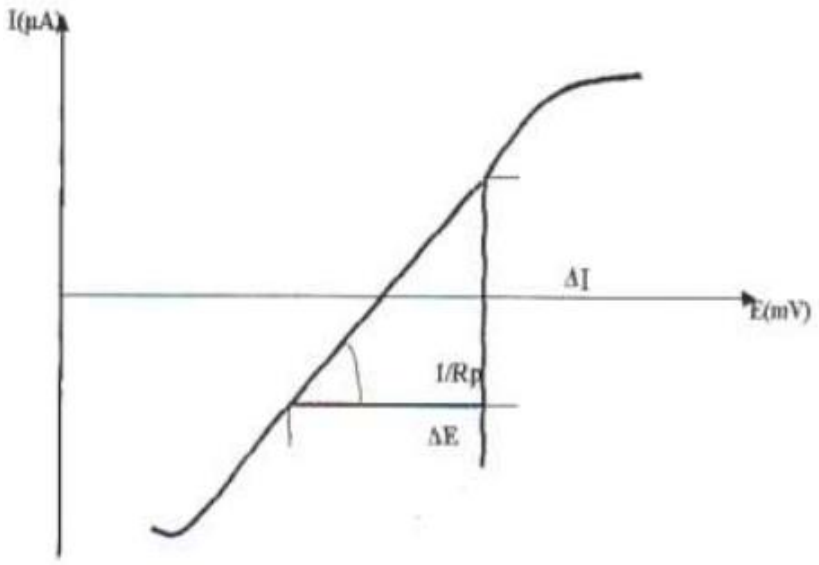


**Figure III.10- The measurement of the polarization resistance.**

The polarization resistance is defined as the derivative of potential to time when the current is null. It's mathematically given by the following relation:

$$R_p = \left(\frac{dE}{dt}\right)_{i=0}$$

The determination of the polarization resistance and the values of the Tafel slopes allow to estimate the corrosion current density by Stern and Geary relation:

$$i_{corr} = \frac{1}{R_p(B_a + B_c)}$$

The constants $B_a$ and $B_c$ are constant values that depends on Tafel slopes, $b_a$ and $b_c$ as follows:

$$B_{a/c} = \frac{ln10}{b_{a/c}}$$

Then another mathematical relation can be deduced:

$$i_{corr} = \frac{1}{2.3\ R_p}\left(\frac{b_c b_a}{bc + ba}\right)$$

**III.3.3.1.3. Tafel method**

With Tafel extrapolation, it is possible to approximately determine the electrochemical parameters that characterize the corrosion kinetic of a material in contact with an electrolyte (electrochemical cell). The extrapolation allows to determine either corrosion current, corrosion potential or by extention corrosion rate using Tafel slopes. The calculation of Tafel slopes uses the two portions of the curve i = f (E) (Figure 11): the portion by which the Tafel line has a positive slope (the potential is superior to the corrosion potential (anodic domain)) and the portions for which the Tafel line has a negative slope (the potential is inferior to the corrosion potential (cathodic domain)).

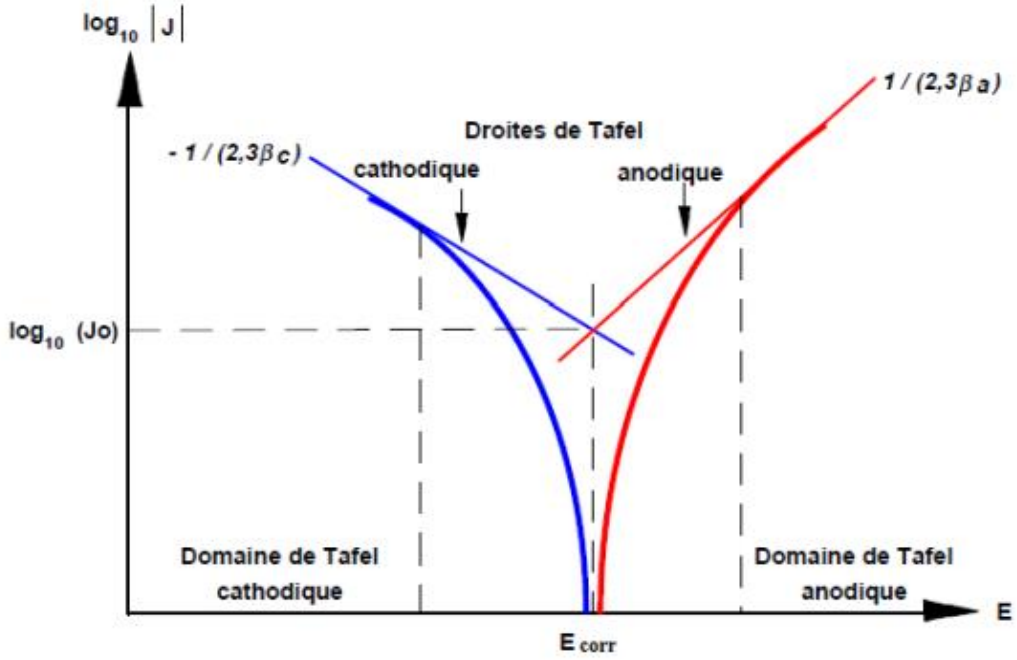


**Figure III.11- Determination of electrochemical parameters from Tafel's straight lines.**

This method is based on the Buttler-Volmer equation:

$$i = i_0\left(exp\left(\frac{\alpha zF}{RT}\eta\right) - exp\left(-\frac{(1-\alpha)zF}{RT}\eta\right)\right)$$

For the anodic portion:

$$i_a = i_{corr} exp\ \frac{2.3\eta_a}{b_a}$$

with :

$$\eta_a = E - E_{corr} = a + blog\ (i)$$

where :

$\eta_a$ : anodic overpotential.

a : the ordinate at the origin.

For the cathodic portion:

$$i_c = i_{corr} exp\ \frac{2.3\eta_c}{b_c}$$

with :

$$\eta_c = E - E_{corr} = a' + b' log\ (i')$$

where :

$\eta_a$ : cathodic overpotential.

a' : the ordinate at the origin.

The two equations of $\eta_a$ and $\eta_c$ represent the simplified form of Tafel law and indicate that the curve log (i) = f (E) must have two linear straight lines, which are called the straight line of Tafel. The intersection of these lines define the corrosion point.

As seen before (Figure 11), it's possible to experimentally determine the electrochemical parameters with a logarithmic representation of the current density, as it highlights the linear relationship between the logarithm of the current density and the potential.

**III.3.3.2. Transitional methods:**

These methods help to study the mechanisms of corrosion and protection of metals. Some of them are used to measure the rate of corrosion. Unlike stationary methods, the transitional methods make it possible to differentiate the reaction phenomena by their relaxation time.

The transient methods consist in imposing a variation of potential or current, then measuring the response of the studied system to this disturbance.

The different transient methods are differentiated from one another by the amplitude of the respective applied signal.

**III.3.3.2.1. Electrochemical impedance spectrometry**

The electrochemical impedance spectroscopy is a kind of non-destructive testing method which does not disturb the analyzed surfaces. This technique is based on the measuring of the current in a range of frequencies after applying an alternative potential of small amplitude on the working electrode. The small applied voltage make the system under investigation in quasi-equilibrium state. The main parameters to be fixed during EIS tests are the potential of perturbation and data rate acquisition. The non-linearity of most electrochemical systems requires local analysis around a polarization point and the use of a low amplitude perturbation signal as shown in the Figure below.

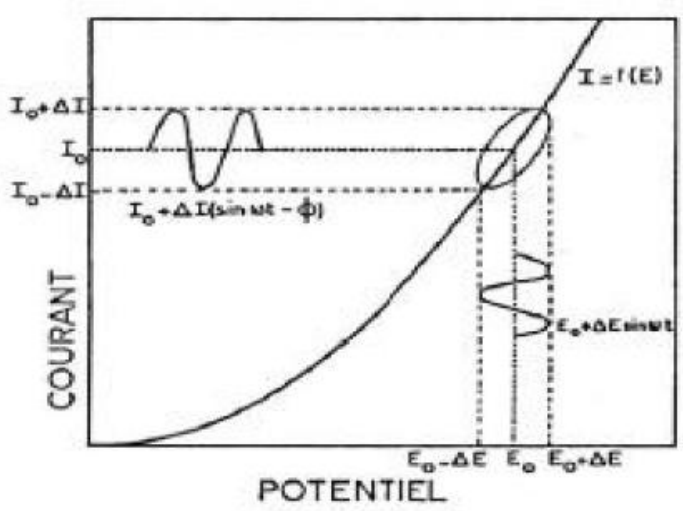


**Figure III.12- Representation of electrochemical conditions on a current-potential curve.**

In potentiostatic mode, a sinusoidal interference signal ΔE will give a sinusoidal current response ΔI which will be out of phase by an angle φ with respect to the potential:

$$\Delta E = |\Delta E| sin\omega t$$

$$\Delta I = |\Delta I| sin(\omega t - \varphi)$$

The impedance Z (ω) is defined as the ratio between the perturbation signal and the associated response:

$$Z\ (\omega) = \frac{\Delta E}{\Delta I}$$

A metal-solution contact can be represented by an equivalent electrical circuit that takes into account the electrochemical phenomenon at the interface.

### III.3.3.2.2. Impedance representation:

The representation of the impedance can be done according to two types of representation: the representation of Bode and the representation of Nyquist.

#### III.3.3.2.2.1 Nyquist representation:

It is a representation in the complex plane with two perpendicular axes. On the abscess the real part of the impedance Z'= Z cos ω is represented, while on the ordinate, it is the imaginary part Z''= Z sin ω which is represented and that for a range of frequencies. The figure 13 shows a semicircle that intersects with the real axis at two points, each one corresponds to a resistance. For the higher frequencies the intersection point gives the ohmic resistance of the electrolyte Re. For the lowest frequencies, the intersection point corresponds to the sum of Re + Rt where Rt is the

charge transfer resistance. The frequency which corresponds to the maximum of the imaginary part makes possible the determination of the double layer capacity Cd by applying the following relation:

$$\omega Z_{max} = \frac{1}{C_d . R_t}$$

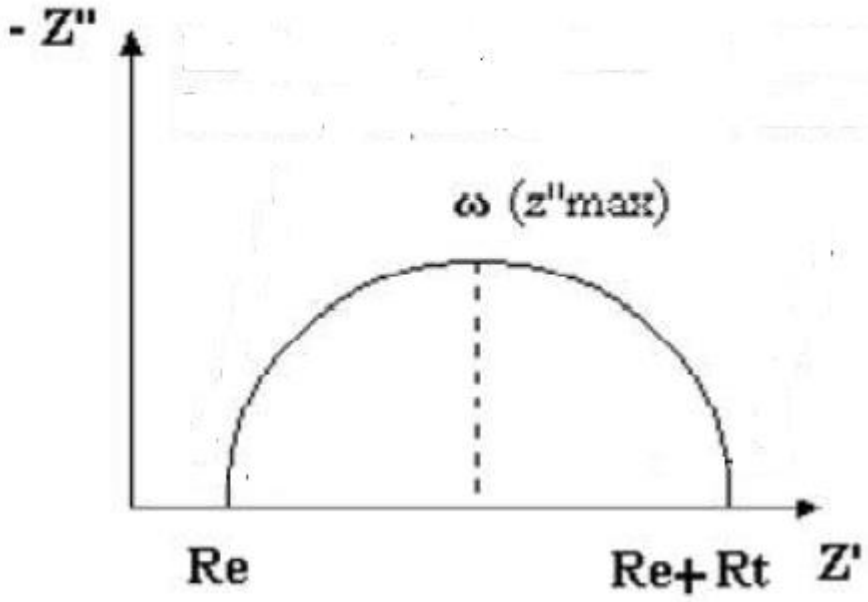


**Figure III.13- Nyquist diagram of a reaction under activation control.**

### III.3.3.2.2.2 Bode representation:

In Bode representation (Figure 14), on the abscess, the logarithm of the pulsation is plotted against the logarithm of the impedance module on the ordinate. The curve obtained makes it possible to determine the resistance of the electrolye Re , the sum of the resistance of the electrolyte with the resistance of the charge transfer (Re + Rtc) and the inverse of double layer capacity 1 / Cd by extrapolation of its central linear part. The other curve log | Z | = f (log ω) has a maximum that allows the calculation of Cd. This representation gives the same information as the Nyquist representation but offers the advantage of shortening the duration of the measurements made in the low frequency domain.

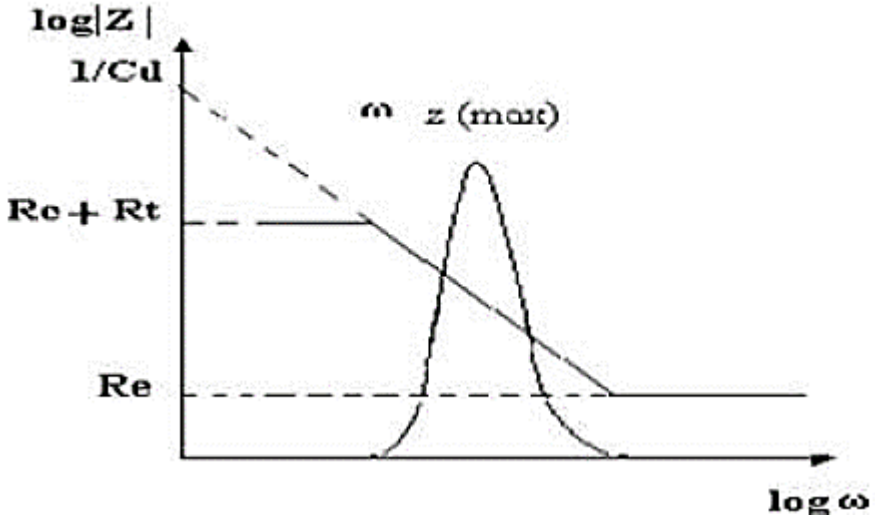


**Figure III.14- Bode diagram of a reaction under activation control.**

## III.4. Profilometry analysis

Profilometry measurements were carried out on the top surface of each coating together with the steel substrate before and after grit-blasting and bond layer deposition. The purpose was to characterize the surface morphology and to get the surface roughness of the analyzed surfaces. The used profilometer is equipped with a laser that reads the altitude as the profilometer moves along the surface. For the roughness profiles, the parameter Ra refers to the arithmetic mean roughness which is defined by the following relation:

$$R_a = \frac{1}{l}\int_0^l |Z(x)|dx$$

While Z is the height and l the length of the analyzed line.

# Chapter IV :

# Results and Discussion

## IV Results and Discussion:

In the present chapter, we will flesh out and discuss the obtained results. It's about the microstructural characterization and the mechanical indentation and the corrosive behavior of two type coatings designed to coat the drilling bits. The first coating (coating A) was obtained from the spraying of Spherotene wire while the second (Coating B) is a NiFeCrBSi alloy reinforced with WC.

## IV.1 Top Surface Characterization of Coating A

Figure 1 shows a 3D representation of the surface topography for the coating with that of the steel substrate before and after grit blasting and bond layer deposition.

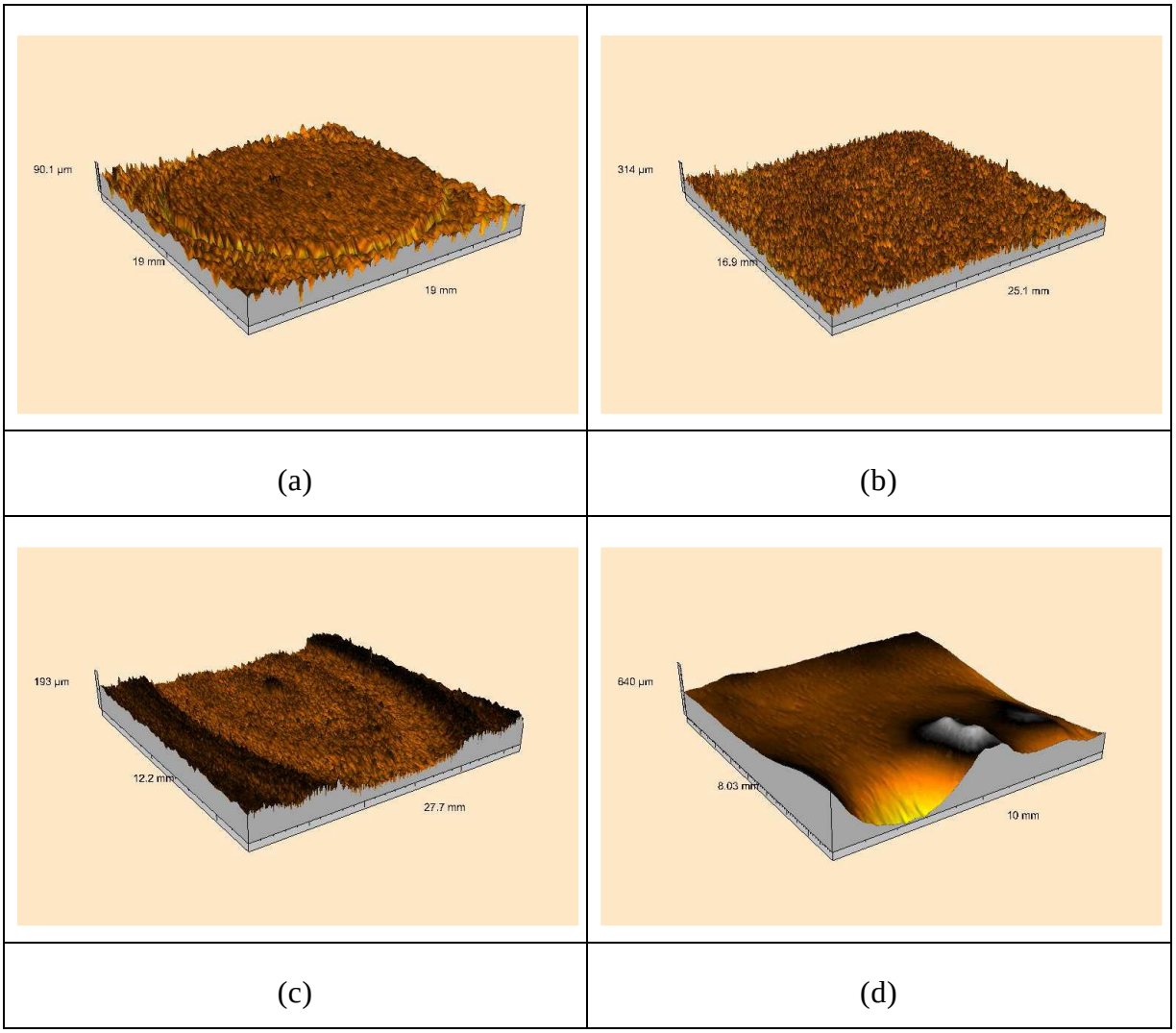


(a) (b)

(c) (d)

**Figure IV.1- 3D rebuilding of the surface roughness of (a) the substrate, (b) the substrate after grit-blasting, (c) the substrate after bond layering, and (d) the substrate after deposition of the coating.**

The purpose of performing the spray pretreatments was to achieve a value of roughness that approaches (~11 µm), which was found the best for assuring good adherence to the substrate in industry. The roughness of the substrate increased from 2.92 µm to 5.11 µm and then to 12.5 µm, respectively after grit blasting and bond coat deposition. Comparatively to the other surfaces, the substrate surface can be marked by the lowest value of roughness and by the presence of circular cradles. These cradles were produced when the samples were cut by a machining operation. The coating is characterized by the presence of tiny like pits at the top surface of the metallic matrix. That indicates that there is a difference in the superficial tension in the melting pool. The WC particles that are on the top of each surface appear in the 3D representations in the form of balls. Some of them appear clearly in grey. The roughness of the coatings provides good wear performance to the steel body which is covered by the coating. For that reason, this kind of coating is difficult to be polished with abrasive papers and is hard to obtain mirror-like surfaces. However, various machining techniques including diamond machining and grinding were suggested to be used to rapidly modify the surface profile of the coatings [1].

## IV.2 Microstructure of Coating A

The performance of any coating strongly depends on its metallurgical characteristics. These characteristics can differ from one coating to another depending on the microstructure that composes them. Thus, the understanding of the behavior of any industrial component should pass by the study of the properties of the individual phases which define the microstructural state of a material. Generally, the microstructural state of a coating is a feature that marks the process by which the coating was performed. Figure 2 shows the microstructure of coating A. From these micrographs, it can be seen that the nickel-based feedstock materials were completely melted into a multiphase matrix which is reinforced by the presence of WC particles. These particles are randomly distributed inside the matrix with either spherical or irregular shapes. The matrix of coating consists of nickel dendrites which are surrounded by the eutectic phase. Within the coating, the dendrites were preferentially initiated around the WC particles and are oriented in opposite directions. This particular orientation suggests that residual stresses are present in various locations in the coatings. A certain number of voids and porosity were found inside the coatings.

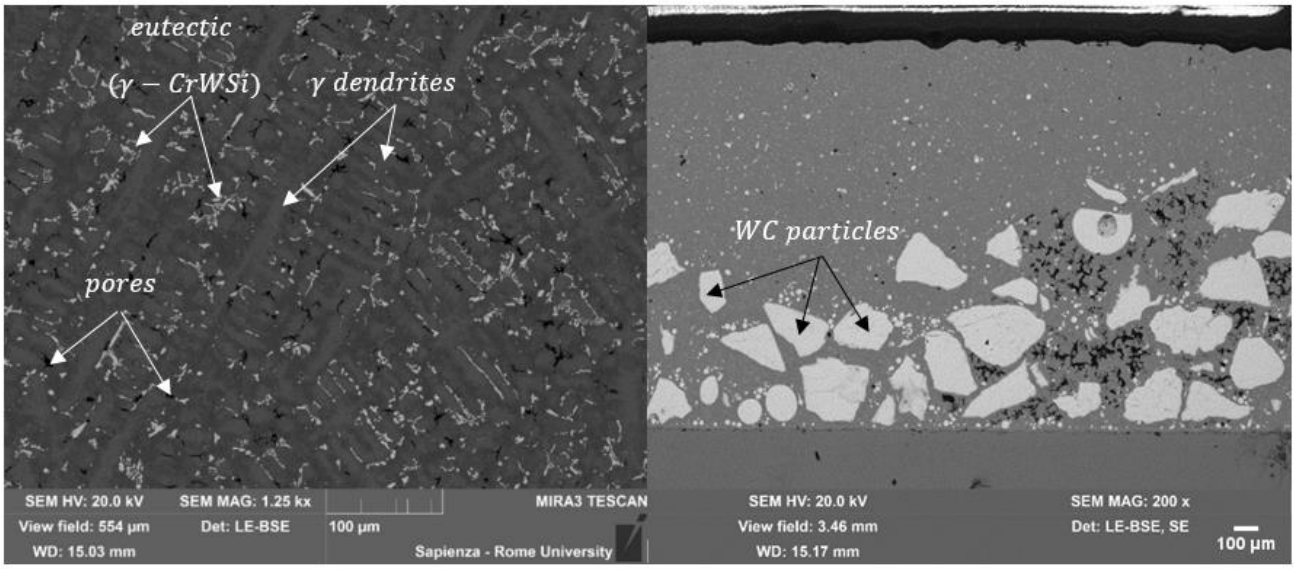


(a) (b)

**Figure IV.2- Microstructure of (a) the top and (b) the cross-section of coating A.**

The formation of these defects is presumably due to the entrapment of gas inside the coatings during the processing. The pores have an irregular or spherical-like shape. They appear in the micrographs in a dark threshold. No micro-cracks or unmelted nickel particles were observed inside the coatings. The inter-splat boundaries between the deposited layers were completely disappeared. This may be attributed to a post-heating of the nickel self-fluxing matrix. The flame moves at a low speed at a short distance from the substrate. It provides then an excess of heat to the nickel matrixes, which impedes the rapid solidification of the nickel matrix and contributes to the elimination of the inter-splat boundaries.

## IV.3. SEM and EDS Analysis

Inside coating, the Ni-$\gamma$ ($Ni_3Fe$) dendrites are the first to be formed when the feedstock material is propelled to glance on the steel substrate [2]. However, as the boron and the carbon have a low solubility in the nickel dendrites, they are rejected in the remaining melt during the solidification. As the cooling continues the eutectic-like structure forms in an interdendritic region. According to the EDS results (Figure 3), this phase is composed of $\gamma$ nickel solid solution ($Ni_3Fe$) and CrWSi based constituent that contains a certain amount of Mn.

With the decrease of the temperature, several sites that are enriched with chromium, carbon, and boron become unstable and undergo a solid-state transformation to give carbides and borides by a mechanism of controlled diffusion through the interference with the $\gamma$ nickel phase. The Ni-$\gamma$ phase present in the eutectic contains silicon and is depleted in W, as compared with the Ni-$\gamma$ phase which composes the dendrites.

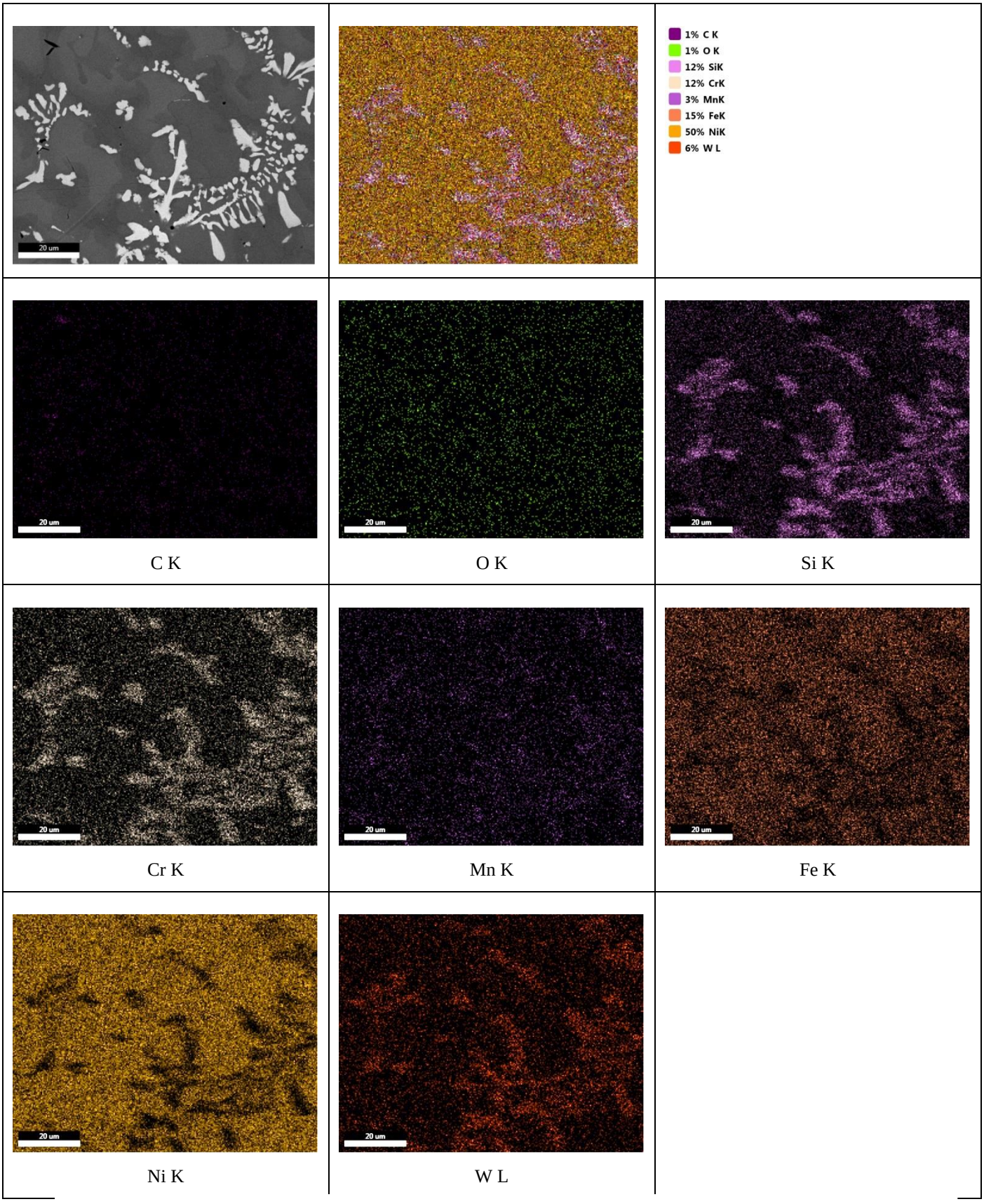


**Figure IV.3- EDS mapping showing the distribution of the chemical compounds within the matrix of coating.**

The grain boundaries between these two different constituents contain further oxygen together with all the chemical elements present in both phases. This confirmed that the formation of the eutectic was done through a controlled diffusion process which was occurred at the interface between the dendrites and the remaining melt.

The detected oxygen is entrapped in the boundaries mainly due to surface oxidation of the inflight particles (Figure 4 and Table IV.1).

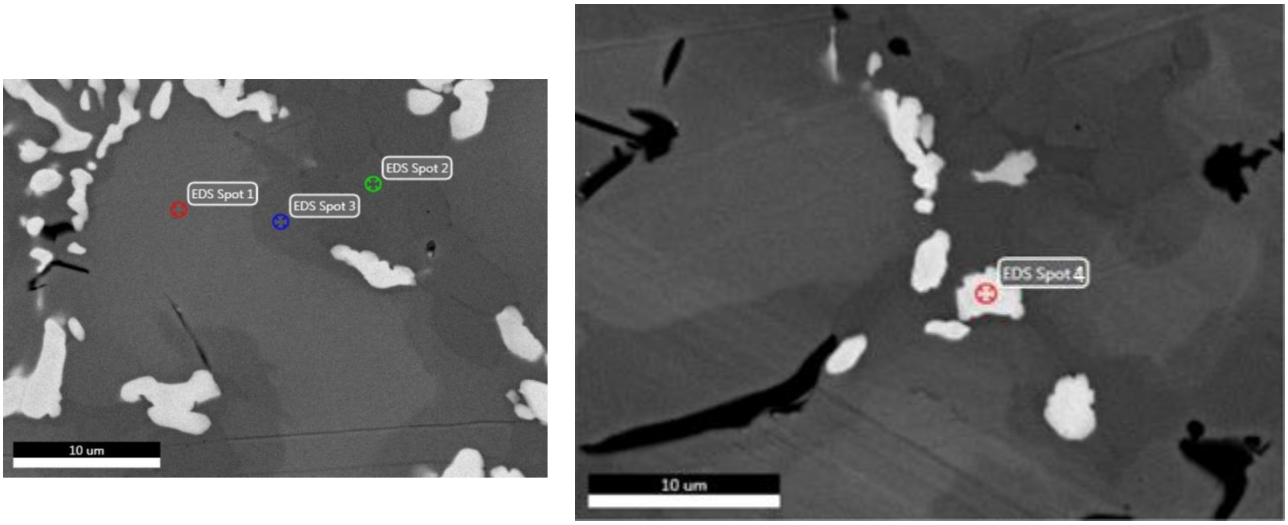


**Figure IV.4- EDS point analysis showing the difference in the chemical composition between the dendritic γ phase, the eutectic γ phase and the formed chromium carbide.**

**Table IV.1-**Chemical composition of the γ nickel phase and the chromium carbide.

| Element | Ni | Fe | W | Cr | C | Si | O |
|---|---|---|---|---|---|---|---|
| Dendritic γ (%wt) (Spot 1) | 68.45 | 14.82 | 7.38 | 4.65 | 4.71 | - | - |
| Eutectic (γ phase) (%wt) (Spot 2) | 74.07 | 12.64 | - | 2.93 | 5.99 | 4.36 | - |
| γ/γ Interface (%wt) (Spot 3) | 67.79 | 13.84 | 5.8 | 3.92 | 6.79 | 1.51 | 0.34 |
| Chromium carbide(%wt) (Spot 4) | 17.20 | 3.91 | 45.47 | 22.19 | 11.12 | - | - |

This phenomenon was observed by Deshpande et al. in the case of nickel sprayed alloys [3]. Indeed, the nickel oxidation mechanism differs depending on the used processing techniques. For the flame sprayed coatings, the oxidation is caused by the higher temperature and the viscosity of the in-flight particles. The nickel is propelled in a superheated state as droplets with the WC carbides which remain in their unmelted form. In this condition where the spraying is

performed in the open air, the oxygen tends to diffuse for a short time during the inflight period (according to the Ellingham diagram) as the spraying distance was kept at its minimum. The diffusion of oxygen alters the surface chemistry of the particles by forming a nickel oxide. The chemical composition of the nickel oxide approaches that determined by the EDS analysis which was reported in Table IV.1 (Spot3). Other chemical compositions of the feedstock material may generally lead to the formation of other oxides. Deshpande et al. [3] found that with 5% of Al in the chemical composition of a Ni-Al alloy, $Al_2O_3$ was formed along with NiO due to oxidation. Katranidis et al. [4] and Verdon et al. [5] found that the oxygen remains confined in the splat boundaries after deposition. However, the particular self-fluxing effect of the nickel matrix and the adequate processing parameters play a significant role in the splat boundaries elimination. Thus, the oxygen doesn't retrieve a place only on the voids and the grain boundaries. The non-porous microstructure permits the use of the coating for a wide range of applications where higher corrosion in aggressive environments is expected. Incorporation of Zr in the chemical composition of the composite is recommended to reduce further the oxygen content in the coating [6]. The dark contrast in the SEM refers to voids and porosities.

The relatively heavy nature of W is responsible for the bright contrast of the CrWSi eutectic constituent. W is present within the CrWSi constituent due to an intensified dissolution of the WC carbides in the melted nickel binder. The dissolution (Figure 5) was activated via an interdiffusion process when the WC particle gets wet with the melted nickel binder.

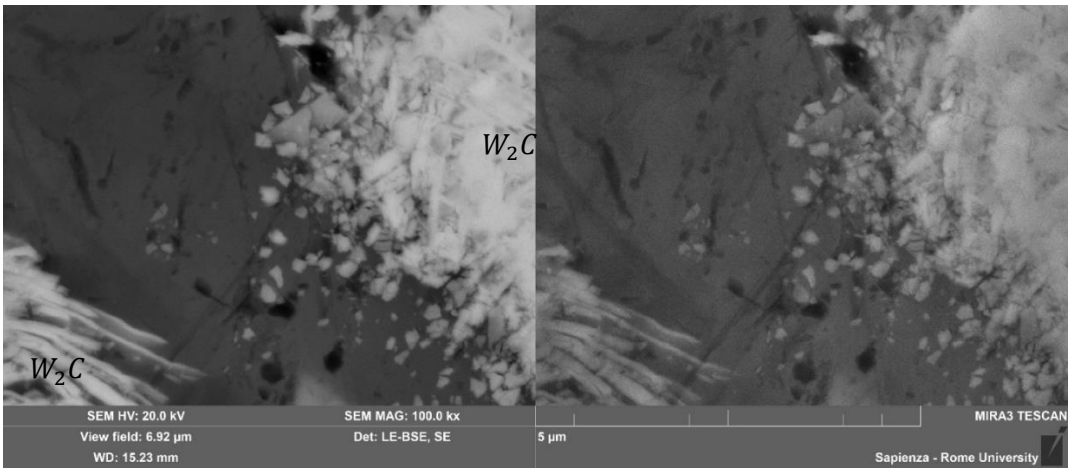


(a) (b)

**Figure IV.5 - Micrographs showing the result of the dissolution of WC carbide within the coating: (a) backscattered electron image, (b) secondary electron image.**

During the deposition, the dissolution is fostered due to the strong chemical affinity between nickel, carbon, and tungsten. The mutual elemental diffusion of the chemical compounds increases the cohesion of the WC carbides with the nickel matrix, which makes the detachment of the carbides difficult. In this way, improved wear resistance can be achieved. On another hand, the decarburization of WC carbides takes place when these carbides reach a temperature of about 1200°C [7]. This chemical reaction yields W and $W_2C$ semi-carbides and is the result of direct oxidation which was occurred according to the following chemical mechanism [8]:

$$2WC+O_2 \leftrightarrow W_2C+CO_2$$

$$2W_2C+O_2 \leftrightarrow 2W_2(CO)$$

$$W_2(CO) \leftrightarrow 2W+CO$$

$$2WC \leftrightarrow W_2C+C$$

The part of carbon that results from the oxidation of WC particles is released as carbon dioxide. After the decarburization of WC, another part of carbon is produced and diffuses to contribute to the formation of secondary precipitates such as chromium carbides ($Cr_{0.46}Ni_{0.31}W_{0.27}Fe_{0.08}$ C) (Table IV.1). The brittle $W_2C$ phase surrounds the WC particles with its eutectic form. It occupies the space left by the atoms of carbon. $W_2C$ phase is well known for its brittleness. Its presence in the coating gives the composite good resistance to penetration while reducing the fracture toughness. During the cutting of the material from the drilling bits, these properties are important and the best combination can help to reduce both the cracks formation and the intrusion of minerals present in the rock formations such as magnetite, during drilling [9]. As chromium is present in the matrix and because the tungsten and carbon can diffuse to it, the chromium-based intermetallic phase is formed around the WC particles.

The decarburization of WC is affected by numerous factors such as the size, the distribution, the dislocation density [10], the morphology of these carbides, and the presence of twins within the WC grains [11]. The spherical WC particles can mostly be subject to a pronounced dissolution due to a higher dislocation density of the WC grains. The decarburization becomes worse and results in just a few amounts of $W_2C$ with the WC particles that have an irregular or angular shape. Inversely, the WC particles with small size decarburize easily and give a higher

amount of WC because they have higher plasticity [12] and surface energy that result from a higher volume to surface ratio. However, some of them retain their spherical shape despite dissolution and decarburization.

As seen before, WC carbides are not distributed homogeneously in the nickel-based matrixes. Indeed, they have a density ($\sim 15800\ kg/m^3$) which is approximately twice that of nickel ($\sim 8900\ kg/m^3$). After the impact, these carbides fall in the melting pool taking the way toward the substrate. For that reason, there are more WC carbides on the middle and the bottom of the coatings rather than on the top. In other words, the volume density of WC on the top of coatings is lower than that on the middle and the bottom. This can, unfortunately, facilitate the removal of the material at the primary moments of drilling as the top layer, which is composed of nickel and a limited number of WC carbides, will be removed easily. However, as the drilling continues progressively, the superficial density of the WC increases. The encountered part of the composite will be harder and the wear rate of the coating will be then improved. After a working cycle and after the repairing of the drilling bits with newly deposited composite coating, the lifetime of the drilling bit will be more improved. The reason behind that is that the new coating is deposited on a layer that is filled with WC carbides.

## IV.4 X-ray diffraction pattern Analysis

The identification of the phases only using X-ray diffraction is complex and difficult due to the overlap of diffraction peaks [13]. The following figure (Figure 6) illustrates the diffraction pattern obtained for coating A.

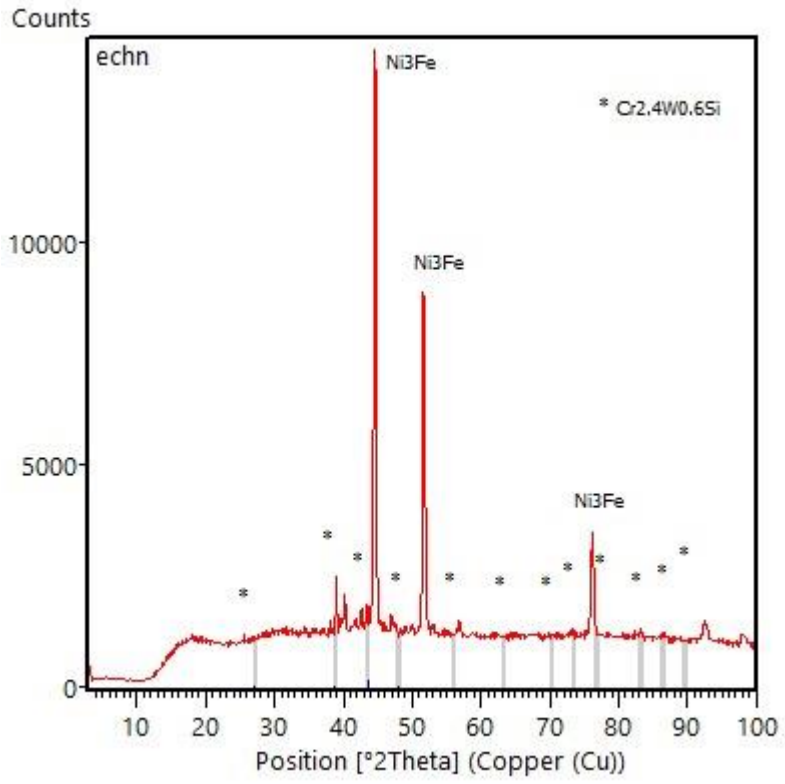


**Figure IV.6- XRD pattern of the coating.**

The result shows that the microstructure is mainly composed of γ ($Ni_3Fe$) nickel solid solution, $Cr_{2.4}W_{0.6}Si$, beside $W_2C$ and WC carbides. However, the peaks that correspond to the chromium carbides ($Cr_{0.46}Ni_{0.31}W_{0.27}Fe_{0.08}$ C) which was previously identified by EDS overlap with the other diffraction peaks and it's difficult to differentiate them from the other peaks.

## IV.5. Substrate/Coating A Interface Analysis

Figure 7 shows a micrograph taken from the substrate/coating interface. The coating mechanically adheres to the substrate. The mechanical adhesion was insured by an anchoring which occurred during the flattening of the particles inflight on the substrate. The interface between the coating and the substrate seems to be slightly free of pores.

According to the EDS results, a slight amount of nickel diffused towards the substrate from the bonding layer. Inversely, a diffusion of iron from the substrate towards the bonding layer also occurred. The small interdiffusion of these elements was due to the chemical affinity that exists between them. It can also be explained by the existence of a chemical concentration gradient between the substrate surface and the bonding layer. The interdiffusion was facilitated by the high spraying temperature of the feedstock NiCr alloy. It's also activated because the steel substrate surface has received a heat flux from the spraying flame by convection. Thus, the coating consequently adheres with metallurgic bonds due to the interdiffusion.

**Interface**

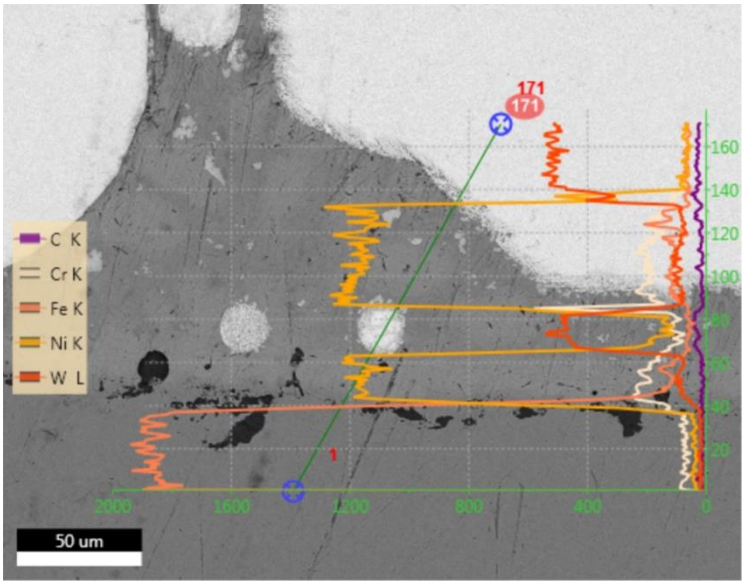


**Figure IV.7- EDS line scan shows the variance of the chemical composition from the substrate to the bottom**

## IV.6. Mechanical Characterization of Coating A

### IV.6.1 Hardness Measurements

The hardness measurements were carried out on both the cross-section and the top surface of the coating, by tapping on the present phases under 100gf and 200gf for comparison. The results are illustrated in Figure 8. Our observations in the variance of hardness, during the test, are mentioned below.

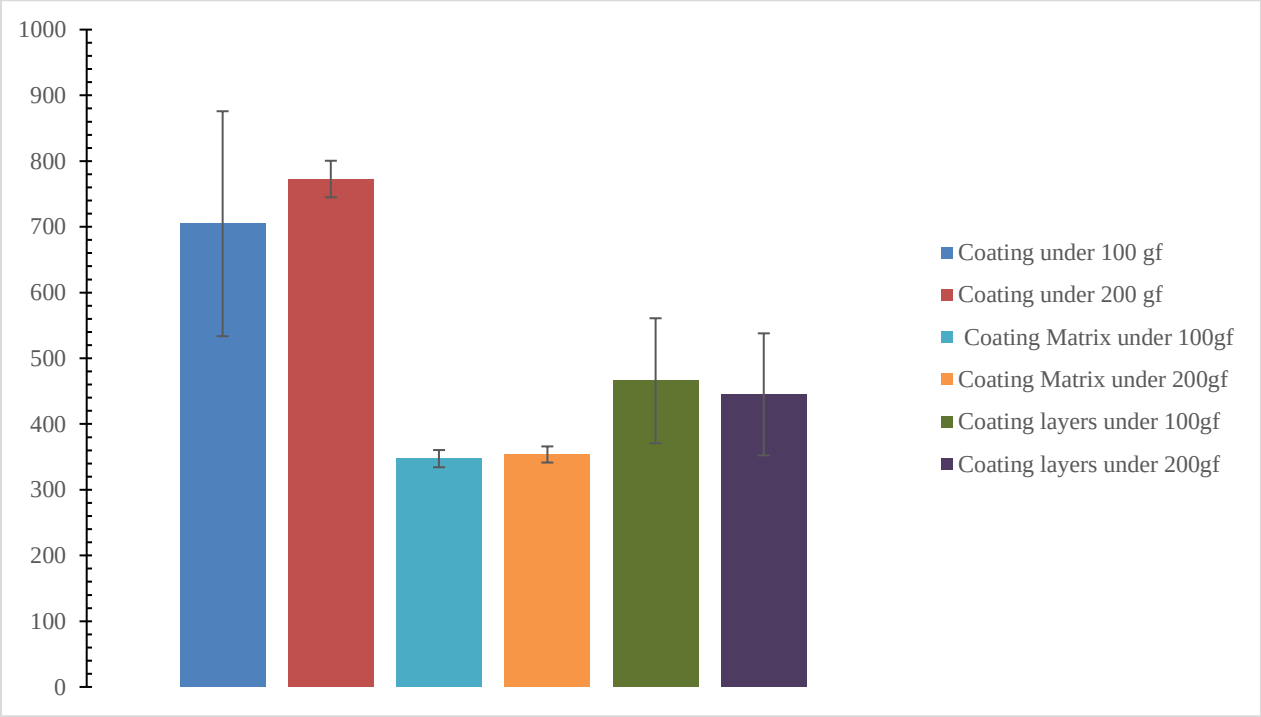


**Figure IV.8- Hardness of the top surface, the matrix, and the cross-section of coating.**

#### IV.6.1.1 Hardness of coating matrix

It appears from these results that on the top of the coating, under a constant charge of 100gf, the mean hardness of the coating matrix is about 347 HV, while that of the tungsten carbides roughly reaches 3027HV. The hardness of WC particles may be higher than their mean hardness value, it may achieve 3500 HV, due to the presence of brittle $W_2C$ phase within them. The presence of voids and porosity within the coating has contributed to the decreasing of hardness in various indented areas where the mean hardness value reaches a value of 278 HV. However, some

regions of the coating were found to have a slightly higher hardness that can attain sometimes a value of 513 HV. These regions presumably contain hard carbides and borides.

Under the charge of 200 gf, the hardness of the matrix takes a mean value of 353 HV. It may reach a maximum value of 441 HV. In the zones where porosities are present, the hardness attains a mean value of about 286 HV. The hardness of WC particles became smaller than the previous values. It ranges between 2296 HV and 2743HV with a mean value of 2525 HV.

#### IV.6.1.2 Hardness of coating

The overall hardness of the composite, when indented at 100 gf, is about 778 HV. This value becomes greater as the indenter was able to hit some large decarburization areas where the hardness reaches 852 HV.

#### IV.6.1.3 Hardness of the substrate

On the cross-section of the coating, the substrate shows a hardness that is very close to that measured for the coating matrix under 200gf (~450 HV). However, these hardness values have a tendency to increase when approaching the substrate/coating interface where the hardness takes a maximum value of 730 HV. The obtention of this value is presumably due to the substrate grit-blasting treatment which plastically deforms the treated surface by increasing its hardness by a strain-hardening.

It is important to note that in the indented areas, there were some differences between the recorded values under 100 gf. the hardness of any indented area generally differs from one zone to another depending on the phase ratio. the chemical composition of the phase and the presence of porosities affect the hardness. The type, shape, and morphology of the indented phases and the presence of defects determine whatever the hardness is high or low. However, after increasing the indentation charge to 200gf, the differences between the obtained values become smaller.

#### IV.6.1.4 Hardness of the cross-section of coating

As depicted in figure 8, under 100gf, the coating layers of the coating have a mean hardness of 465 HV. This value decreases to 445 HV under 200gf. This difference in hardness confirms that even the coating is inhomogeneous, from the cross-section, the hardness depends on the distribution of WC and voids.

### IV.6.2 Microhardness Measurements of coating A

The cross-sectional micro-hardness evolution profile (Figure 9) demonstrate that the carbon steel top surface has undergone a hardening due to a cold deformation occurred during the grit blasting treatment. On the affected volume and along 150 µm from the interface, the hardness seems to follow a linear-like evolution, suggesting that the more the distance is closer to the interface, the more the surface is plastically deformed, and the more the hardness is high. This result is in agreement with Coddet et al. findings [14].

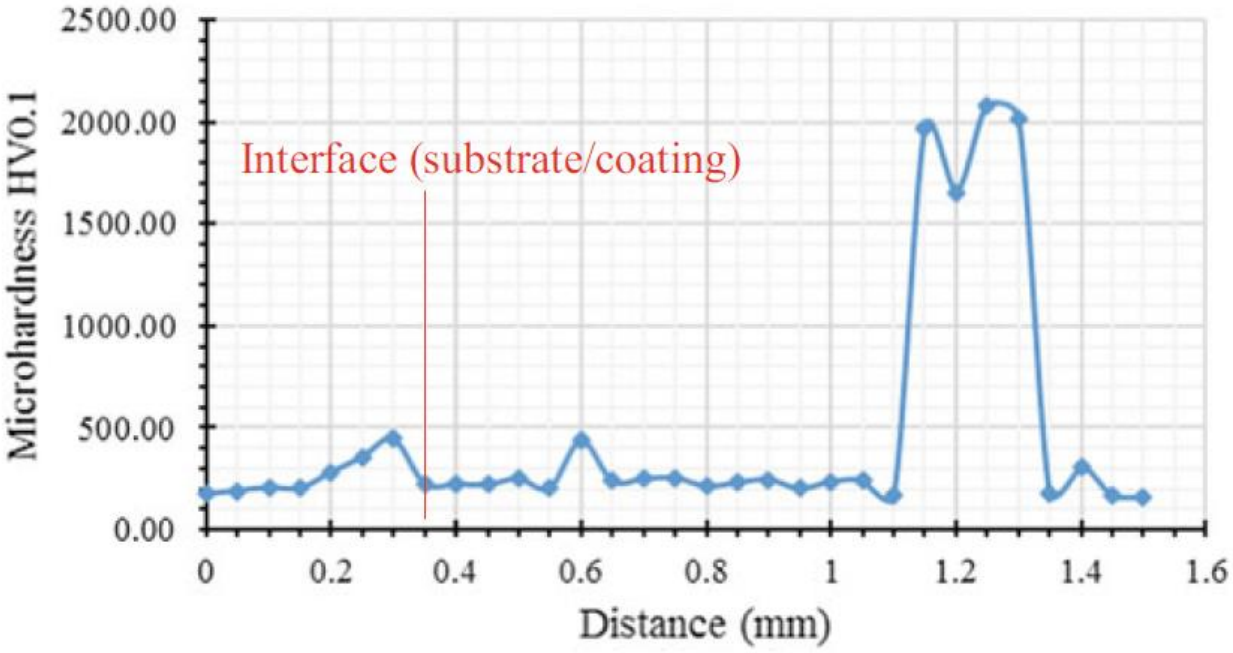


**Figure IV.9- Cross sectional micro-hardness evolution profile**

While the mean hardness of the coating matrix and that of the steel substrates were slightly similar (~210 ± 15 HV), near the interface, the hardness has achieved its maximum value that was around 445 HV. In several matrix areas, the hardness rose sharply because of the presence of hard precipitates. As the residual impressions 'sizes were almost bigger than the precipitates' mean size, the dissimilarity between these relatively high hardness values apparently depends on the type, the shape and the number of precipitates being indented. The *WC* surrounding zones were found to have a remarkable lower hardness attributed to the presence of γ dendrites.

### IV.6.3 Nanoindentation Measurements

For figuring out the main contributable factors to the occasional increase and decrease in the matrix hardness, the nano-indentation tests were performed on various dendritic arm areas starting from the center towards the boundaries. Several tests were further carried out on eutectic regions around which the proportion of phases was not the same.

By analyzing Figure 10, displaying some micrographs captured from the indented surfaces after the nano-indentation tests, it appears that the pop-in event, both of matrix constituents were subjected to, is more pronounced in the eutectic phases comparatively with that emerged in the dendritic arms.

The obtained curves presenting the recorded variation of the applied charge P as a function of the depth of penetration h are shown in Figure 11 and 12. From these results, it can be drawn that the first stage of the loading section in which the nanoindentation curves coincide, indicates that the material has experienced a pure elastic deformation. This stage was then followed by an elastoplastic transition preceding the plastic deformation. After maintaining the load at its maximum value, by unloading the indenter, a systematic elastic recovering goes on as a response from the material against penetration.

For the dendritic indented phases (Figure 10), when the distance from the center is too small, it can be noticed that there is a little difference between the obtained nanoindentation graphs. When this distance becomes closer to the grain boundaries, the associated graph bends sharply to the left. As a result, the elastic domain of that curve becomes less extended as compared with the others. Likewise, in the case of eutectic phases (Figure 11), the curves become more inclined with the small interdistance between the eutectic surrounding dendrites and the decreasing in the size of the nickel grains confined inside them.

Furthermore, after the loading stage, by keeping the loading charge constant at its maximum value, it can be mentioned that no discrepancy in the depth of penetration has been recorded. That confirms that in the indentation stress field, there was any movement of dislocations which prove in particular that the *NiCr* based matrix does not show a creep phenomenon, the Inconel arc sprayed coatings containing porosity and oxides have shown during Mebdoua et al.[15] nano-indentation tests.

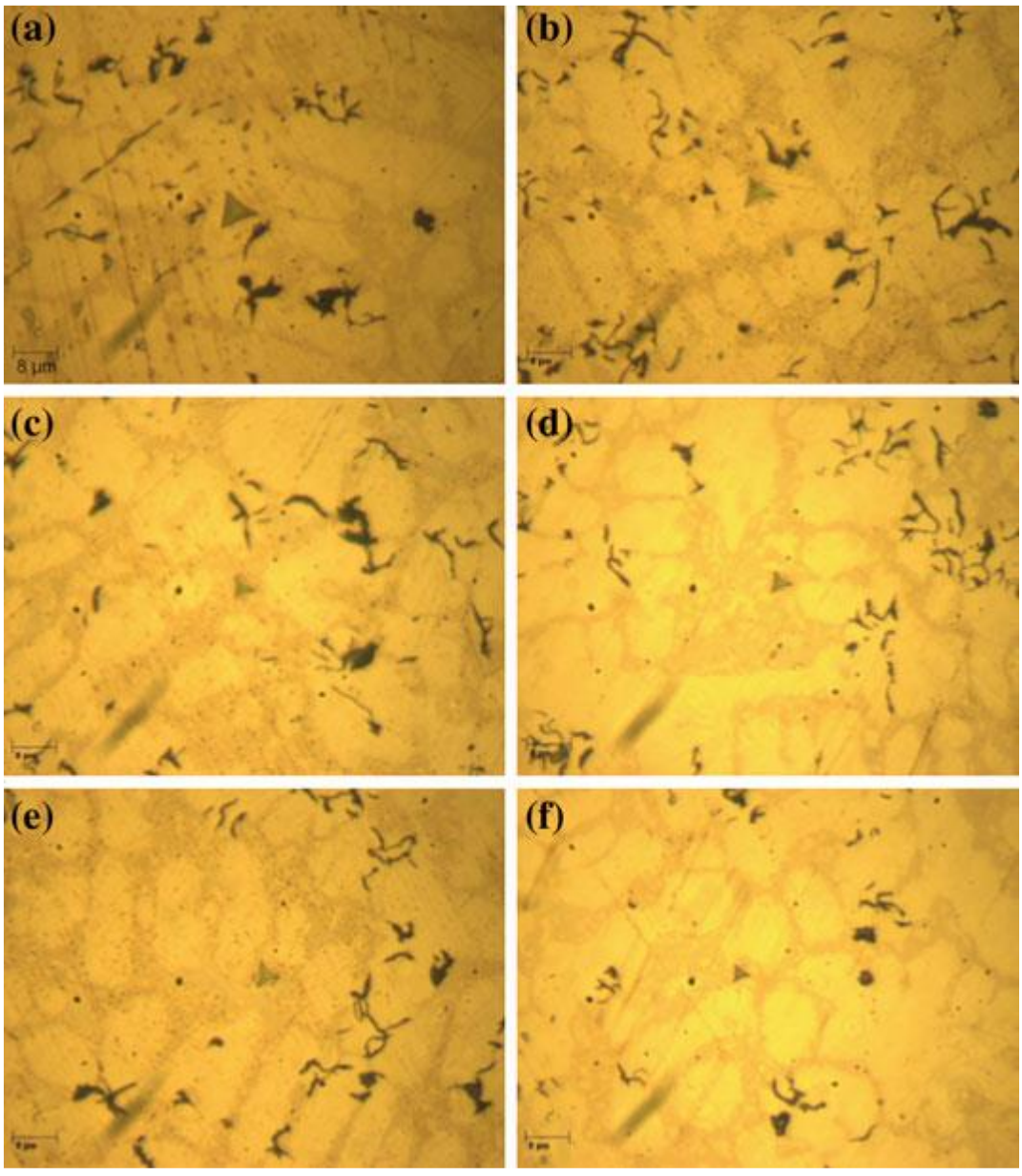


**Figure IV.10- Optical micrographs show various nano-indented surfaces (a, b): nano-indented dendritic regions (d–g) nano-indented eutectic regions**

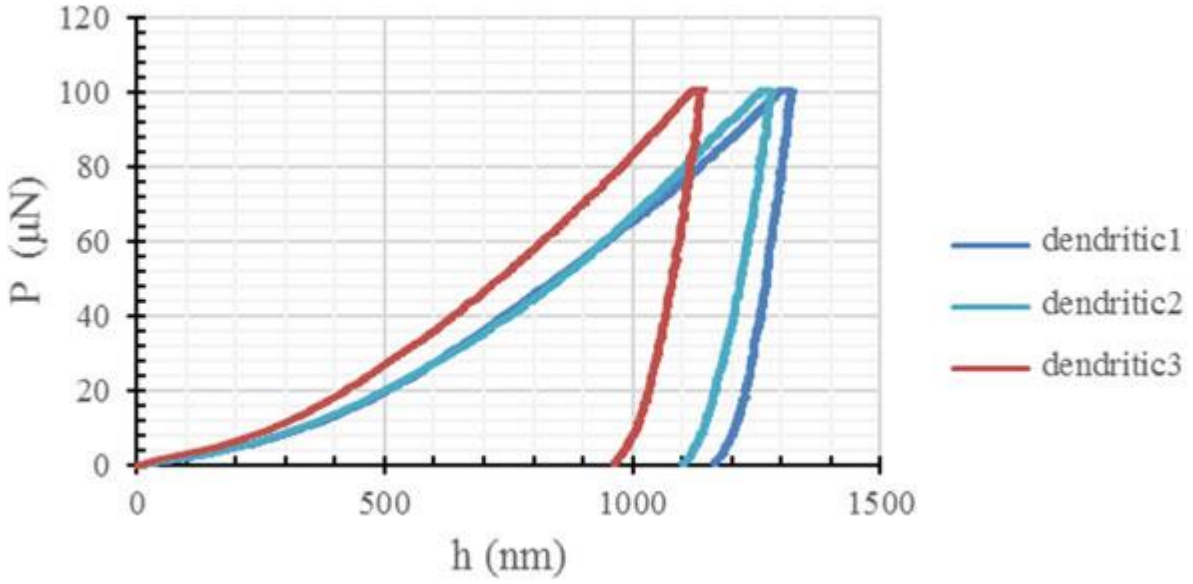


**Figure IV.11- Load–displacement (P–h) curves obtained during nano-indentation experiments carried out on dendritic regions**

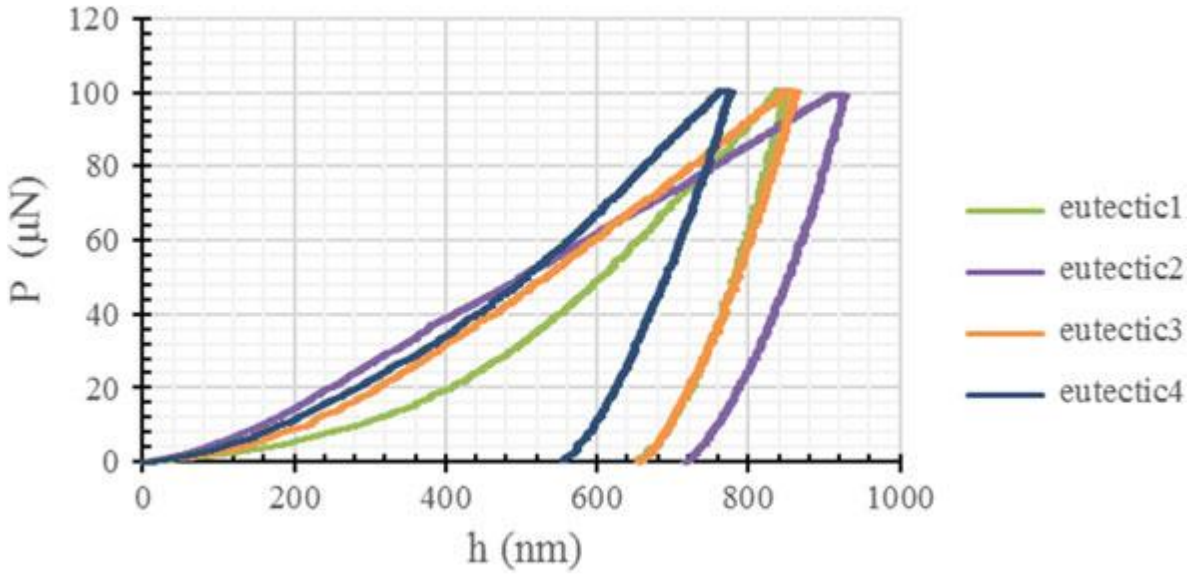


**Figure IV.12- Load–displacement curves (P–h) obtained during nano-indentation experiments carried out on various eutectic regions**

Moreover, the elastic moduli and hardness of the indented phases are listed in Table IV.3. The extracted data from the unloading part of each graph were calculated and summarized in Table IV.4.

**Table IV.2-**The obtained elastic moduli and hardness values after the nano-indentation tests.

| | No. | E (GPa) | Hv10 |
|---|---|---|---|
| Dendritic | 1 | 196.03 | 311.63 |
| | 2 | 160.16 | 343.71 |
| | 3 | 200.35 | 444.22 |
| Eutectic | 4 | 190 | 746.74 |
| | 5 | 207.24 | 903.05 |
| | 6 | 248.71 | 904.33 |
| | 7 | 213.89 | 1217.4 |

**Table IV.3-**The characterizing depths of nano-indentation.

| | No. | $h_m$ (nm) | $h_{rc}$ (nm) | $h_e$ (nm) | $h_r$ (nm) |
|---|---|---|---|---|---|
| Dendritic | 1 | 1317.52 | 1230.65 | 1253.37 | 1167.23 |
| | 2 | 1277.56 | 1169.09 | 1196.76 | 1104.66 |
| | 3 | 1135. 76 | 1033.78 | 1060.34 | 963.49 |
| Eutectic | 4 | 924.84 | 787.42 | 821.57 | 720.09 |
| | 5 | 859.68 | 718.51 | 752.60 | 659.78 |
| | 6 | 843.18 | 721.49 | 752.54 | 655.19 |
| | 7 | 772.10 | 612.39 | 650.12 | 556.12 |

These results indicate that the dendrites' hearts have a mean hardness of 366 Hv and elastic modulus (*E*) of about 185 GPa which result in a low capacity to bear the plastic deformation as the ratio $H/E^2$ is the least. However, the great tendency of hardness to increase has been observed when approaching the grain boundaries. This has been accompanied by a mutual decreasing of all the nanoindentation characterizing depths. That is to say, the depth from the original specimen surface at maximum load *Pm* (*hm*), the calculated depth of the residual impression for an equivalent punch (*hrc*), the elastic displacement during unloading (*he*), and the depth of residual impression (*hr* ) (Table IV.3). Nevertheless, the dendritic hardness values remain inferior to those obtained by indenting the eutectic phases.

As compared with Bezborodov et al. investigation [16] and by relating the results to what was observed from the nano-indentation micrographs, the increase of the eutectic phases hardness

may be attributed to both the smallest size of nickel grains present in the eutectic and the small inter-distance between eutectic surrounding dendrites. However, as many authors expected it [17, 18], the results can be significantly affected by the presence of WC reinforcements beyond the indented surfaces since these can oppose to the indenter penetration and act as an opposing indenter. Therefore, from a metallurgical point of view, the *WC* carbides constitute great impediments to the motion of dislocations formed around them when the plastic deformation is produced leading to a particular strengthening commonly known as Orowan strengthening mechanism. This strengthening can be strictly enhanced by raising the volume fraction of reinforcement carbides and influenced by particles' shape, their typical morphology and their distribution inside the coatings as well. Hence, the thermal mismatch between the matrix and the *WC* carbides contribute separately to the increase of dislocation density within the matrix and consequently to its work hardening.

# IV.7. Electrochemical Characterization of Coating A

## IV.7.1 Potentiodynamic Polarization

The potentiodynamic polarization curves of NiFeCrBSi-WC coating had the same form in the given range of NaCl and $Na_2SO_4$ concentrations (Figure 13 and Figure 14).

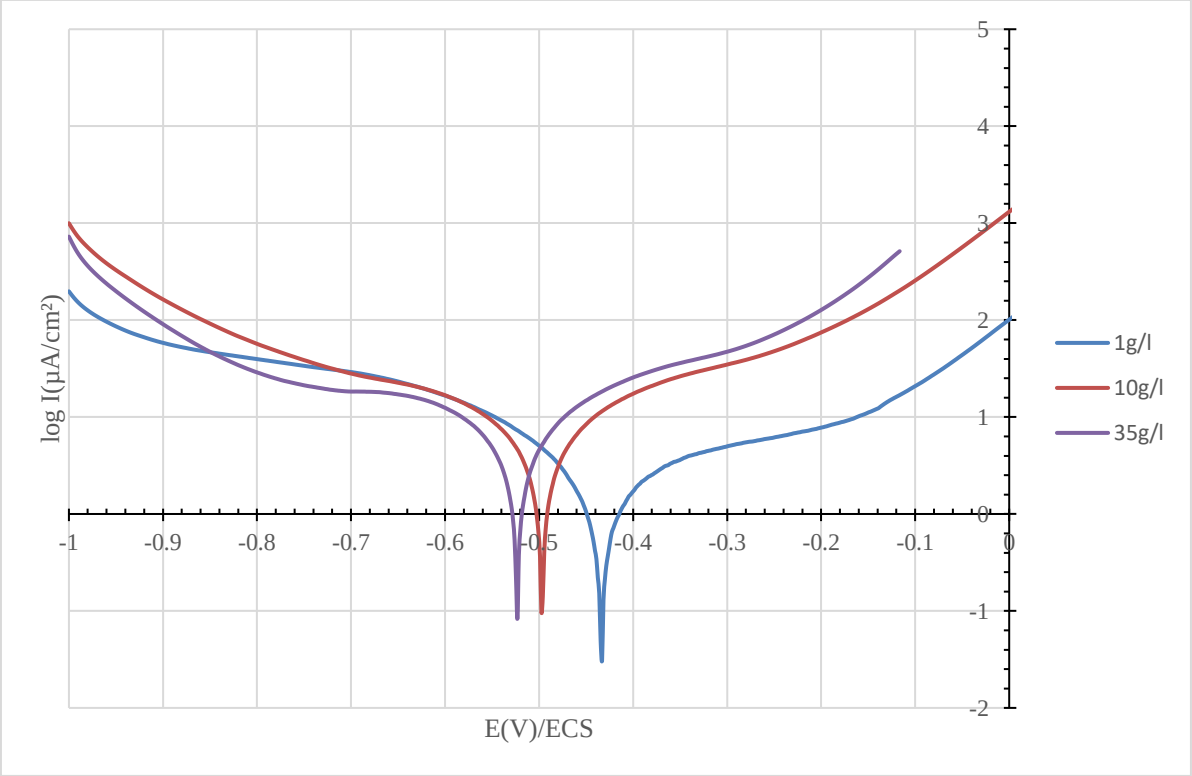


**Figure IV.13- Potentiodynamic polarization curves obtained after the immersion of coating in NaCl aqueous solutions with concentrations ranging from 1g/l to 35 g/l.**

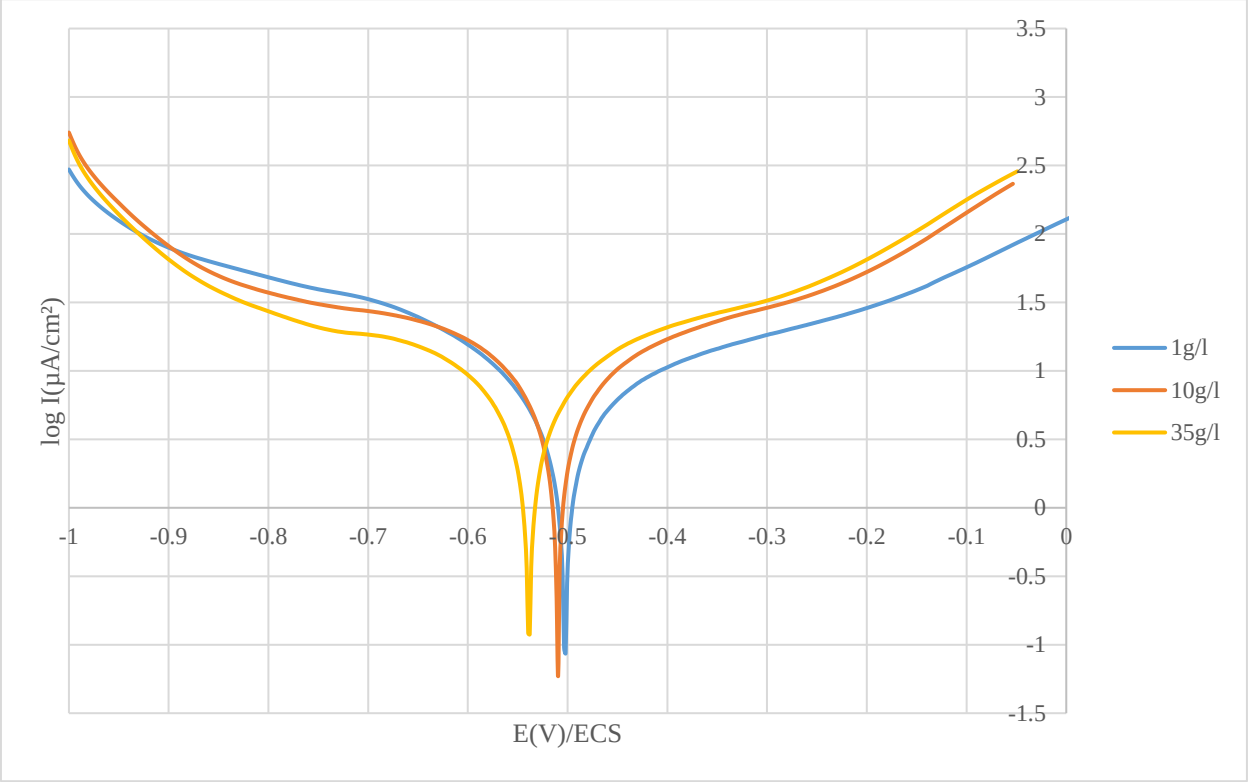


**Figure IV.14- Potentiodynamic polarization curves obtained after the immersion of coating in $Na_2SO_4$ aqueous solutions with concentrations ranging from 1g/l to 35 g/l.**

Each curve can be subdivided into two main domains: the cathodic domain that shows a descendant curve which is characterized by a straight Tafel line of negative slope, and the anodic domain that shows an upward curve which is characterized by a straight Tafel line of positive slope.

As listed in Table IV.4 and Table IV.5, corrosion current $I_{corr}$ increased gradually from the value 0.5898 µA/cm$^2$ in NaCl solution with 1g/l of concentration to reach a value of about 2.7680 µA/cm$^2$ when the concentration reached 35 g/l NaCl.

**Table IV.4-**Electrochemical parameters of NiFeCrBSi-WC coating in NaCl aqueous solution with different concentrations at ambient temperature.

| $C_{NaCl}\ (g/l)$ | 1 | 10 | 35 |
|---|---|---|---|
| $E_{corr}$(mV) | -433.7 | -497.0 | -523.3 |
| $I_{corr}(\mu A/cm^2)$ | 0.5898 | 2.5086 | 2.7680 |
| $V_{corr}$(µm/year) | 6.899 | 29.34 | 32.37 |

**Table IV.5-** Electrochemical parameters of NiFeCrBSi-WC coating in $Na_2SO_4$ aqueous solution with different concentrations at ambient temperature.

| $C_{Na2SO4}$ (g/l) | 1 | 10 | 35 |
|---|---|---|---|
| $E_{corr}$(mV) | -502.6 | -509.8 | -531.3 |
| $I_{corr}(\mu A/cm^2)$ | 1.6150 | 2.2581 | 2.2617 |
| $V_{corr}$(µm/year) | 18.88 | 26.41 | 26.45 |

In the case of $Na_2SO_4$, the corrosion current also increased from 1.6150 in 1g/l $Na_2SO_4$ to 2.2581 in 10g/l $Na_2SO_4$. Its value further rises continually with increasing the concentration of $Na_2SO_4$. It reaches 2.5972 µA/cm$^2$ and 2.2617 µA/cm$^2$ in 26g/l $Na_2SO_4$ and 35g/l $Na_2SO_4$ respectively.

Moreover, corrosion rate values increased with increasing the ion concentration in both NaCl and $Na_2SO_4$ solutions. The corrosion rate varies between 6.899 µm/y and 32.37 µm/y in NaCl solutions and is between 18.88 µm/y and 30.37 µm/y in $Na_2SO_4$ solutions. Additionally, corrosion potential values decreased from -433.7 mV to -523.3 mV with the increase of NaCl concentration. In $Na_2SO_4$ solutions, corrosion potential values range between -502.6 mV and -531.3 mV. The previous results suggest that the more the ion concentration is higher the more the corrosion potentials are negative. By examining the potentiodynamic polarization curves, it appears that the passivation domain doesn't exceed -200mV/ECS. When the concentration increases, the passivation domain shifts towards more negative potentials. The presence of WC

carbides makes the corrosion resistance better in NaCl and $Na_2SO_4$ than that in KOH alkaline environment if we compare the values with those obtained by Zeng et al [19]. However, a post-treatment with flame may be recommended to decrease the corrosion rate of coating by decreasing more the amount of porosity[20].

### IV.7.2 Electrochemical Impedance Spectroscopy

Figure 15 displays the Nyquist representations obtained after an EIS analysis of coating in various NaCl solutions. Each Nyquist plot shows a depressed capacitive semi-circle. This indicates that at the working electrode, there was adsorption of ions at the first moment of the tests. This adsorption gradually became worse when the passive layer began to form and the charge transfer is activated.

By comparing all the Nyquist plots in Figure 15, it results that the increase in ion concentration reduces the radius of the impedance semi-circles. This reduction is associated with the decrease of the charge transfer with increasing the chlorine ion concentration in the electrolyte. This is attributed to the gradual growth of the passive layer.

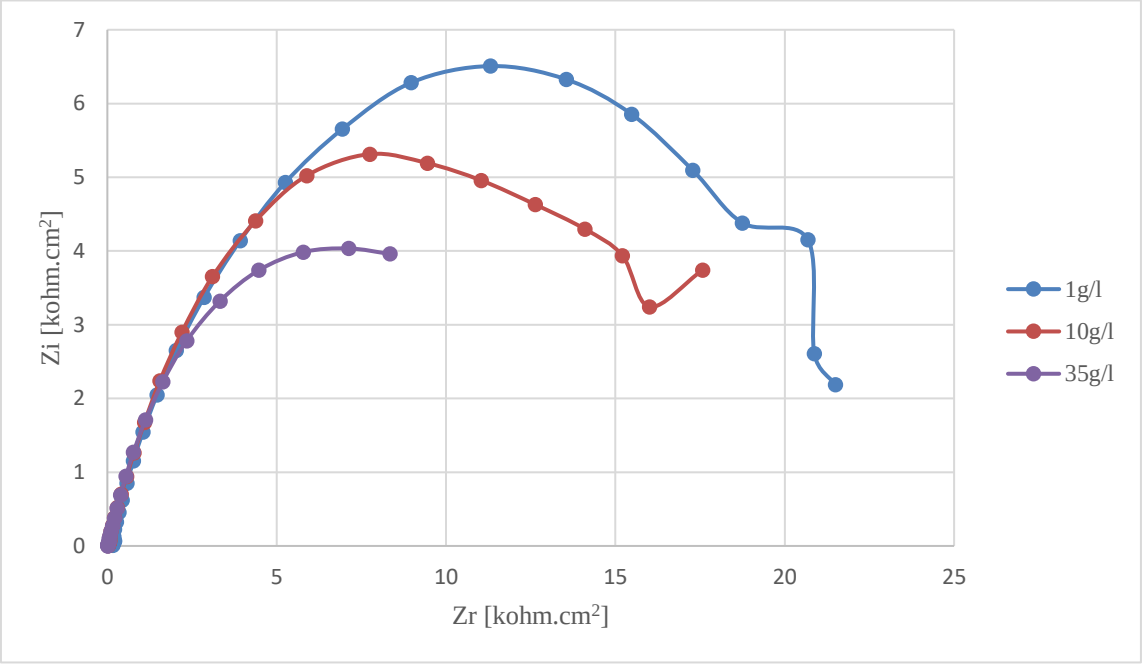


**Figure IV.15- EIS spectrum of coating immersed in NaCl aqueous solutions with concentration ranging from 1g/l to 35 g/l.**

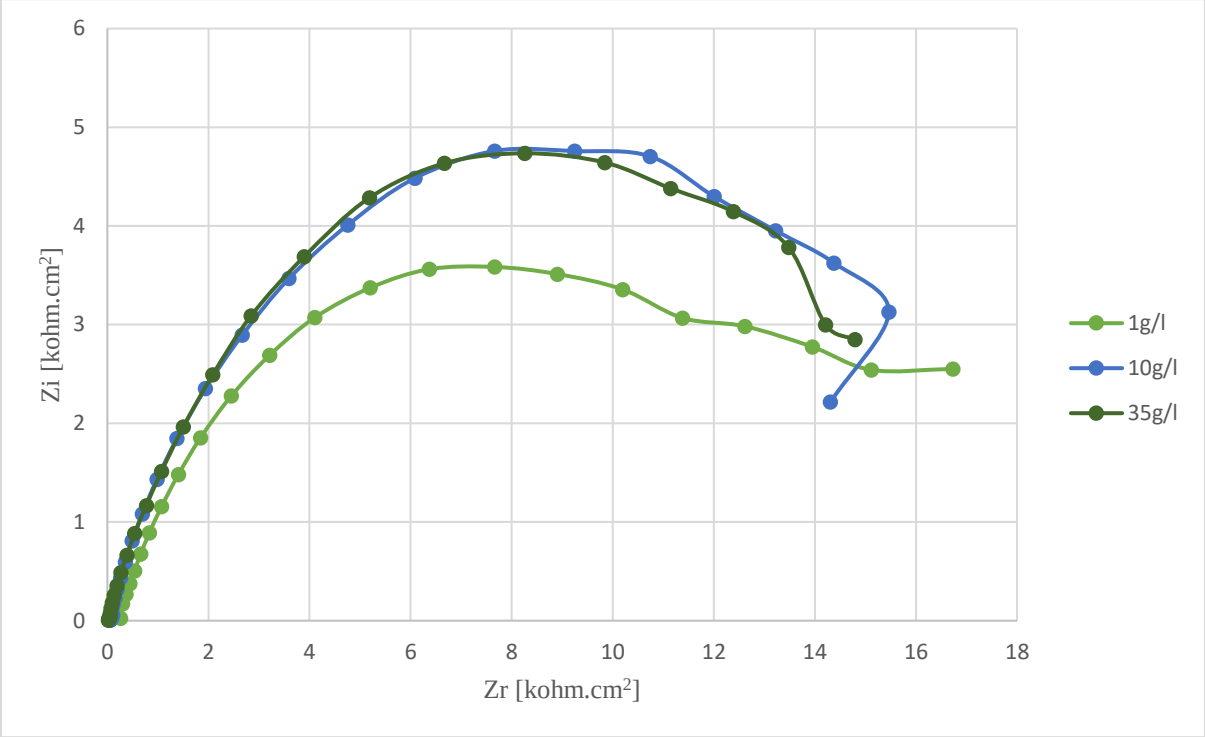


**Figure IV.16- EIS spectrum of coatings immersed in $Na_2SO_4$ aqueous solutions with concentration ranging from 1g/l to 35 g/l.**

As depicted in Figure 16, the increase of ion concentration induced an increase in the radius of the impedance semi-circles to a nearly constant value at concentrations above 1g/l of $Na_2SO_4$. This indicates that the passivation of coating at concentrations above 1g/l of $Na_2SO_4$ has occurred and therefore the coatings are protected against the aggressivity of $SO_4^{2-}$ ions through a compact passive layer.

## IV.8. Top Surface Characterization of Coating B

Figure 17 shows a 3D representation of the surface topography of the coating. The WC particles, in their unmelted state, are randomly distributed within the coating. They clearly appear in dark grey color and have the form of balls. Their presence makes the coating rough (8.23 µm) and the top surface wavier.

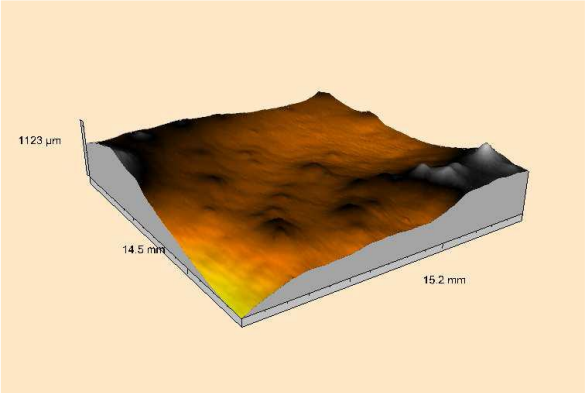


**Figure IV.17-3D rebuilding of the coating surface of coating B.**

Figure 18 shows the microstructure of a flame sprayed nickel-based composite coatings. The matrix of coating consists of two different nickel phases in which a white phase precipitate. One of the phases is dendritic. The coating matrix doesn't contain any amount of eutectic. Within the coating, the dendrites have a preferential orientation and were formed around the WC particles owing to an epitaxial nucleation. This specific orientation confirms the presence of residual stresses in the coating. The residual stresses are not very high as the coating adheres well to the substrate and cannot delaminate. The coating has certain amount of porosity and voids. These defects are characteristic of flame spraying process and are attributed to a gas entrapment. The voids and pores are present in the matrix with irregular shape. Some of them are spherical. They are distinguishable in the micrographs by their darkness. No unmelted particles or splat boundaries were observed and the coating is free of cracks. Indeed, the nickel self-fluxing matrix was subject to a post-heating by the spraying flame. The heat flux received by the sample reduces the residual stresses and eliminates the inter-splat boundaries. Moreover, the received heat flux make the solidification slow and that let the dendrites grow.

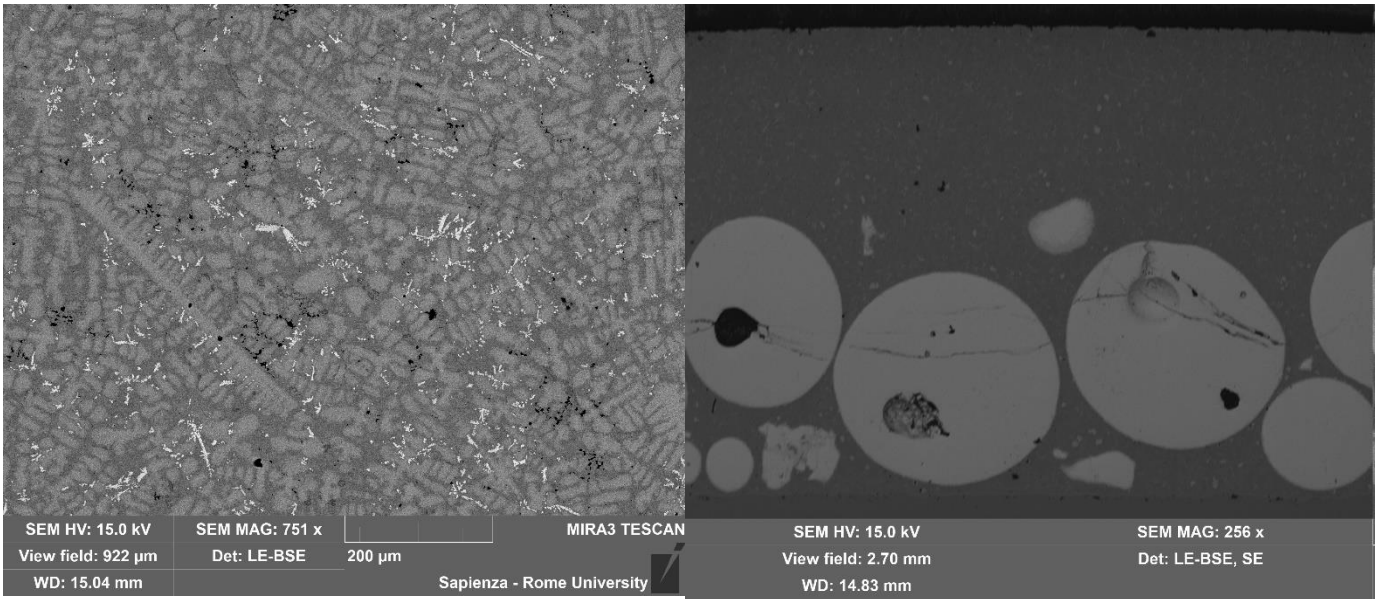


**Figure IV.18- Micrographs show on the left the microstructure of coating B and on the right show the microstructure of the cross section of coating B.**

## IV.9 SEM and EDS Analysis

The coating (Figure19, Figure 20, and Table IV.6) is composed of a matrix with a microstructure consisting of a dendritic phase ($Ni_3Fe$) and an interdendritic nickel-based phase. The chemical composition of the dendritic phase is different from the interdendritic nickel-based phase. The nickel phase which fills the interdendritic region is mainly composed of 90.44 % of nickel,5.04 % of carbon, 3% of chromium, and a few amounts of silicon (~0.01%) and tungestene (0.58%). it appears in dark gray while the other has a light gray color. The difference between the two phases lies in their content of alloying elements. The $Ni_3Fe$ phase (the light grey phase) is composed of 79.67% of nickel, 6.63% of chromium, 4.43% of carbon, 3.33% of tungsten, 3.22% of iron and 2.27 of silicon. This phase contains a little amount of oxygen (0.44%). Between these nickel-based phases, along the boundaries, there was no formation of precipitates, However, This matrix microstructure was a site of nucleation for the chromium carbides. Some of them has a floret-like structure. In its chemical composition, the chromium carbides contain particularly 40.98% of chromium, 21.89% of nickel, 22.44% of tungsten, 10.40% of carbon, and 3.25% of cobalt. The chromium carbides were initiated and then grew in the nickel phases. The formation of dendrites in this microstructure is attributed to a slow cooling rate. During the solidification, the nickel dendrites are the first to be formed. In the beginning, these dendrites are enriched with silicon and boron. With the cooling, these two chemical elements are rejected

to the interdendritic space due to their limited solubility in the dendrites at lower temperatures. When the nickel matrix is completely solidified, solid-state precipitation occurs through a diffusion-controlled process in the regions enriched in chromium to produce chromium carbides. As said before, the chromium carbides that result from this reaction are enriched with W. The absence of the eutectic in the microstructure is only due to the typical chemical composition of this composite and the kinetic of cooling.

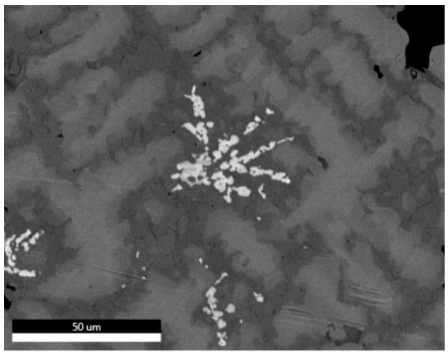


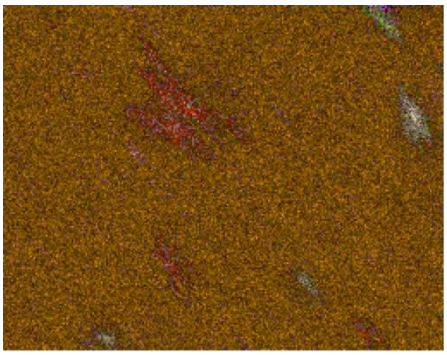


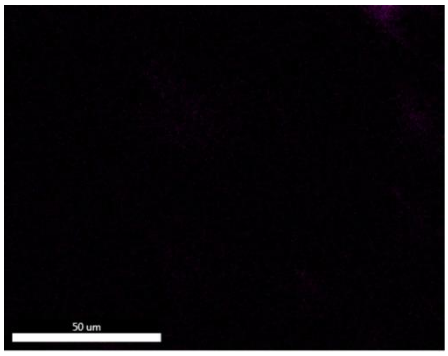


CK

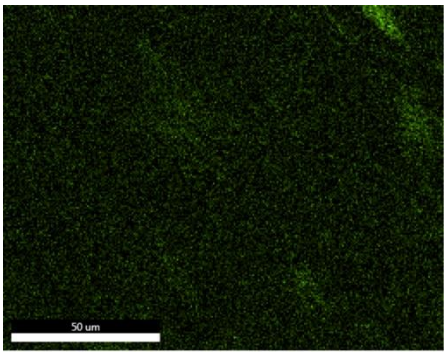


OK

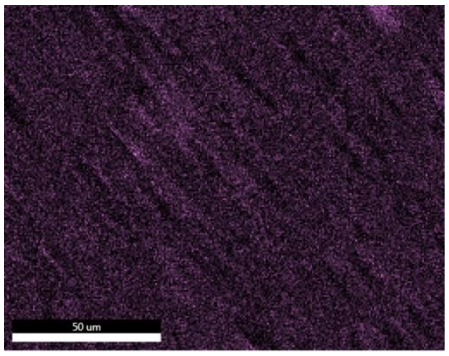


SiK

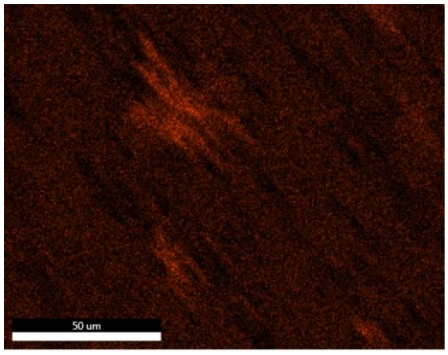


WM

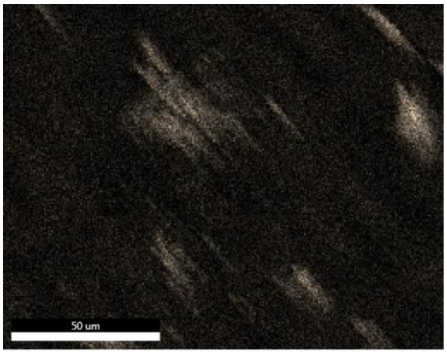


CrK

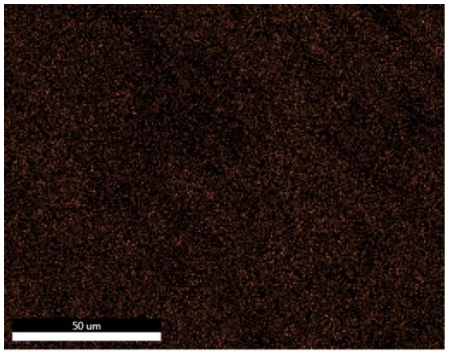


FeK

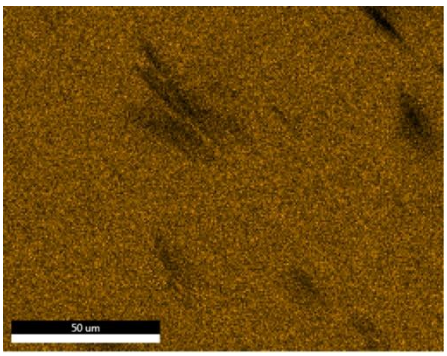


NiK

**Figure IV.19- Distribution of the chemical compounds within the coating matrix of coating B.**

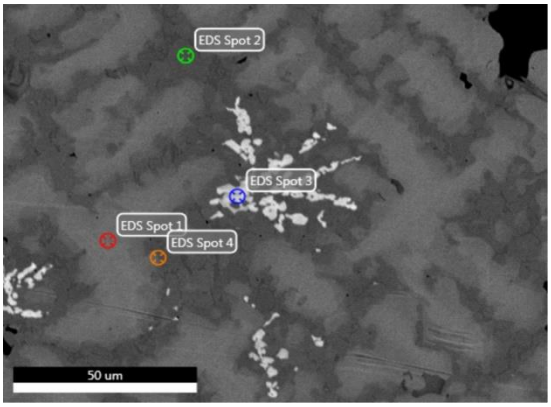


**Figure IV.20- The difference in the chemical composition between different phases present in the matrix.**

**Table IV.6-** The chemical composition of the analyzed spots.

| Element | | Ni | Fe | W | Cr | C | Si | O | Co |
|---|---|---|---|---|---|---|---|---|---|
| Spot 1 | (%Wt) | 79.67 | 3.22 | 3.33 | 6.63 | 4.43 | 2.27 | 0.44 | - |
| Spot 2 | (%Wt) | 90.44 | - | 0.58 | 3.00 | 5.04 | 0.01 | 0.93 | - |
| Spot 3 | (%Wt) | 21.89 | - | 22.44 | 40.98 | 10.40 | - | 1.04 | 3.25 |
| Spot 4 | (%Wt) | 90.65 | - | 0.99 | 2.89 | 4.42 | 1.05 | - | - |

During the processing, the WC carbides were subject to dissolution and decarburization to give $W_2C$ and the secondary precipitates around the WC particles (Figure 21). The presence of air facilitates this phenomenon especially if the WC has an irregular shape and small size. the chemistry of the matrix contributes to the acceleration of the dissolution. The tungsten has an affinity to diffuse to the matrix to form chromium tungsten carbides ($Cr_7W_3C_6$) [21]. Within the coating, the chromium tungsten carbides act as strengthening phase which induce an increasing of hardness and wear resistance. The $W_2C$ phase is present in its eutectic form along the interference with the matrix.

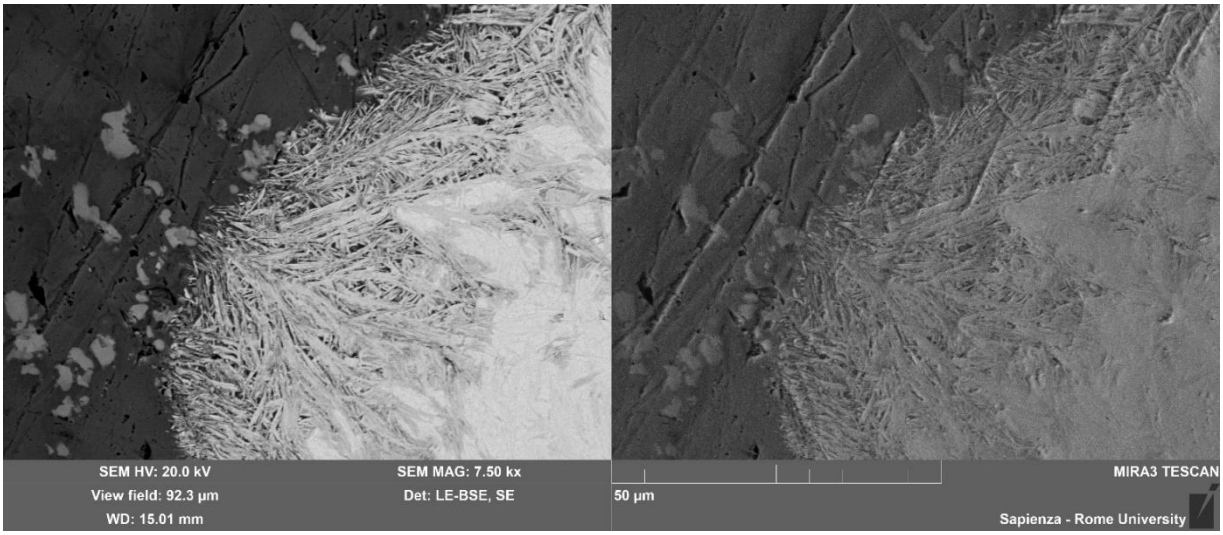


**Figure IV.21- Micrographs showing the dissolution of a WC particle.**

## IV.10 X-ray diffraction pattern Analysis

From a first view, the X-ray diffraction pattern of coating B (Figure 22) appears to be consisting of γ nickel solid solution along with $W_8Fe_{16}C_{168}H_{80}O_{64}$.WC while $W_2C$ and WC are present as strengthening phases. The chromium carbides could not be associated to any peak due to the overlap.

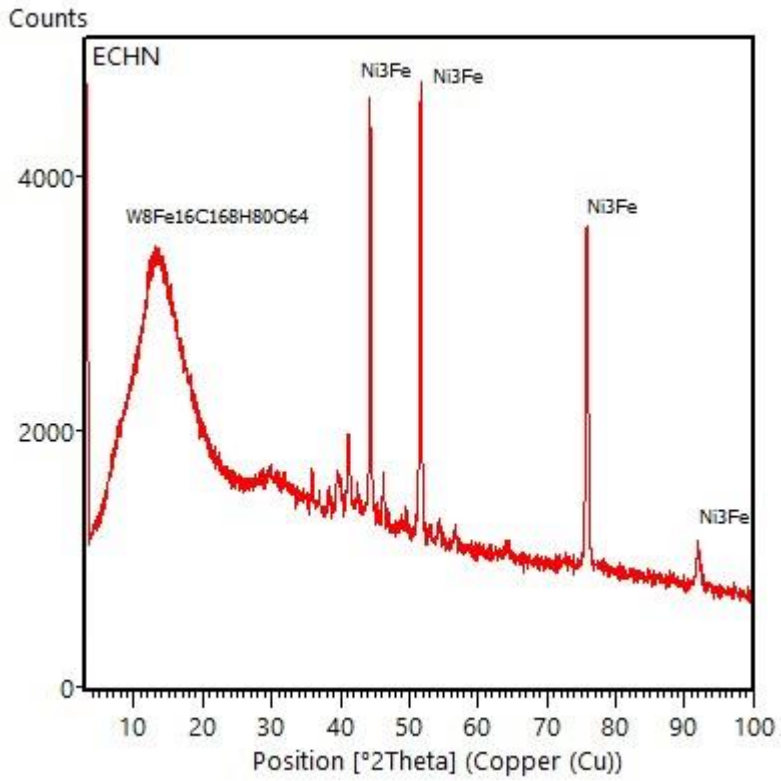


**Figure IV.22- XRD diffraction of coating B.**

## IV.11 Substrate/Coating B Interface Analysis

The Coating (Figure 23) is well bonded to the steel substrate. However, the porosity at the coating/substrate interface is minimal. The selected spraying parameters are adequate to not provoke the delamination and the cracking of the coating. The preheating treatment of the substates seems to be advantageous as it increases the adhesion of the bonding layer and the coatings. The preheating treatment also eliminates the stress between the substrate and the coatings.

At the interface between coating and the bounding layer, the EDS line scan (Figure 23) indicates that nickel diffused towards the substrate. This diffusion was high and conducted to depletion of nickel at the bottom of coating. Moreover, a peak of chromium was recorded near the steel substrate surface, which, indicates that a significant amount of chromium was diffused to the bottom of the bonding layer. However, it couldn't diffuse to the inside of the steel substrate as the substrate surface remains unmelted during the processing. The diffusion of chromium

depends on the diffusion coefficient of each chemical element that can be affected by the presence of carbides.

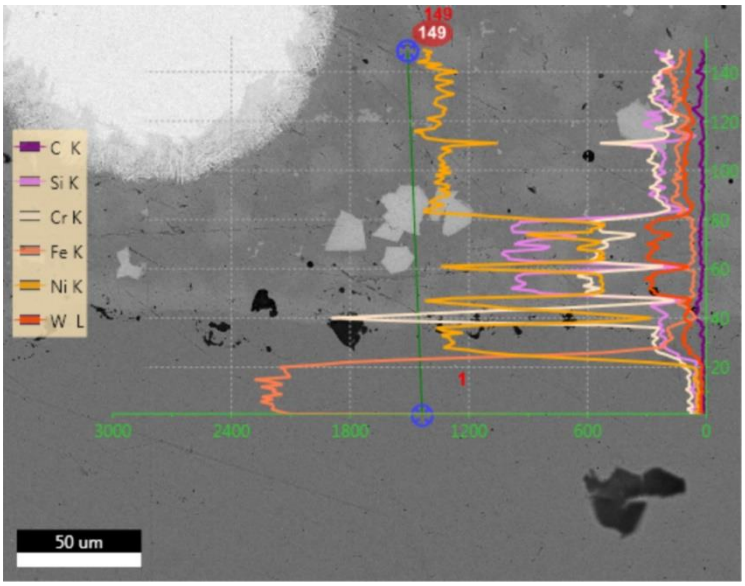


**Figure IV.23- EDS line scan shows the variance of the chemical composition starting from the substrate to the bottom of coating B.**

## IV.12. Mechanical Characterization of Coating B

### IV.12.1 Hardness Measurements

The hardness measurements were carried out on both the cross-section and the top surface of the coating under 100gf and 200gf. The results are illustrated in figures below. Our observation about the variance of hardness, during the test, are summarized in the following lines.

#### IV.12.1.1 Hardness of the substrate

The substrate hardness is equal to 450 HV under 100gf and 200gf. However, this value has a tendency to increase near the substrate/coating interface where the hardness reaches a maximum value of 730 HV. The higher value of hardness is attributed to the grit-blasting treatment which plastically deforms the surface by increasing its hardness by a strain-hardening.

#### IV.12.1.2 Hardness of coating matrix

Under an indentation normal force of 100gf, the matrix of coating exhibits a mean hardness value of about 443,14 (Figure 24). The maximum hardness value reached in the matrix is equal

to 669,7 HV. The WC carbides seem to be more brittle in several indented zones. They have a hardness that ranges from 1878 HV to 4410 HV with a mean value of 3026,6 HV. The voids and porosity-containing areas are characterized by a mean hardness of about 271,73 HV.

When increasing the value of the indentation charge to 200gf, the coating matrix takes a mean hardness around 402,11 HV. The hardness of WC carbides ranges from 1995 HV to 2786 HV with a mean value of 2428,4 HV. The voids and porosity-containing sites have a mean hardness of 288,3 HV.

### IV.12.1.3 Hardness of coating

The overall hardness of the composite under 100gf and 200gf (Figure 24) is 856,57 HV and 732,24 HV, respectively. These values are comparable with those reported in the literature even though the microstructures are not the same [22-25]. The decreasing of the overall hardness can be attributed to the lower density of WC and the presence of porous and decarburized zones in this type of coating.

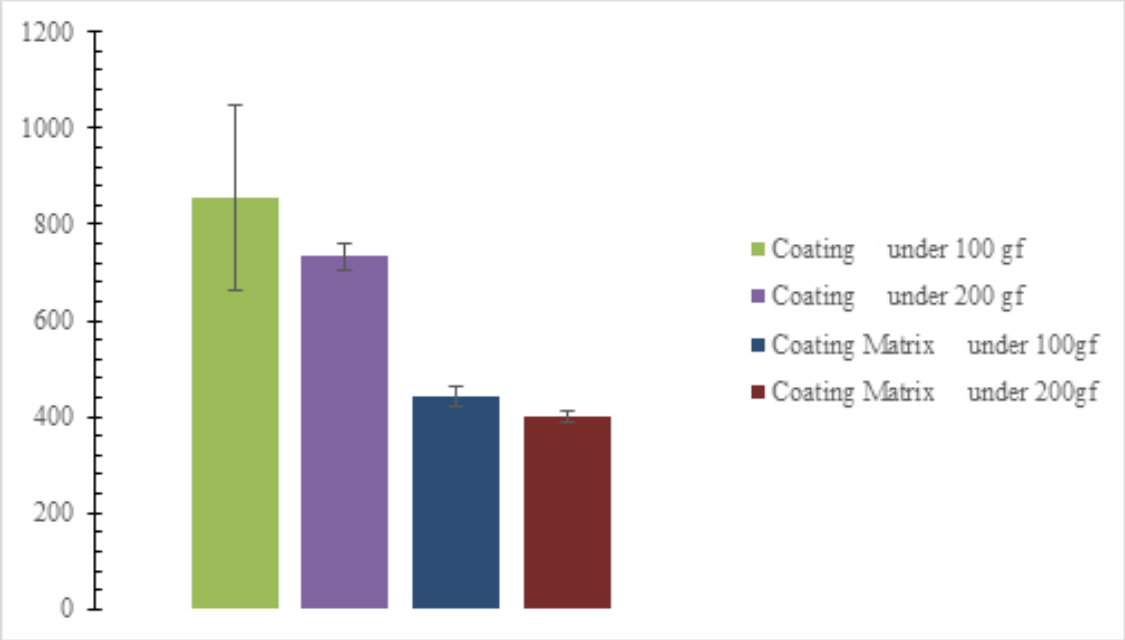


**Figure IV.24- Hardness of the coating and the coating matrix.**

### IV.12.1.4 Hardness of cross-section of coating

As depicted in Figure 25, the hardness of the cross section of coating increases from 474.49HV under 100gf to 496.25HV under 200gf. Despite the inhomogeneity of the coating,

the difference between the hardness values confirms that, from the cross section, the hardness depends on the distribution of WC and voids.

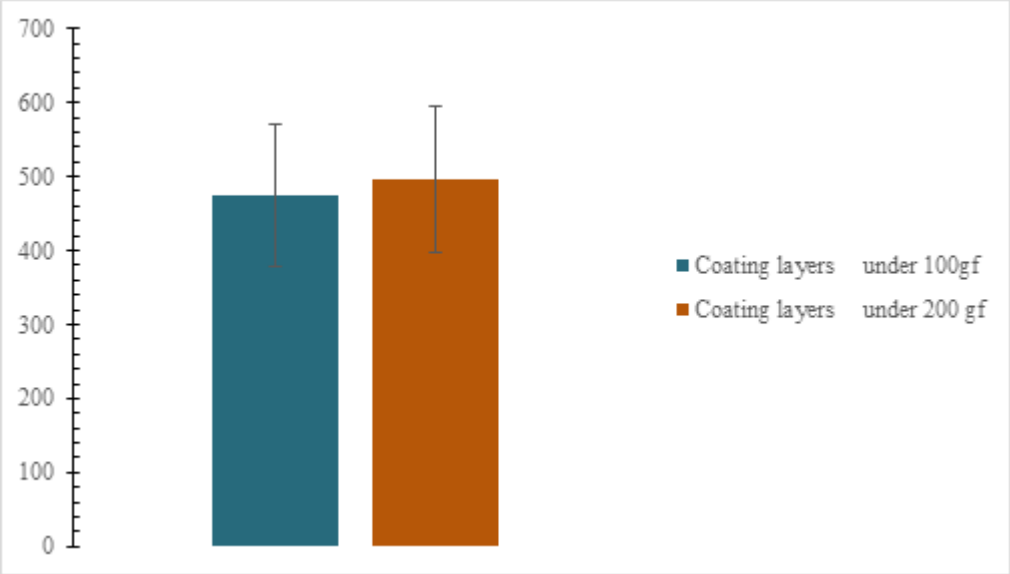


**Figure IV.25- Hardness of the cross section of coating.**

### IV.12.2. Microhardness Measurements of Coating B

The following figure illustrate the results of the microhardness measurement undergone on the cross section of coatings B. The results demonstrate the inhomogeneity of the coatings due to the presence of carbides. Even though the mean hardness of the matrix doesn't exceed 470 HV, the matrix is characterized by the presence of zones of carbides with relatively high hardness (500HV to 700 HV). During these tests, the indenter was not able to touch the WC carbides. However, the areas which surrounds the WC particles are characterized by high hardness (900 HV)

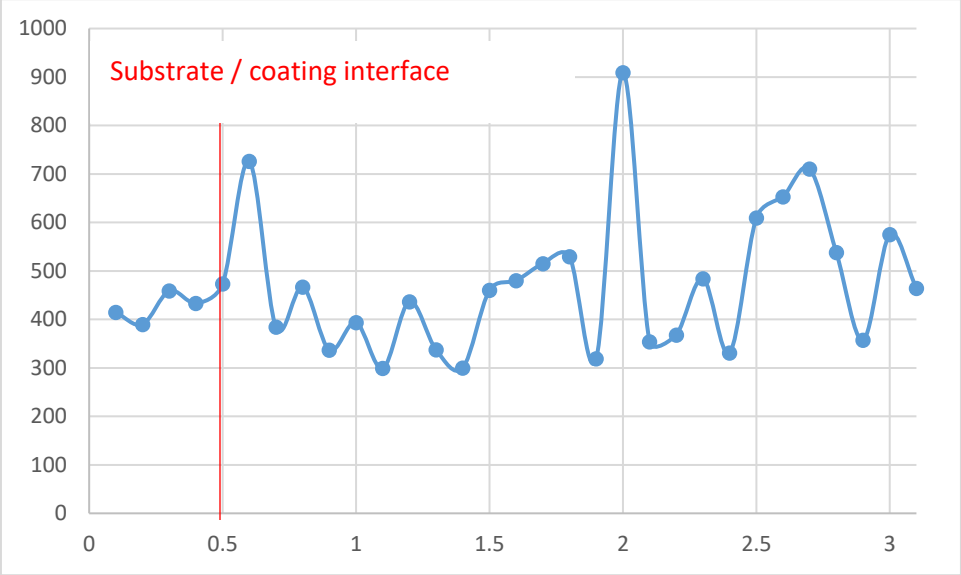


**Figure IV.26- Cross sectional micro-hardness evolution profile.**

### IV.12.3. Nanoindentation Measurements

Figure 27 presents the load displacement curves obtained after indenting the different phases present in the matrix of coating B. By analyzing these curves, it results that the chromium carbide is harder than the $\gamma$ nickel dendrites. The elastic modulus of the chromium carbide reaches a value of 118 GPa, while that of the $\gamma$ nickel dendrites achieves 124 GPa (Table IV.7). The more the phase is hard, the more the nanoindentation curve bends to the left. The areas, where porosity and voids are present, are characterized by the lower hardness (198HV) and elastic modulus (100 GPa). The extracted data from the unloading part of each graph were calculated and summarized in Table IV.8.

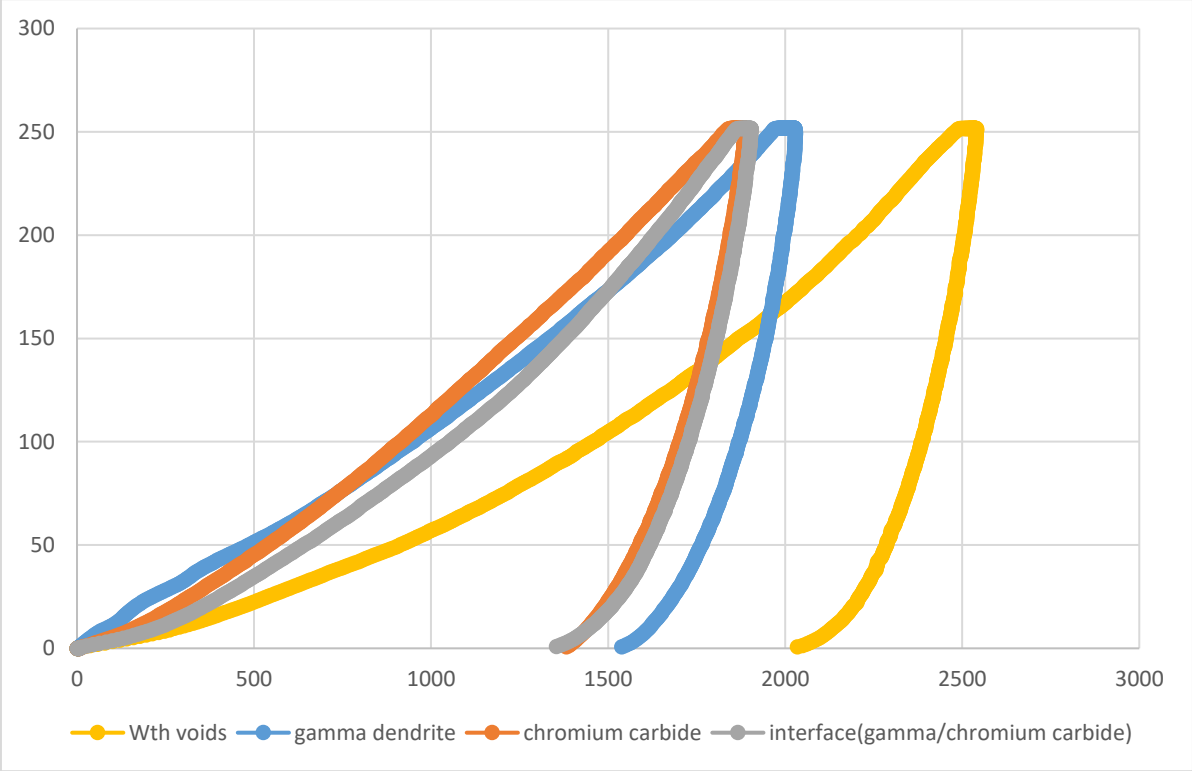


**Figure IV.27- Load–displacement (P–h) curves obtained during nano-indentation experiments carried out on the surface of coating B.**

**Table IV.7**-The obtained elastic moduli and hardness values after the nano-indentation tests.

| | E (GPa) | HV10 |
|---|---|---|
| With voids | 100.84 | 198.2 |
| $\gamma$ dendrite | 124.49 | 330.08 |
| Interface ($\gamma$/chromium carbide) | 126.03 | 385.56 |
| Chromium carbide | 118.15 | 399.55 |

**Table IV.8**-The characterizing depths of nano-indentation.

| | $h_m$(nm) | $h_{rc}$(nm) | $h_e$(nm) | $h_r$(nm) |
|---|---|---|---|---|
| With voids | 2539.25 | 2383.21 | 2072.85 | 2324.61 |
| $\gamma$ dendrite | 2027.14 | 1860.95 | 1562.91 | 1798.54 |
| Interface ($\gamma$/chromium carbide) | 1903.13 | 1725.47 | 1382.37 | 1658.76 |
| Chromium carbide | 1887.96 | 1695.67 | 1395.49 | 1624.27 |

## IV.13. Electrochemical Characterization of Coating B

### IV.13.1 Potentiodynamic Polarization

Figure 28 and Figure 29 represent the potentiodynamic polarization curves obtained after the immersion of coating in NaCl and $Na_2SO_4$ aqueous solutions, respectively, with concentrations ranging from 1g/l to 35 g/l.

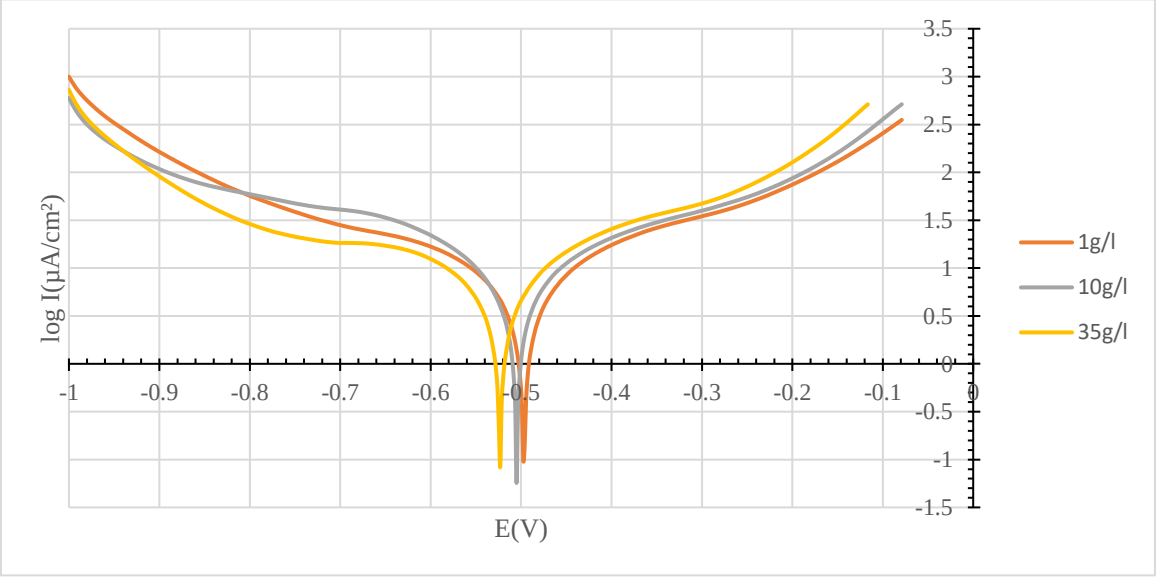


**Figure IV.28-Potentiodynamic polarization curves obtained after the immersion of coating in NaCl aqueous solutions with concentrations ranging from 1g/l to 35 g/l.**

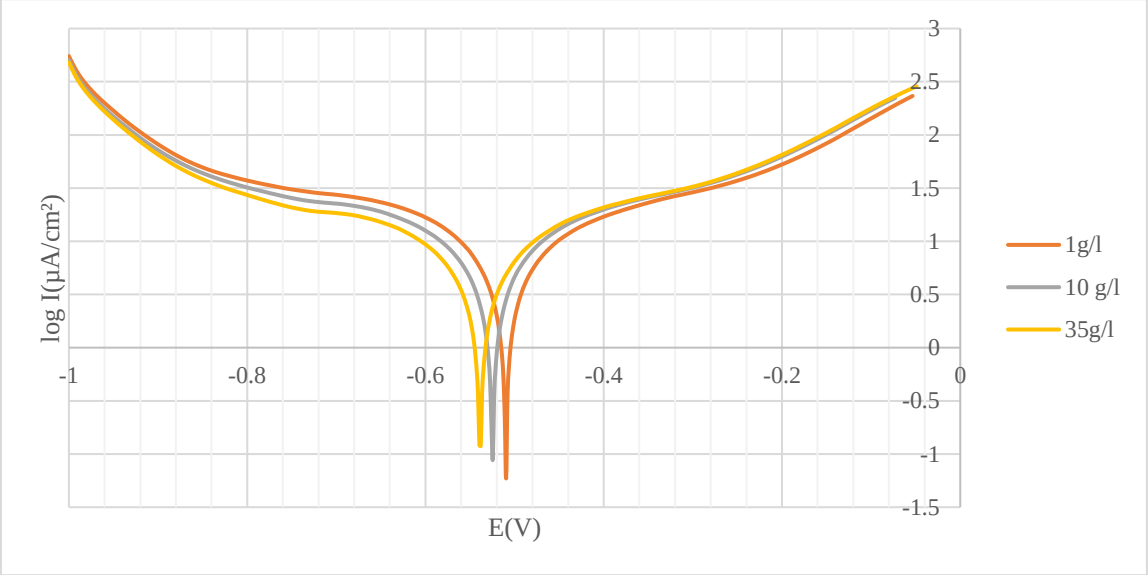


**Figure IV.29- Potentiodynamic polarization curves obtained after the immersion of coating in $Na_2SO_4$ aqueous solutions with concentrations ranging from 1g/l to 35 g/l.**

The extracted electrochemical data from the previous curves are summarized in Table IV.9 and Table IV.10. it's clear that the corrosion current $I_{corr}$ increased from the value 0.7471 µA/cm$^2$ in NaCl solution with 1g/l of concentration to attain a value of about 2.5970 µA/cm$^2$ when the concentration reached 35 g/l NaCl. The corrosion potential shift from –505 mV in NaCl solution with 1g/l of concentration toward the more negative values to reach -524.2 mV in NaCl solution with 35 g/l NaCl of concentration. The corrosion rate varies between 5.983 µm/year to 28.78 µm/year in this range of concentration.

In $Na_2SO_4$, the corrosion potential decreased from -509.5 mV at 1g/l of concentration to 524.5 mV at 10 g/l to reach a value of -539.5 mV. The corrosion current increased gradually and is between 1.3750 µA/cm$^2$ and 2.2501 µA/cm$^2$. In the given range of concentration, the corrosion rate increased gradually from 16.98 µm/year to 22.63 µm/year.

**Table IV.9-**Electrochemical parameters of NiFeCrBSi-WC coating in NaCl aqueous solution with different concentrations at ambient temperature.

| $C_{NaCl}\ (g/l)$ | 1 | 10 | 35 |
|---|---|---|---|
| $E_{corr}$(mV) | -505.0 | -506.1 | -524.2 |
| $I_{corr}(\mu A/cm^2)$ | 0.7471 | 2.1748 | 2.5970 |
| $V_{corr}$(µm/year) | 5.983 | 25.53 | 28.72 |

**Table IV.10-** Electrochemical parameters of NiFeCrBSi-WC coating in $Na_2SO_4$ aqueous solution with different concentrations at ambient temperature.

| $C_{Na2SO4}$ (g/l) | 1 | 10 | 35 |
|---|---|---|---|
| $E_{corr}$(mV) | -509.5 | -524.5 | -539.5 |
| $I_{corr}(\mu A/cm^2)$ | 1.3750 | 2.1378 | 2.2501 |
| $V_{corr}$(µm/year) | 16.98 | 20.30 | 22.63 |

### IV.13.2 Electrochemical Impedance Spectroscopy

Figure 30 displays the Nyquist representations obtained after an EIS analysis of coating in various NaCl solutions. Each Nyquist plot shows a depressed capacitive semi-circle, suggesting that there was adsorption of ions during the tests. This adsorption gradually became worse when the passive layer began to form and the charge transfer is activated.

By comparing all the Nyquist plots in Figure 30, it results that the increase in ion concentration reduces the radius of the impedance semi-circles. This reduction is ascribed to the decrease of the charge transfer with increasing the chlorine ion concentration in the electrolyte due to the gradual growth of the passive layer.

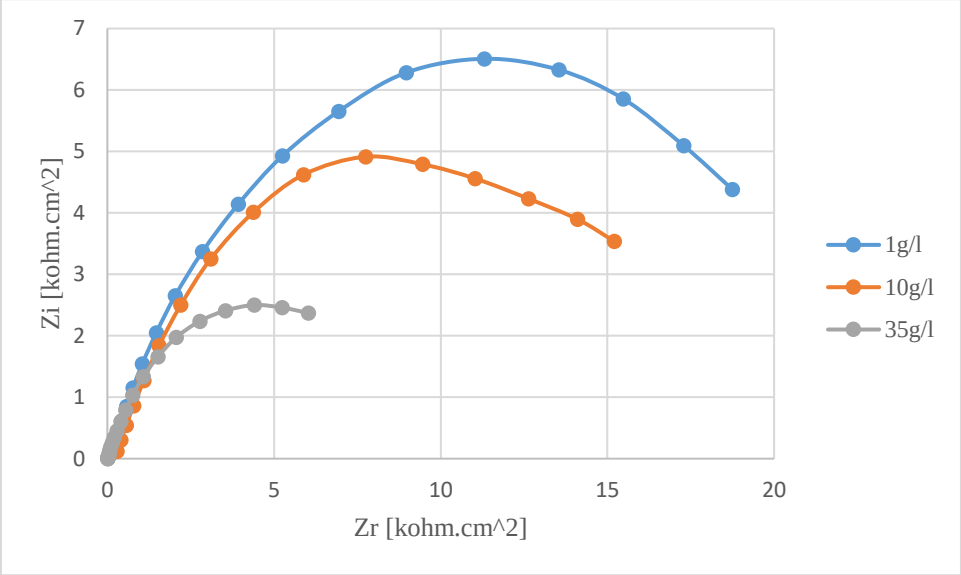


**Figure IV.30- EIS spectrum of coating immersed in NaCl aqueous solutions with concentration ranging from 1g/l to 35 g/l.**

As depicted in Figure 31, the increase of ion concentration induced an increase in the radius of the impedance semi-circles at concentrations above 1g/l of $Na_2SO_4$. This indicates that the passivation of coating at concentrations above 1g/l of $Na_2SO_4$ has occurred and therefore the coatings are protected against the aggressivity of $SO_4^{2-}$ ions through a compact passive layer.

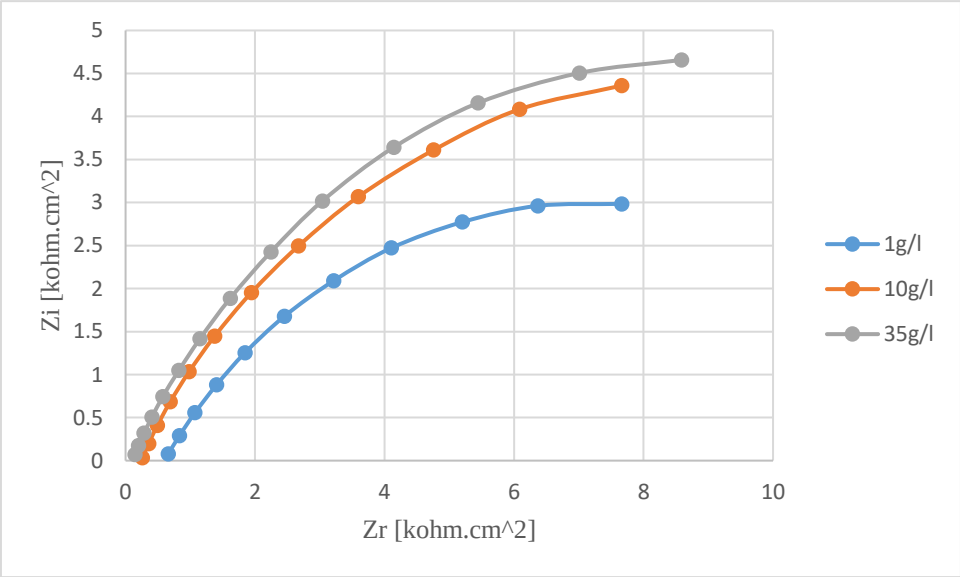


**Figure IV.31- EIS spectrum of coatings immersed in $Na_2SO_4$ aqueous solutions with concentration ranging from 1g/l to 35 g/l.**

# Conclusion

## Conclusion

In this thesis, two different NiFeCrBSi-WC, which will be used as coating for drilling bits, were characterized through profilometry, electronic microscopy, hardness, microhardness and nanoindentation measurements as well as potentiodynamic measurement and impedance spectroscopy.

we can infer that the obtained coating A is composed of nickel-based matrix reinforced with WC carbides. In this matrix, Ni-$\gamma$ is present in the form of dendrites. The coating contains further a eutectic phase ($\gamma$-$Cr_{2.4}W_{0.6}Si$) which fulfills the interdendritic space with chromium carbides ($Cr_{0.46}Ni_{0.31}W_{0.27}Fe_{0.08}$ C). The chromium carbides are present due to solid-state precipitation. The coating was thick and adherent and was subject to decarburization as the temperature of spraying was higher than 1200°C. The majority of WC carbides change their spherical shape. The presence of these carbides makes the hardness of the coating very high as compared with the coating matrix. The coating and its matrix resist better to the penetration when the indentation is performed on the top surface of the coating. This resistance refers to an elastoplastic response that differs depending on the present phases, voids, and oxides. For corrosion behavior, the increase in chlorine or sulfur ion concentration increases the corrosion rate. However, the increase in chloride ion concentration decreases the charge transfer at the coating/electrolyte interface. In $Na_2SO_4$ aqueous solutions, the coating forms a thin and compact passive layer that makes the charge transfer permanently constant at ion concentrations above 1g/l. Thus, the coating resist better in $Na_2SO_4$ than NaCl aqueous solutions. It could be used for offshore and onshore oil and gas fields.

From the present thesis, we can also infer that the coating matrix B is consisting of $Ni_3Fe$ ( ) dendrites and an interdendritic nickel rich phase. The coating matrix was subject to solid state precipitation which gives chromium carbides which contain in particular 40.98% of chromium, 21.89% of nickel, 22.44% of tungsten, 10.40% of carbon, and 3.25% of cobalt. Beside the tungsten carbides, near the interference with the matrix, the secondary chromium tungsten carbides ($Cr_7W_3C_6$) act as strengthening phases. These phases are a result of WC dissolution and decarburization. In the indented areas, the presence of carbides makes the hardness higher while the porosity drastically affect its value. The distribution of WC within the coating plays a significant role in increasing further the hardness of the composite. The hardness differs depending on the applied load and elasto-plastic response of the indented phases. For the

composite coating, it reaches 856,57 HV under 100gf and 732,24 HV under 200gf. The electrochemical behavior of coating B is similar to that of coating A. However, better corrosion resistance was observed due to the higher density of WC carbides.

As perspective, our results should be completed with tribological measurement via pin on disk and scratch test in order to evaluate the wear behavior of the coatings. The use of coatings for a working cycle will allow and lead to the determination of the prominent mechanisms arisen before their failure. An evaluation of the residual stresses and the adherence is recommended to complement the results.

# Bibliography

# Bibliography

## Chapter I


**[1]. Manhar R. Dhanak, Nikolaos I. Xiros. Springer Handbook of Ocean Engineering. Springer (2016) ISBN: 978-319-16648-3**

**[2]. Urbina, M., et al., The methodologies and strategies for the development of novel material systems and coatings for applications in extreme environments − a critical review. Manufacturing Rev., 2018. 5: p. 9.**

**[3]. Cartier, M. and E. American Society of Mechanical, Handbook of surface treatments and coatings. 2003, New York, NY; Bury St. Edmunds, Suffolk, UK: ASME Press ; Professional Engineering Pub.**

**[4]. Espallargas, N., 1 - Introduction to thermal spray coatings, in Future Development of Thermal Spray Coatings, N. Espallargas, Editor. 2015, Woodhead Publishing. p. 1-13.**

**[5]. DAVIS, Joseph R., et al. (ed.). Handbook of thermal spray technology. ASM international, 2004.**

**[6] American Welding Society Thermal spraying, practice, theory and application. (1985), American Welding Society, Miami, FL**

**[7] Pawlowski L. The science and engineering of thermal spray coatings. Wiley, New York, NY, 1st edition (1995).**

**[8] Pawlowski, L., The science and engineering of thermal spray coatings. 2008: John Wiley & Sons.**

**[9] Fauchais, P.L., J.V.R. Heberlein, and M.I. Boulos, Introduction, in Thermal Spray Fundamentals: From Powder to Part. 2014, Springer US: Boston, MA. p. 1-15.**

**[10] Schneider, K.E., et al., Thermal spraying for power generation components. 2006: John Wiley & Sons.**

**[11]. Ružbarský, J. and A. Panda, Thermal Spraying, in Plasma and Thermal Spraying. 2017, Springer. p. 49-57.**

**[12] Fauchais, P. and A. Vardelle, Thermal sprayed coatings used against corrosion and corrosive wear, in Advanced plasma spray applications. 2012, InTech.**

**[13] Kadyrov, E. and V. Kadyrov, Gas dynamical parameters of detonation powder spraying. Journal of Thermal Spray Technology, 1995. 4(3): p. 280-286.**

**[14] Fauchais, P., 2 - Current status and future directions of thermal spray coatings and techniques, in Future Development of Thermal Spray Coatings, N. Espallargas, Editor. 2015, Woodhead Publishing. p. 17-49.**

**[15] Fagoaga, I., Barykin, G., De Juan, J., Soroa, T., Vaquero, C., Coatings, A., Inasmet, F., The high frequency pulse detonation (HFPD) spray process. In: Thermal Spray 1999: United Thermal Spray Conference (DVS-ASM), pp. 282–287.**

**[16] Browning, J.A., Hypervelocity impact fusion—a technical note. Journal of Thermal Spray Technology, 1992. 1(4): p. 289-292.**

**[17] Dykhuizen, R.C. and M.F. Smith, Gas dynamic principles of cold spray. Journal of Thermal Spray Technology, 1998. 7(2): p. 205-212.**

**[18] Moreau, C., P. Gougeon, and M. Lamontagne, Influence of substrate preparation on the flattening and cooling of plasma-sprayed particles. Journal of Thermal Spray Technology, 1995. 4(1): p. 25-33.**

**[19] Gawne, D.T., B.J. Griffiths, and G. Dong, The Influence of Pretreatment on the Adhesion of Ceramic Coatings on Steel. Transactions of the IMF, 1997. 75(6): p. 205-207.**

**[20] Sampath, S., et al., Substrate temperature effects on splat formation, microstructure development and properties of plasma sprayed coatings Part I: Case study for partially stabilized zirconia. Materials Science and Engineering: A, 1999. 272(1): p. 181-188.**

**[21] Jiang, X., J. Matejicek, and S. Sampath, Substrate temperature effects on the splat formation, microstructure development and properties of plasma sprayed coatings: Part II: case study for molybdenum. Materials Science and Engineering: A, 1999. 272(1): p. 189-198.**

**[22] Collings, E.W., et al., Splat-quench solidification of freely falling liquid-metal drops by impact on a planar substrate. Journal of Materials Science, 1990. 25(8): p. 3677-3682.**

**[23] C. Robert, A Vardelle, G.X. Wang, X.Y.Jiang, S. Sampaph, Microstructure development during plasma spraying of molybdenum Part I : Splat solidification proceedings of the 15th International Thermal Spray Conference, Vol.1, Edited by Christian Codett, Nice, France, 1998, p.729.**

**[24] Dykhuizen, R.C., Review of impact and solidification of molten thermal spray droplets. Journal of Thermal Spray Technology, 1994. 3(4): p. 351-361.**

**[25] Fauchais, P., et al., Knowledge concerning splat formation: An invited review. Journal of Thermal Spray Technology, 2004. 13(3): p. 337-360.**

**[26] Chandra, S. and P. Fauchais, Formation of Solid Splats During Thermal Spray Deposition. Journal of Thermal Spray Technology, 2009. 18(2): p. 148-180.**

**[27] Fukumoto M, Haang Y Flattening mechanism in thermal sprayed Ni particles impinging on flat substrate. Journal Thermal Spray Technology, 1999. 8(2): p. 427–432.**

**[28] Sokolov, D., Contribution to the development of thermal spraying at very low pressure. 2009, Université de Technologie de Belfort-Montbeliard.**

**[29] Bolot, R., et al., A three-dimensional model of the wire-arc spray process and its experimental validation. Journal of Materials Processing Technology, 2008. 200(1): p. 94-105.**

**[30] Seyed A., Co-spraying of alumina and stainless steel by d.c. plasma jets. PhD Thesis, University of Limoges France and GIK Institute, Topi, Pakistan, 26 Feb 2004, Limoges France**

**[32] Fauchais, P.L., J.V. Heberlein, and M.I. Boulos, Overview of Thermal Spray, in Thermal Spray Fundamentals. 2014, Springer. p. 17-72.**

**[33]. Barradas, S., Etude, à l'aide du choc laser, des mécanismes d'adhérence aux interfaces cuivre/aluminium et cuivre/cuivre obtenues par projection thermique. 2004, École Nationale Supérieure des Mines de Paris.**

**[34]. Darque-Ceretti, E. and E. Felder, Adhésion et Adhérence. 2003: CNRS Editions. 388 pages - ISBN : 978-2-271-06092-1.**

**[35]. Blanchi, L., et al., Comparison of plasma-sprayed alumina coatings by RF and DC plasma spraying. Journal of Thermal Spray Technology, 1995. 4(1): p. 59-66.**

**[36]. Mellali Mohamed, Influence de la rugosité et de la température de surface du substrat sur l'adhérence et les contraintes résiduelles au sein de dépôts d'alumine projetés par plasma, thèse de doctorat, Limoges, Université de Limoges, 1994. p,292.**

**[37]. Bianchi, L., et al., Splat formation and cooling of plasma-sprayed zirconia. Thin Solid Films, 1997. 305(1): p. 35-47.**

**[38]. Patru J. Modélisation du développement des contraintes résiduelles au sein de dépôts plasma de zircone et d'acier [En ligne]. Thèse de doctorat : Matériaux Céramiques et Traitements de Surface. Limoges : Université de Limoges, 2005**

**[39]. Moreau, C., P. Gougeon, and M. Lamontagne, Influence of substrate preparation on the flattening and cooling of plasma-sprayed particles. Journal of Thermal Spray Technology, 1995. 4(1): p. 25-33.**

**[40]. Cedelle, J., M. Vardelle, and P. Fauchais, Influence of stainless steel substrate preheating on surface topography and on millimeter- and micrometer-sized splat formation. Surface and Coatings Technology, 2006. 201(3): p. 1373-1382.**

**[41]. Vandellos, T., Développement d'une stratégie de modélisation du délaminage dans les structures composites stratifiées. Thèse de doctorat, Université de Bordeaux 1, 2011.**

**[42]. Clyne, T.W., Residual Stresses in Coated and Layered Systems, in Encyclopedia of Materials: Science and Technology, K.H.J. Buschow, et al., Editors. 2001, Elsevier: Oxford. p. 8126-8134.**

**[43]. Arif, A.F.M., K.S. Al-Athel, and J. Mostaghimi, 3.4 Residual Stresses in Thermal Spray Coating, in Comprehensive Materials Finishing, M.S.J. Hashmi, Editor. 2017, Elsevier: Oxford. p. 56-70.**

**[44]. Tchoquessi-Diodjo, M.R., Tchoquessi Diodjo, Improving adhesion of thick coatings on steel : experimental and numerical study. 2013, Université de Toulon.**

**[45]. Mellali, M., P. Fauchais, and A. Grimaud, Influence of substrate roughness and temperature on the adhesion/cohesion of alumina coatings. Surface and Coatings Technology, 1996. 81(2): p. 275-286.**

**[46]. Khante, S.N. and N. Jain. Erosion Identification and Assessment of a Steel Pipeline Using EMI Technique. 2019. Singapore: Springer Singapore.**

**[47]. Holmberg, K. and A. Erdemir, Influence of tribology on global energy consumption, costs and emissions. Friction, 2017. 5(3): p. 263-284.**

**[48]. Dong, H., 3 - Tribological properties of titanium-based alloys, in Surface Engineering of Light Alloys, H. Dong, Editor. 2010, Woodhead Publishing. p. 58-80.**

**[49]. Roy, M., 6 - Tribological degradation at elevated temperature, in Developments in High Temperature Corrosion and Protection of Materials, W. Gao and Z. Li, Editors. 2008, Woodhead Publishing. p. 117-163.**

**[50]. Moore, M.A., A review of two-body abrasive wear. Wear, 1974. 27(1): p. 1-17.**

**[51]. Hokkirigawa, K. and K. Kato, An experimental and theoretical investigation of ploughing, cutting and wedge formation during abrasive wear. Tribology International, 1988. 21(1): p. 51-57.**

**[52]. Bhushan, B., Modern tribology handbook, two volume set. 2000: CRC press.**

**[53]. Bhushan, B., Introduction to tribology. 2013: John Wiley & Sons.**

**[54]. Bayer, R.G., Mechanical Wear Fundamentals and Testing, revised and expanded. 2004: CRC Press.**

**[55]. Kandeva-Ivanova, M., A. Vencl, and D. Karastoyanov, Advanced Tribological Coatings for Heavy-Duty Applications: Case Studies. 2016: Bulgarian Academy of Sciences, Institute of Information and Communication Technologies; Prof. Marin Drinov Publishing House of Bulgarian Academy of Sciences.**

**[56]. Mohanty, R.M. and M. Roy, 5 - Thermal sprayed WC-Co coatings for tribological application, in Materials and Surface Engineering, J. Paulo Davim, Editor. 2012, Woodhead Publishing. p. 121-162.**

**[57]. Gruner, H., Vacuum plasma spray quality control. Thin Solid Films, 1984. 118(4): p. 409-420.**

**[58]. Henne, R., W. Schnurnberger, and W. Weber, Low pressure plasma spraying-properties and potential for manufacturing improved electrolysers. Thin Solid Films, 1984. 119(2): p. 141-152.**

**[59]. J. Stokes, The Theory and Application of the HVOF Thermal Spray Process, Dublin City University, Dublin (2005).**

**[60]. V. V. Sobolev, J. M. Guilemany, and J. Nutting, HVOF Spraying, B0655, Maney, IOM3 (2004).**

**[61]. Kudinov V., Pekshev P., Belaschenko B., Solonenko O., Safiulin V., " Coating spraying by plasma", in russian, Moscou, "Nauka", 1990, p 401**

**[62]. Gale, B.K., et al., Low-Cost MEMS Technologies, in Reference Module in Materials Science and Materials Engineering. 2016, Elsevier.**

## Chapter II

**[1]. Reinaldo, P.R. and A.S.C.M. D'Oliveira, *NiCrSiB Coatings Deposited by Plasma Transferred Arc on Different Steel Substrates.* Journal of Materials Engineering and Performance, 2013. 22(2): p. 590-597.**

**[2]. Gil, L., et al., *Microstructural characterisation of NiWCrBSiC alloy coating produced by HVOF thermal spraying.* Surface Engineering, 2006. 22(4): p. 304-313.**

**[3]. Hemmati, I., et al., *Microstructure and Phase Formation in a Rapidly Solidified Laser-Deposited Ni-Cr-B-Si-C Hardfacing Alloy.* Metallurgical and Materials Transactions A, 2014. 45(2): p. 878-892.**

**[4]. Rodríguez, M.A., L. Gil, and M.H. Staia, *Post-Heat Microstructural Treatment Changes in Nickel Based Hvof Coating.* Surface Engineering, 2002. 18(5): p. 358-362.**

**[5]. Tokarev, A.O., *Treatment of Wear-Resistant Metallic Coatings with Highly Concentrated Energy Sources.* Metal Science and Heat Treatment, 2001. 43(1): p. 61-64.**

**[6]. Serres, N., et al.,** ***Microstructures of Metallic NiCrBSi Coatings Manufactured via Hybrid Plasma Spray and In Situ Laser Remelting Process.*** **Journal of Thermal Spray Technology, 2011. 20(1): p. 336-343.**

**[7]. Zhang, Y.M., et al.,** ***Influence of WC addition on microstructures of laser-melted Ni-based alloy coating.*** **Journal of Materials Engineering and Performance, 2002. 11(6): p. 667-674.**

**[8]. Zhang, Y.M., et al.,** ***Effect of WC addition on microstructures of laser melted Ni-based alloy powder.*** **Surface and Coatings Technology, 2003. 169-170: p. 384-387.**

**[9]. Liyanage, T., G. Fisher, and A.P. Gerlich,** ***Influence of alloy chemistry on microstructure and properties in NiCrBSi overlay coatings deposited by plasma transferred arc welding (PTAW).*** **Surface and Coatings Technology, 2010. 205(3): p. 759-765.**

**[10]. Sudha, C., et al.,** ***Microchemical and microstructural studies in a PTA weld overlay of Ni–Cr–Si–B alloy on AISI 304L stainless steel.*** **Surface and Coatings Technology, 2008. 202(10): p. 2103-2112.**

**[11]. Sidhu, T.S., S. Prakash, and R.D. Agrawal,** ***Performance of high-velocity oxyfuel-sprayed coatings on an fe-based superalloy in Na2SO4-60%V2O5 environment at 900 °C Part I: Characterization of the coatings.*** **Journal of Materials Engineering and Performance, 2006. 15(1): p. 122-129.**

**[12]. Otsubo, F., H. Era, and K. Kishitake,** ***Interface reaction between nickel-base self-fluxing alloy coating and steel substrate.*** **Journal of Thermal Spray Technology, 2000. 9(2): p. 259-263.**

**[13]. Šimunović, K., I. Kladarić, and D. Krumes,** ***Investigation of substrate microstructure after flame spraying and fusing.*** **Strojarstvo: časopis za teoriju i praksu u strojarstvu, 2008. 50(4): p. 213-220.**

**[14]. Skulev, H., et al.,** ***Microstructural and mechanical properties of nickel-base plasma sprayed coatings on steel and cast iron substrates.*** **Surface and Coatings Technology, 2005. 197(2): p. 177-184.**

**[15]. La Barbera-Sosa, J.G., et al.,** ***Effect of spraying distance on the microstructure and mechanical properties of a Colmonoy 88 alloy deposited by HVOF thermal spraying.*** **Surface and Coatings Technology, 2010. 205(7): p. 1799-1806.**

**[16]. Zeng, Z., et al.,** ***Effects of Some Light Alloying Elements on the Oxidation Behavior of Fe and Ni-Cr Based Alloys During Air Plasma Spraying.*** **Journal of Thermal Spray Technology, 2010. 19(1): p. 128-136.**

**[17]. Zeng, Z., S. Kuroda, and H. Era,** ***Comparison of oxidation behavior of Ni–20Cr alloy and Ni-base self-fluxing alloy during air plasma spraying.*** **Surface and Coatings Technology, 2009. 204(1): p. 69-77.**

**[18]. Zhang, X.C., et al.,** ***Porosity and effective mechanical properties of plasma-sprayed Ni-based alloy coatings.*** **Applied Surface Science, 2009. 255(8): p. 4362-4371.**

**[19]. Zhang, X.C., et al.,** ***Porosity, mechanical properties, residual stresses of supersonic plasma-sprayed Ni-based alloy coatings prepared at different powder feed rates.*** **Applied Surface Science, 2008. 254(13): p. 3879-3889.**

**[20]. Zhang, X.C., et al.,** ***Statistical analyses of porosity variations in plasma-sprayed Ni-based coatings.*** **Journal of Alloys and Compounds, 2009. 467(1): p. 501-508.**

**[21]. Zhang, X.C., et al.,** ***Microstructural and porosity variations in the plasma-sprayed Ni-alloy coatings prepared at different spraying powers.*** **Journal of Alloys and Compounds, 2009. 473(1): p. 145-151.**

**[22]. Li, C.-J. and Y.-Y. Wang,** ***Effect of particle state on the adhesive strength of HVOF sprayed metallic coating.*** **Journal of Thermal Spray Technology, 2002. 11(4): p. 523-529.**

**[23]. Wang, Y.Y., C.J. Li, and A. Ohmori,** ***Examination of factors influencing the bond strength of high velocity oxy-fuel sprayed coatings.*** **Surface and Coatings Technology, 2006. 200(9): p. 2923-2928.**

**[24]. Wang, Y.Y., C.J. Li, and A. Ohmori,** ***Influence of substrate roughness on the bonding mechanisms of high velocity oxy-fuel sprayed coatings.*** **Thin Solid Films, 2005. 485(1): p. 141-147.**

**[25]. Dolgov, N.A.,** ***Method for Determining the Modulus of Elasticity for Gas Thermal Spray Coatings.*** **Powder Metallurgy and Metal Ceramics, 2004. 43(7): p. 423-428.**

**[26]. Tsui, Y.C. and T.W. Clyne,** ***An analytical model for predicting residual stresses in progressively deposited coatings Part 1: Planar geometry.*** **Thin Solid Films, 1997. 306(1): p. 23-33.**

**[27]. Tsui, Y.C. and T.W. Clyne,** ***An analytical model for predicting residual stresses in progressively deposited coatings Part 2: Cylindrical geometry.*** **Thin Solid Films, 1997. 306(1): p. 34-51.**

**[28]. Zhang, Z., Z. Wang, and B. Liang,** ***Microstructure and Dry-Sliding Wear Behavior of Thermal Sprayed and Fused Ni-Based Coatings with the Addition of La2O3.*** **Tribology Letters, 2010. 37(2): p. 141-148.**

**[29]. Chen, H., et al.,** ***Sliding wear behaviour of laser clad coatings based upon a nickel-based self-fluxing alloy co-deposited with conventional and nanostructured tungsten carbide–cobalt hardmetals.*** **Wear, 2005. 259(7): p. 801-806.**

**[30]. Chen, H., et al.,** ***Microstructure and phase transformation of WC/Ni60B laser cladding coatings during dry sliding wear.*** **Wear, 2008. 264(7): p. 487-493.**

**[31]. García, A., et al.,** ***Tribological effects of the geometrical properties of plasma spray coatings partially melted by laser.*** **Wear, 2013. 305(1): p. 1-7.**

**[32]. Serres, N., et al.,** ***Microstructures and mechanical properties of metallic NiCrBSi and composite NiCrBSi–WC layers manufactured via hybrid plasma/laser process.*** **Applied Surface Science, 2011. 257(12): p. 5132-5137.**

**[33]. Parthasarathi, N.L. and M. Duraiselvam,** ***High temperature tribological properties of NiCrBSiCFe plasma-sprayed coating on austenitic stainless steel substrate.*** **Journal of Alloys and Compounds, 2010. 505(2): p. 824-831.**

**[34]. Parthasarathi, N.L., M. Duraiselvam, and U. Borah,** ***Effect of plasma spraying parameter on wear resistance of NiCrBSiCFe plasma coatings on austenitic stainless steel at elevated temperatures at various loads.*** **Materials & Design (1980-2015), 2012. 36: p. 141-151.**

**[35]. Hejwowski, T.,** ***Sliding wear resistance of Fe-, Ni- and Co-based alloys for plasma deposition.*** **Vacuum, 2006. 80(11): p. 1326-1330.**

**[36]. Zhang, Z., Z. Wang, and B. Liang,** ***Wear characterization of thermal spray welded Ni–Cr–B–Si–RE alloy coatings.*** **Journal of Materials Processing Technology, 2009. 209(3): p. 1368-1374.**

**[37]. Fernández, E., et al.,** ***Wear behaviour of laser clad NiCrBSi coating.*** **Wear, 2005. 259(7): p. 870-875.**

**[38]. González, R., et al.,** ***Wear behaviour of flame sprayed NiCrBSi coating remelted by flame or by laser.*** **Wear, 2007. 262(3): p. 301-307.**

**[39]. González, R., et al.,** ***Microstructural study of NiCrBSi coatings obtained by different processes.*** **Wear, 2007. 263(1): p. 619-624.**

**[40]. Serres, N., N. Portha, and F. Machi,** ***Influence of salt fog aging tests on mechanical resistance of laser clad-coatings.*** **Surface and Coatings Technology, 2011. 205(23): p. 5330-5337.**

**[41]. Wong, T.T., et al.,** ***Wear resistance of laser-clad Ni–Cr–B–Si alloy on aluminium alloy.*** **Journal of Materials Processing Technology, 2000. 100(1): p. 142-146.**

**[42]. Martín, A., et al.,** ***Sliding wear behaviour of plasma sprayed WC-NiCrBSi coatings at different temperatures.*** **Wear, 2001. 251(1): p. 1017-1022.**

**[43]. Rodríguez, J., et al.,** ***An experimental study of the wear performance of NiCrBSi thermal spray coatings.*** **Wear, 2003. 255(7): p. 950-955.**

**[44]. Sari, N.Y. and M. Yilmaz,** ***Improvement of wear resistance of wire drawing rolls with Cr–Ni–B–Si+WC thermal spraying powders.*** **Surface and Coatings Technology, 2008. 202(13): p. 3136-3141.**

**[45]. Kim, H.-J., et al.,** ***Assessment of wear performance of flame sprayed and fused Ni-based coatings.*** **Surface and Coatings Technology, 2003. 172(2): p. 262-269.**

**[46]. Van Acker, K., et al.,** ***Influence of tungsten carbide particle size and distribution on the wear resistance of laser clad WC/Ni coatings.*** **Wear, 2005. 258(1): p. 194-202.**

**[47]. Xu, J.S., et al.,** ***Microstructure and Sliding Wear Resistance of Laser Cladded WC/Ni Composite Coatings with Different Contents of WC Particle.*** **Journal of Materials Engineering and Performance, 2012. 21(9): p. 1904-1911.**

**[48]. Wang, X., et al.,** ***Microstructure and properties of laser clad TiC+NiCrBSi+rare earth composite coatings.*** **Surface and Coatings Technology, 2002. 161(2): p. 195-199.**

**[49]. Niranatlumpong, P. and H. Koiprasert,** ***The effect of Mo content in plasma-sprayed Mo-NiCrBSi coating on the tribological behavior.*** **Surface and Coatings Technology, 2010. 205(2): p. 483-489.**

**[50]. Buytoz, S., et al.,** ***Microstructural and Wear Characteristics of High Velocity Oxygen Fuel (HVOF) Sprayed NiCrBSi–SiC Composite Coating on SAE 1030 Steel.*** **Arabian Journal for Science and Engineering, 2013. 38(6): p. 1481-1491.**

**[51]. Fernandes, F., et al.,** ***Influence of nanostructured ZrO2 additions on the wear resistance of Ni-based alloy coatings deposited by APS process.*** **Wear, 2013. 303(1): p. 591-601.**

**[52]. Sun, R.L., Y.W. Lei, and W. Niu,** ***Laser clad TiC reinforced NiCrBSi composite coatings on Ti–6Al–4V alloy using a CW CO2 laser.*** **Surface and Coatings Technology, 2009. 203(10): p. 1395-1399.**

**[53]. Gómez-del Río, T., et al.,** ***Influence of the deposition techniques on the mechanical properties and microstructure of NiCrBSi coatings.*** **Journal of Materials Processing Technology, 2008. 204(1): p. 304-312.**

**[54]. Niranatlumpong, P. and H. Koiprasert,** ***Phase transformation of NiCrBSi–WC and NiBSi–WC arc sprayed coatings.*** **Surface and Coatings Technology, 2011. 206(2): p. 440-445.**

**[55]. Guilemany, J., et al.,** ***Tribología de recubrimientos Cermet/NiCrBSi depositados mediante HVOF.*** **Sistema, 2004. 2(W4): p. W6.**

**[56]. Bolelli, G., L. Lusvarghi, and R. Giovanardi,** ***A comparison between the corrosion resistances of some HVOF-sprayed metal alloy coatings.*** **Surface and Coatings Technology, 2008. 202(19): p. 4793-4809.**

**[57]. Man, H.C., et al.,** ***Laser surface alloying of NiCrSiB on Al6061 aluminium alloy.*** **Surface and Coatings Technology, 2001. 148(2): p. 136-142.**

**[58]. Flores, J.F., et al.,** ***Corrosion and Erosion-Corrosion Processes of Metal-Matrix Composites in Slurry Conditions.*** **Journal of Materials Engineering and Performance, 2012. 21(3): p. 395-405.**

**[59]. Gil, L. and M.H. Staia,** ***Influence of HVOF parameters on the corrosion resistance of NiWCrBSi coatings.*** **Thin Solid Films, 2002. 420-421: p. 446-454.**

**[60]. Serres, N., et al.,** ***Corrosion properties of in situ laser remelted NiCrBSi coatings comparison with hard chromium coatings.*** **Journal of Materials Processing Technology, 2011. 211(1): p. 133-140.**

**[61]. Shrestha, S., T. Hodgkiess, and A. Neville,** ***The effect of post-treatment of a high-velocity oxy-fuel Ni-Cr-Mo-Si-B coating Part I: Microstructure/corrosion behavior relationships.*** **Journal of Thermal Spray Technology, 2001. 10(3): p. 470-479.**

**[62]. Gil, L., M.A. Prato, and M.H. Staia,** ***Effect of post-heat treatment on the corrosion resistance of NiWCrBSi HVOF coatings in chloride solution.*** **Journal of Thermal Spray Technology, 2002. 11(1): p. 95-99.**

**[63]. Matsubara, Y., et al.,** ***Advanced Coatings on Furnace Wall Tubes.*** **Journal of Thermal Spray Technology, 2007. 16(2): p. 195-201.**

**[64]. Zhao, W.-M., et al.,** ***Corrosion mechanism of NiCrBSi coatings deposited by HVOF.*** **Surface and Coatings Technology, 2005. 190(2): p. 293-298.**

**[65]. Suutala, J., J. Tuominen, and P. Vuoristo,** ***Laser-assisted spraying and laser treatment of thermally sprayed coatings.*** **Surface and Coatings Technology, 2006. 201(5): p. 1981-1987.**

**[66]. Liu, S., X. Zheng, and G. Geng,** ***Dry sliding wear behavior and corrosion resistance of NiCrBSi coating deposited by activated combustion-high velocity air fuel spray process.*** **Materials & Design, 2010. 31(2): p. 913-917.**

**[67]. Zhao, W.-M., et al.,** ***Electrochemical evaluation of corrosion resistance of NiCrBSi coatings deposited by HVOF.*** **Surface and Coatings Technology, 2004. 183(1): p. 118-125.**

**[68]. Sharma, P. and J.D. Majumdar,** ***Microstructural Characterization and Properties Evaluation of Ni-Based Hardfaced Coating on AISI 304 Stainless Steel by High Velocity Oxyfuel Coating Technique.*** **Metallurgical and Materials Transactions A, 2013. 44(1): p. 372-380.**

**[69]. Tam, K.F., F.T. Cheng, and H.C. Man,** ***Enhancement of cavitation erosion and corrosion resistance of brass by laser surface alloying with Ni–Cr–Si–B.*** **Surface and Coatings Technology, 2002. 149(1): p. 36-44.**

**[70]. Serres, N., et al.,** ***Dry coatings and ecodesign part. 1 — Environmental performances and chemical properties.*** **Surface and Coatings Technology, 2009. 204(1): p. 187-196.**

**[71]. Kesavan, D. and M. Kamaraj,** ***Influence of aging treatment on microstructure, wear and corrosion behavior of a nickel base hardfaced coating.*** **Wear, 2011. 272(1): p. 7-17.**

**[72]. Stanford, M.K. and V.K. Jain,** ***Friction and wear characteristics of hard coatings.*** **Wear, 2001. 251(1): p. 990-996.**

**[73]. Sidhu, T.S., S. Prakash, and R.D. Agrawal,** ***Evaluation of hot corrosion resistance of HVOF coatings on a Ni-based superalloy in molten salt environment.*** **Materials Science and Engineering: A, 2006. 430(1): p. 64-78.**

**[74]. Sidhu, T.S., S. Prakash, and R.D. Agrawal,** ***A comparative study of hot corrosion resistance of HVOF sprayed NiCrBSi and Stellite-6 coated Ni-based superalloy at 900°C.*** **Materials Science and Engineering: A, 2007. 445-446: p. 210-218.**

**[75]. Sidhu, T.S., S. Prakash, and R.D. Agrawal,** ***Hot corrosion studies of HVOF NiCrBSi and Stellite-6 coatings on a Ni-based superalloy in an actual industrial environment of a coal fired boiler.*** **Surface and Coatings Technology, 2006. 201(3): p. 1602-1612.**

**[76]. Oliveira, F., et al.,** ***Corrosion–fatigue properties of a 4340 steel coated with Colmonoy 88 alloy, applied by HVOF thermal spray.*** **Surface and Coatings Technology, 2001. 140(2): p. 128-135.**

**[77]. Sidhu, T.S., S. Prakash, and R.D. Agrawal,** ***Hot corrosion behaviour of HVOF-sprayed NiCrBSi coatings on Ni- and Fe-based superalloys in Na2SO4–60% V2O5 environment at 900°C.*** **Acta Materialia, 2006. 54(3): p. 773-784.**

**[78]. Sidhu, T.S., S. Prakash, and R.D. Agrawal, *Hot corrosion resistance of high-velocity oxyfuel sprayed coatings on a nickel-base superalloy in molten salt environment.* Journal of Thermal Spray Technology, 2006. 15(3): p. 387-399.**

**[79]. Sidhu, T.S., S. Prakash, and R.D. Agrawal, *Study of Molten Salt Corrosion of High Velocity Oxy-Fuel Sprayed Cermet and Nickel-Based Coatings at 900 °C.* Metallurgical and Materials Transactions A, 2007. 38(1): p. 77-85.**

**[80]. Sidhu, T.S., S. Prakash, and R.D. Agrawal, *Characterisations of HVOF sprayed NiCrBSi coatings on Ni- and Fe-based superalloys and evaluation of cyclic oxidation behaviour of some Ni-based superalloys in molten salt environment.* Thin Solid Films, 2006. 515(1): p. 95-105.**

## Chapter IV

**[1]. Zhong, Z.W., Z.F. Peng, and N. Liu, *Surface roughness characterization of thermally sprayed and precision machined WC–Co and Alloy-625 coatings.* Materials Characterization, 2007. 58(10): p. 997-1005.**

**[2]. Swartzendruber, L.J., V.P. Itkin, and C.B. Alcock, *The Fe-Ni (iron-nickel) system.* Journal of Phase Equilibria, 1991. 12(3): p. 288-312.**

**[3]. Deshpande, S., S. Sampath, and H. Zhang, *Mechanisms of oxidation and its role in microstructural evolution of metallic thermal spray coatings—Case study for Ni–Al.* Surface and Coatings Technology, 2006. 200(18): p. 5395-5406.**

**[4]. Katranidis, V., et al., *FIB-SEM Sectioning Study of Decarburization Products in the Microstructure of HVOF-Sprayed WC-Co Coatings.* Journal of Thermal Spray Technology, 2018. 27(5): p. 898-908.**

**[5]. Verdon, C., A. Karimi, and J.L. Martin, *A study of high velocity oxy-fuel thermally sprayed tungsten carbide based coatings. Part 1: Microstructures.* Materials Science and Engineering: A, 1998. 246(1): p. 11-24.**

**[6]. Xiao, J.-K., et al., *Microstructure, wear and corrosion behaviors of plasma sprayed NiCrBSi-Zr coating.* Surface and Coatings Technology, 2019. 360: p. 172-180.**

**[7]. Kurlov, A.S. and A.I. Gusev, *Tungsten carbides and W-C phase diagram.* Inorganic Materials, 2006. 42(2): p. 121-127.**

**[8]. Zhan, Q., et al., *Quantitative evaluation of the decarburization and microstructure evolution of WC–Co during plasma spraying.* Surface and Coatings Technology, 2012. 206(19): p. 4068-4074.**

**[9]. Beste, U., et al., *Surface damage on cemented carbide rock-drill buttons.* Wear, 2001. 249(3): p. 324-329.**

**[10]. Stewart, D.A., P.H. Shipway, and D.G. McCartney, *Microstructural evolution in thermally sprayed WC–Co coatings: comparison between nanocomposite and conventional starting powders.* Acta Materialia, 2000. 48(7): p. 1593-1604.**

**[11]. Wang, D., et al., *Influence of carbide grain size and crystal characteristics on the microstructure and mechanical properties of HVOF-sprayed WC-CoCr coatings.* International Journal of Refractory Metals and Hard Materials, 2017. 69: p. 138-152.**

**[12]. Saha, G.C. and T.I. Khan, *Comparative Abrasive Wear Study of HVOF Coatings Obtained by Spraying WC-17Co Microcrystalline and Duplex Near-Nanocrystalline Cermet Powders.* Journal of Engineering Materials and Technology, 2011. 133(4).**

**[13]. Hemmati, I., et al., *Electron Microscopy Characterization of Ni-Cr-B-Si-C Laser Deposited Coatings.* Microscopy and Microanalysis, 2013. 19(1): p. 120-131.**

**[14]. Coddet, C., et al., *Surface preparation and thermal spray in a single step: The PROTAL process—example of application for an aluminum-base substrate.* Journal of thermal spray technology, 1999. 8(2): p. 235-242.**

**[15]. Mebdoua, Y., Y. Fizi, and H. Lahmar, *Determination of elastic-plastic parameters of inconel arc sprayed coating*, in *Applied Mechanics, Behavior of Materials, and Engineering Systems*. 2017, Springer. p. 193-203.**

**[16]. Bezborodov, V.P. and Y.N. Saraev. *Microstructure and mechanical properties of eutectic nickel alloy coatings*. in *IOP Conference Series: Materials Science and Engineering*. 2016. IOP Publishing.**

**[17]. Fale, S., A. Likhite, and J. Bhatt,** ***Nanoindentation, compressive and tensile deformation study of in-situ Al–AlN metal matrix composites.*** **Transactions of the Indian Institute of Metals, 2015. 68(2): p. 291-297.**

**[18]. Pramanik, A., L. Zhang, and J. Arsecularatne,** ***Deformation mechanisms of MMCs under indentation.*** **Composites Science and Technology, 2008. 68(6): p. 1304-1312.**

**[19]. Zeng, Q., et al.,** ***Corrosion Behavior of Thermally Sprayed NiCrBSi Coating on 16MnR Low-Alloy Steel in KOH Solution.*** **Journal of Materials Engineering and Performance, 2016. 25(5): p. 1773-1780.**

**[20]. Bergant, Z., U. Trdan, and J. Grum,** ***Effect of high-temperature furnace treatment on the microstructure and corrosion behavior of NiCrBSi flame-sprayed coatings.*** **Corrosion Science, 2014. 88: p. 372-386.**

**[21]. Cheniti, B., et al.,** ***Investigation of WC decarburization effect on the microstructure and wear behavior of WC-Ni hardfacing under dry and alkaline wet conditions.*** **Materials Chemistry and Physics, 2018. 208: p. 237-247.**

**[22]. Kim, H.-J., et al.,** ***Assessment of wear performance of flame sprayed and fused Ni-based coatings.*** **Surface and Coatings Technology, 2003. 172(2): p. 262-269.**

**[23]. Rachidi, R., B. El Kihel, and F. Delaunois,** ***Microstructure and mechanical characterization of NiCrBSi alloy and NiCrBSi-WC composite coatings produced by flame spraying.*** **Materials Science and Engineering: B, 2019. 241: p. 13-21.**

**[24]. Chen, L.-Y., et al.,** ***Improved hardness and wear resistance of plasma sprayed nanostructured NiCrBSi coating via short-time heat treatment.*** **Surface and Coatings Technology, 2018. 350: p. 436-444.**

**[25]. Zhang, Z.Q., et al.,** ***Characterization of microstructure and rolling contact fatigue performance of NiCrBSi/WC–Ni composite coatings prepared by plasma spraying.*** **Surface and Coatings Technology, 2015. 261: p. 60-68.**